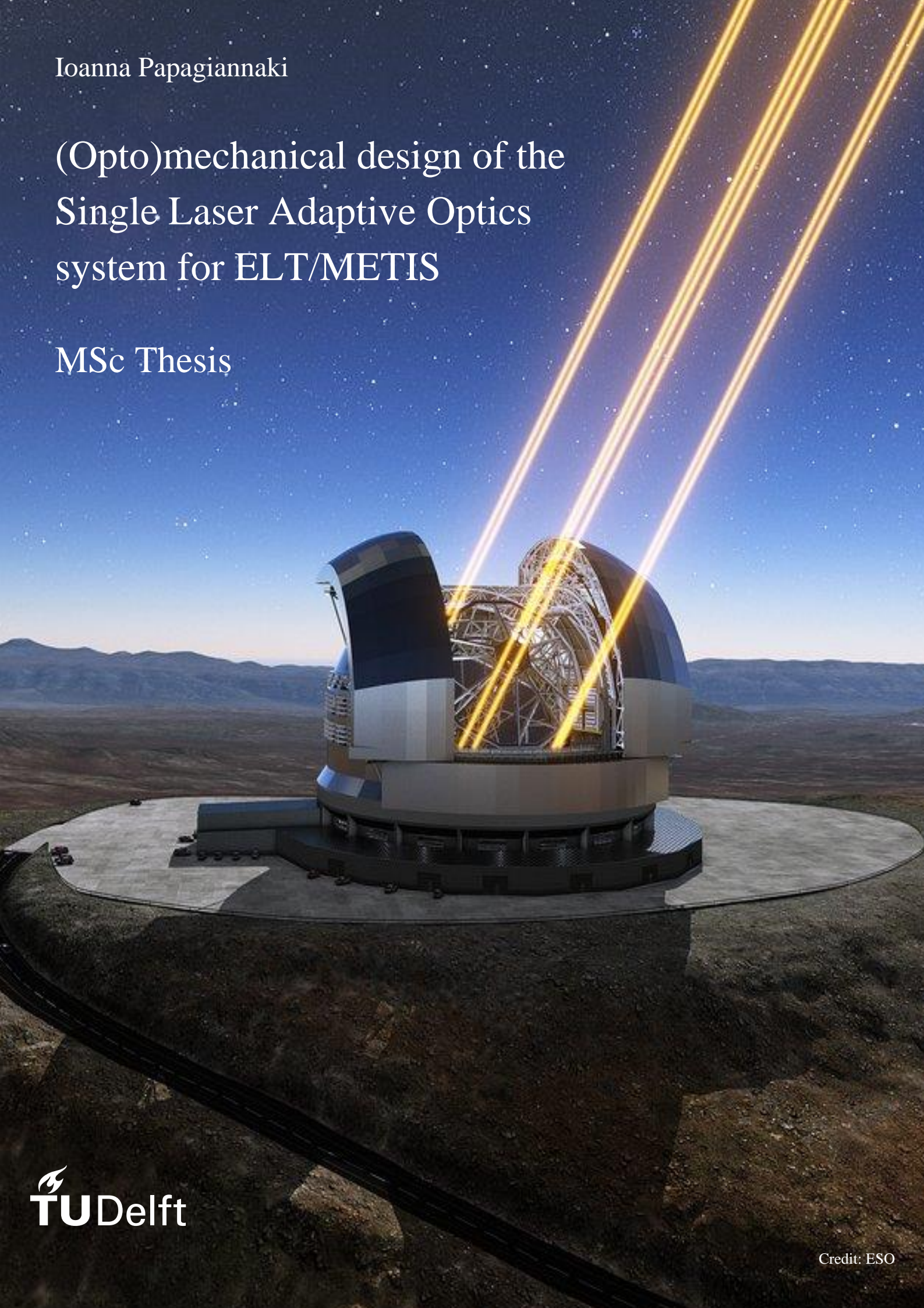


Ioanna Papagiannaki

(Opto)mechanical design of the Single Laser Adaptive Optics system for ELT/METIS

MSc Thesis



(Opto)mechanical design of the Single Laser Adaptive Optics system for ELT/METIS

By

Ioanna Papagiannaki

SN: 5016312

in partial fulfilment of the requirements for the degree of

Master of Science

in Aerospace Engineering

at the Delft University of Technology

Supervisors: Prof. Bernhard Brandl TU Delft / Leiden University
 Dr. Remko Stuik Leiden University

Thesis committee: Prof. Bernhard Brandl TU Delft / Leiden University
 Asst. Prof. Hans Kuiper TU Delft
 Dr. Remko Stuik Leiden University
 Prof. Bert Vermeersen TU Delft

Acknowledgements

The present dissertation is the result of the research I have conducted for my graduation project as part of my MSc studies in Aerospace Engineering at Delft University of Technology. This research has helped me gain more knowledge and a deeper understanding in an area I am particularly interested in, with the support and assistance of my supervisors; Professor Bernhard Brandl and Dr. Remko Stuik, to whom I would like to express my sincere gratitude and appreciation.

Furthermore, I would like to thank Assistant Professor Hans Kuiper, who jumped onboard later on and offered his expertise and apt comments during our discussions. I greatly appreciate the guidance he has provided.

Last but not least, I am grateful to my family for their wise counsel and sympathetic ear. They are always there for me to offer their invaluable support.

*I. Papagiannaki
Delft, May 2021*

Abstract

Terrestrial telescopes have been making significant contributions to Observational Astronomy for many centuries. Undoubtedly, the Earth's atmosphere limits the potential of ground-based observatories, not only by blocking the transmission of certain bands of the electromagnetic spectrum, but also by introducing errors in the wavefront, which are generated by the atmospheric turbulence and lead to the degradation of the image quality. Fortunately, the latter limitation can be mitigated with the aid of Adaptive Optics (AO). For that reason, AO systems have become an integral part of terrestrial observatories, as they allow for spatial resolutions comparable to those attained by space telescopes. Based on this fact, the scientific output of spaceborne observatories can be complemented by ground-based observations.

The Mid-infrared ELT Imager and Spectrograph (METIS), which is one of the three first-light instruments on the Extremely Large Telescope (ELT), will be equipped with a built-in Single Conjugate Adaptive Optics (SCAO) system in order to produce diffraction-limited images over a 27-arcsec Field of View. Although this Field of View is sufficient for reaching the instrument's primary science goals, an increase in its sky coverage would enable it to study additional objects of interest. To this end, an external, laser-assisted AO system is planned to be installed at a later stage. Laser-assisted systems use artificial beacons -also known as Laser Guide Stars (LGSs)- as reference for the image correction. Given the enormous size of ELT's primary mirror, a constellation of LGSs is necessary for good performance. Nonetheless, METIS's observing wavelength range could allow for the use of a simpler, laser-assisted AO system, namely, a Single Laser Adaptive Optics (SLAO) system, without significant performance loss.

In this thesis, the preliminary (opto)mechanical design of the SLAO system for METIS is presented. This design has been developed such that it ensures compliance with the predetermined mass, volume and budget limits, which are the driving design parameters. In a nutshell, the SLAO system comprises the support structure, the optics mounts and the subsystems providing the necessary motions. For the selection of the most suitable design concepts, different solutions are considered and evaluated through a tradeoff. Subsequently, the mechanical properties and attainable position accuracy of the resulting system are analyzed and estimates of its mass and cost are provided. Lastly, the outstanding points pertaining to the development of the (opto)mechanical design are discussed and, when possible, ways to resolve them are proposed.

Clearly, the design of METIS's SLAO system requires a considerable number of iterations before reaching maturity as well as the collaboration of engineers from different disciplines, given its complexity. The aim of the present thesis is to lay the groundwork for the (opto)mechanical design of the system by addressing the different aspects that need to be considered in the design process and propose possible solutions in order to meet the system's requirements.

Contents

1	Introduction.....	1
2	Project background	3
2.1	The Extremely Large Telescope	3
2.2	The Mid-infrared ELT Imager and Spectrograph.....	5
2.3	Adaptive Optics systems for ELT/METIS	7
2.3.1	The Single Conjugate Adaptive Optics system.....	8
2.3.2	The Single Laser Adaptive Optics system	10
3	Project objective and system specifications.....	17
3.1	Project objective	17
3.2	Engineering specifications.....	17
3.3	System requirements.....	20
4	Design concept selection	23
4.1	Conceptual design of the support structure	23
4.2	Mounting of optical components	29
4.2.1	Mounting techniques	30
4.2.2	Optical components in the SLAO system	32
4.2.3	Mirror mounting concept selection	34
4.2.4	Lens mounting concept selection	39
4.2.5	Multielement mounting concept selection	43
4.2.6	Axial preload and optomechanical contact interfaces.....	45
4.3	Implementation of motions in the SLAO system	50
4.3.1	Pickup mirror.....	50
4.3.2	Zoom optics.....	55
5	Preliminary (opto)mechanical design	57
5.1	Design of the support structure.....	57
5.2	Design of the (opto)mechanical components and subsystems	58
5.2.1	M1 subsystem.....	58
5.2.2	L1 mount	61
5.2.3	M2 mount	62
5.2.4	M3 mount	63
5.2.5	L2 mount	64
5.2.6	M4 mount	65
5.2.7	M5 mount	66
5.2.8	L3-L4 mount.....	67
5.2.9	L5-L6 mount.....	68
5.2.10	M6-M9 mount	69
5.2.11	M7-M8 subsystem.....	71
5.2.12	L7 mount	73
5.2.13	L8-L10 mount.....	74
5.3	Integration of components and subsystems into the SLAO system	75
5.4	Cleanliness.....	77
6	Results and Recommendations	79
6.1	Calculation of minimum axial preloads.....	79
6.2	Preload variations with temperature	87

6.3	Optomechanical tolerance analysis.....	90
6.4	Mass estimate.....	100
6.5	Cost estimate.....	101
6.6	Requirement verification	102
6.7	Future work.....	105
7	Conclusions.....	107
	Bibliography.....	109
	Appendix A: Geometry of the optical components.....	115
	Appendix B: Thermomechanical properties of the materials used in the SLAO system.....	117
	Appendix C: COTS components used in the SLAO system.....	119
	Appendix D: Preload and contact stress variations with temperature.....	123

List of Figures

<i>Figure 2.1. The dome (left) and main structure (right) of the ELT [15]. The instruments of the telescope will be mounted on the Nasmyth platforms. Eight LLTs will be located at the rim of M1.</i>	3
<i>Figure 2.2. Optical design of the ELT [16], [17].</i>	4
<i>Figure 2.3. Positions of ELT's first-light instruments on the Nasmyth platform [18].</i>	5
<i>Figure 2.4. Overview of the optical subunits in METIS [10].</i>	6
<i>Figure 2.5. METIS's cryostat, containing the Imagers, the Spectrograph,</i>	6
<i>Figure 2.6. Images of Uranus in the IR range without and with the use</i>	8
<i>Figure 2.7. SCAO scheme for METIS [24].</i>	9
<i>Figure 2.8. Layout of a SCAO system [25].</i>	9
<i>Figure 2.9. Residual error due to cone effect (left) and its reduction with an LTAO system</i>	11
<i>Figure 2.10. Perspective elongation of a Sodium LGS [27].</i>	12
<i>Figure 2.11. Difference between apparent and actual position of a LGS [7].</i>	13
<i>Figure 2.12. LGS and NGS positions for different zenith angles. The effects of</i>	13
<i>Figure 2.13. Current optical design of the SLAO system for METIS [14]. The letters M and L stand for mirror and lens, respectively. Only the front and back optical surfaces of the lenses are shown here.</i>	14
<i>Figure 3.1. Functions within the SLAO system.</i>	18
<i>Figure 3.2. Location of the external SLAO (former LTAO) system for METIS on the Nasmyth platform (left) and on METIS's platform (right) [12].</i>	19
<i>Figure 4.1. Retraction of the M1 through an eccentric rotation.</i>	24
<i>Figure 4.2. Retraction of the M1 through a horizontal translation.</i>	24
<i>Figure 4.3. Retraction of the M1 through a vertical translation.</i>	25
<i>Figure 4.4. New optical scheme of the SLAO system.</i>	26
<i>Figure 4.5. Concept A for the design of the support structure of the SLAO system.</i>	26
<i>Figure 4.6. Concept B for the design of the support structure of the SLAO system.</i>	27
<i>Figure 4.7. Concept C for the design of the support structure of the SLAO system.</i>	28
<i>Figure 4.8. Degrees of freedom of a body in space [28].</i>	29
<i>Figure 4.9. Mounting concepts for the support of large, non-metallic, vertical mirrors.</i>	35
<i>Figure 4.10. Application of the clamping forces [32].</i>	37
<i>Figure 4.11. Mounting concepts for the support of small mirrors [32].</i>	38
<i>Figure 4.12. Mounting concepts for the support of lenses [32].</i>	40
<i>Figure 4.13. Definition of the clear aperture, over which fabrication,</i>	43
<i>Figure 4.14. Multielement mounting in a common barrel [28].</i>	43
<i>Figure 4.15. Clamping angle and analysis of forces acting upon a clamped lens (the reaction force due</i>	45
<i>Figure 4.16. Optomechanical contact interfaces for different lens surfaces [32].</i>	47
<i>Figure 4.17. Optomechanical contact interfaces for different lens surfaces.</i>	48
<i>Figure 4.18. Examples of guide systems.</i>	51
<i>Figure 4.19. Power screw types.</i>	52

<i>Figure 4.20. Motorized lead screw configurations [50], [51].</i>	53
<i>Figure 4.21. Screw jack connected to a rotating</i>	54
<i>Figure 5.1. Preliminary design of the support structure.</i>	57
<i>Figure 5.2. Preliminary design of the M1 mount.</i>	59
<i>Figure 5.3. Preliminary design of the vertical translation system for M1.</i>	60
<i>Figure 5.4. M1 position when the SLAO is employed (left) and in its retracted state (right).</i>	60
<i>Figure 5.5. Preliminary design of the L1 mount.</i>	61
<i>Figure 5.6. Preliminary design of the M2 mount.</i>	62
<i>Figure 5.7. Preliminary design of the M3 mount.</i>	63
<i>Figure 5.8. Preliminary design of the L2 mount.</i>	64
<i>Figure 5.9. Preliminary design of the M4 mount.</i>	65
<i>Figure 5.10. Preliminary design of the M5 mount.</i>	66
<i>Figure 5.11. Preliminary design of the L3-L4 mount.</i>	67
<i>Figure 5.12. Preliminary design of the L5-L6 mount.</i>	68
<i>Figure 5.13. Preliminary design of the M6 mount.</i>	69
<i>Figure 5.14. Preliminary design of the M9 mount.</i>	70
<i>Figure 5.15. Preliminary design of the M6-M9 mount.</i>	70
<i>Figure 5.16. Preliminary design of the M7-M8 mount.</i>	71
<i>Figure 5.17. Exploded view of the M7-M8 mount.</i>	71
<i>Figure 5.18. M7-M8 mount attached to the selected translation stage.</i>	72
<i>Figure 5.19. Preliminary design of the L7 mount.</i>	73
<i>Figure 5.20. Preliminary design of the L8-L9-L10 mount.</i>	74
<i>Figure 5.21. Proposed integration sequence of the components and subsystems</i>	76
<i>Figure 5.22. Optomechanical design of the SLAO system. In the bottom right figure, the top view of the system is repeated with the M2 and M3 hidden for clarity.</i>	76
<i>Figure 5.23. Cleanliness of the SLAO system.</i>	77
<i>Figure 6.1. Mount-induced compressive contact stresses on the front optical surfaces</i>	84
<i>Figure 6.2. Mount-induced tensile contact stresses on the front optical surfaces</i>	85
<i>Figure 6.3. Mount-induced compressive contact stresses on the rear optical surfaces</i>	85
<i>Figure 6.4. Mount-induced tensile contact stresses on the rear optical surfaces</i>	86
<i>Figure 6.5. Block diagram representing a typical application of tolerances to an optomechanical system [32].</i>	90
<i>Figure 6.6. Mechanical coordinate systems.</i>	91
<i>Figure 6.7. Schematic diagram of a sphere in a V-groove [74].</i>	98
<i>Figure 6.8. Position of M7-M8 assembly at the two extremes and at an intermediate value of the zenith angle.</i>	105

List of Tables

<i>Table 2.1. Key design parameters of the SCAO system for METIS [26].</i>	10
<i>Table 2.2. Key design parameters of the selected WFS [13], [14].</i>	15
<i>Table 3.1. Boundary and ambient conditions of the SLAO system.</i>	19
<i>Table 3.2. General design requirements for the SLAO system.</i>	20
<i>Table 3.3. Requirements for the M1 subsystem.</i>	20
<i>Table 3.4. Requirements for the M7-M8 refocusing stage.</i>	21
<i>Table 4.1. Tradeoff for the selection of the conceptual design for the support structure of the SLAO system.</i>	29
<i>Table 4.2. General characteristics of bonding and mechanical clamping.</i>	30
<i>Table 4.3. Tradeoff for optics mounting techniques.</i>	31
<i>Table 4.4. List of all mirrors in the SLAO system.</i>	32
<i>Table 4.5. List of all lenses in the SLAO system.</i>	33
<i>Table 4.6. Tradeoff for the selection of the mounting concept for the large mirrors in the SLAO system.</i>	36
<i>Table 4.7. Tradeoff for the selection of the mounting concept for the lenses in the SLAO system.</i>	42
<i>Table 4.8. Tradeoff for the selection of the barrel design for the mounting of multiple.</i>	44
<i>Table 4.9. Commercially available vertical translation stages.</i>	50
<i>Table 4.10. Commercially available horizontal translation stages. All stages are equipped with a position sensor.</i>	55
<i>Table 4.11. Main characteristics of the translation stage LMS-270KSHO.</i>	55
<i>Table 6.1. Minimum axial preloads for the clamping of the mirrors.</i>	79
<i>Table 6.2. Minimum axial preloads for the clamping of the lenses.</i>	80
<i>Table 6.3. Parameters for the selection of the COTS metallic springs for the application of the preloads.</i>	80
<i>Table 6.4. O-ring compression for a cross section of approximately 2.6 mm (0.103 in) [71].</i>	82
<i>Table 6.5. Parameters for the selection of the O-rings for the application of the preloads.</i>	82
<i>Table 6.6. Applied preloads and calculated contact stresses for all mirrors.</i>	83
<i>Table 6.7. Applied preloads and calculated contact stresses for all lenses.</i>	83
<i>Table 6.8. Deflection and bending stress in custom-made springs.</i>	86
<i>Table 6.9. Axial preload change with temperature for mirrors M1, M2, M3 and M6.</i>	87
<i>Table 6.10. O-ring compression change with temperature.</i>	87
<i>Table 6.11. Radial preload change with temperature for mirrors M1, M2 and M3.</i>	87
<i>Table 6.12. Axial preload change with temperature for all lenses.</i>	88
<i>Table 6.13. Recovered thickness and reduction of percent compression due to compression set.</i>	89
<i>Table 6.14. M1 – Tolerance analysis.</i>	92
<i>Table 6.15. M2 – Tolerance analysis.</i>	92
<i>Table 6.16. M3 – Tolerance analysis.</i>	92
<i>Table 6.17. M4 – Tolerance analysis.</i>	93

<i>Table 6.18. M5 – Tolerance analysis.</i>	93
<i>Table 6.19. M6 – Tolerance analysis.</i>	93
<i>Table 6.20. M7 – Tolerance analysis.</i>	94
<i>Table 6.21. M8 – Tolerance analysis.</i>	94
<i>Table 6.22. M9 – Tolerance analysis.</i>	94
<i>Table 6.23. L1 – Tolerance analysis.</i>	95
<i>Table 6.24. L2 – Tolerance analysis.</i>	95
<i>Table 6.25. L3-L4 – Tolerance analysis.</i>	95
<i>Table 6.26. L5-L6 – Tolerance analysis.</i>	96
<i>Table 6.27. L7 – Tolerance analysis.</i>	96
<i>Table 6.28. L8-L9-L10 – Tolerance analysis.</i>	97
<i>Table 6.29. Virtual play in the horizontal and vertical direction for different load cases.</i>	99
<i>Table 6.30. Total mass of the SLAO system.</i>	100
<i>Table 6.31. Cost estimate for the SLAO system.</i>	101
<i>Table 6.32. Review of general design requirements for the SLAO system.</i>	102
<i>Table 6.33. Review of requirements for the M1 subsystem.</i>	103
<i>Table 6.34. Review of requirements for the M7-M8 refocusing stage.</i>	104
<i>Table A.1. List of all mirrors in the SLAO system. All mirrors are flat.</i>	115
<i>Table A.2. List of all lenses in the SLAO system. The above clear apertures correspond to a zenith angle</i>	116
<i>Table B.1. List of thermomechanical properties of all materials used for the optomechanical design of the SLAO system.</i>	117
<i>Table C.1. Parts list for all COTS components in the system.</i>	121
<i>Table D.1. Axial and radial preloads and contact stresses for all mirrors at -33 °C (survival range).</i>	123
<i>Table D.2. Axial and radial preloads and contact stresses for all mirrors at +85 °C (survival range).</i>	123
<i>Table D.3. Axial and radial preloads and contact stresses for all mirrors at 0 °C (operational range).</i>	124
<i>Table D.4. Axial and radial preloads and contact stresses for all mirrors at +15 °C (operational range).</i>	124
<i>Table D.5. Axial preloads and contact stresses for all lenses at -33 °C (survival range).</i>	125
<i>Table D.6. Axial preloads and contact stresses for all lenses at +85 °C (survival range).</i>	125
<i>Table D.7. Axial preloads and contact stresses for all lenses at 0 °C (operational range).</i>	126
<i>Table D.8. Axial preloads and contact stresses for all lenses at +15 °C (operational range).</i>	126

List of abbreviations and acronyms

ADC:	Atmospheric Dispersion Corrector	MAORY:	Multi-conjugate Adaptive Optics Relay
AIV:	Assembly, Integration and Verification	LTAO:	Laser Tomography Adaptive Optics
AO:	Adaptive Optics	MCAO:	Multi-Conjugate Adaptive Optics
CAD:	Computer Aided Design	METIS:	Mid-infrared ELT Imager and Spectrograph
CoG:	Center of Gravity	MICADO:	Multi-Adaptive Optics Imaging Camera for Deep Observations
COTS:	Commercial Off-The-Shelf	MIM:	Minimum Incremental Motion
CTE:	Coefficient of Thermal Expansion	MoS:	Margin of Safety
DM:	Deformable Mirror	n.a.:	not available
DoF:	Degrees of Freedom	N.A.:	Not Applicable
eAPD:	electron Avalanche Photodiode	NGS:	Natural Guide Star
ELT:	Extremely Large Telescope	QSL:	Quasi-Static Level
EM:	Electromagnetic	RfQ	Request for Quotation
ESO:	European Southern Observatory	RoC:	Radius of Curvature
FEA:	Finite Element Analysis	RSS	Root Sum Square
FKM:	Fluorocarbon elastomer	RTC	Real-Time Controller
FoV:	Field of View	SCAO:	Single Conjugate Adaptive Optics
HARMONI:	High Angular Resolution Monolithic Optical and Near-infrared Integral field spectrograph	SLAO:	Single Laser Adaptive Optics
HST:	Hubble Space Telescope	SMBH:	Supermassive Black Hole
IF:	Interface	SNR	Signal to Noise Ratio
IR:	Infrared	TBD:	To Be Defined
JWST:	James Webb Space Telescope	TT:	Tip-Tilt Mirror
LCU	Local Control Unit	VLT:	Very Large Telescope
LGS:	Laser Guide Star	WFS:	Wavefront Sensor
LLT:	Laser Launch Telescope		

Nomenclature

Latin

- a_G : Acceleration coefficient [-]
 C : Compression [%]
 CS : Compression Set [%]
 E : Young's modulus [GPa]
 F : Preload force [N]
 $f/\#$: Focal ratio [-]
 f_s : Safety factor [-]
 G : Shear modulus [GPa]
 g : Gravitational acceleration [m/s^2]
 LC : Load Capacity [N]
 m : Mass [kg]
 p : Preload per unit length of the contact [N/mm]
 R : Radius of curvature [mm]
 s_v : Virtual play [mm]
 T : Temperature [$^{\circ}C$]
 Y_c : Distance between the clamping location and the optical axis [mm]

Greek

- α : Clamping angle [$^{\circ}$]
 δ : Spring deflection [mm]
 μ : Coefficient of static friction [-]
 ν : Poisson's ratio [-]
 σ_B : Bending stress [MPa]
 σ_c : Compressive contact stress [MPa]
 σ_t : Tensile contact stress [MPa]
 σ_y : Yield strength [MPa]

1 Introduction

The technological developments of the 20th century have led to significant advances in Aerospace Engineering and Astronomy. The manufacturing of launch vehicles, which can carry crewed spacecraft or unmanned space probes, has revolutionized space exploration, while the building of more sophisticated instruments for astronomical observations has resulted in groundbreaking discoveries in Astronomy. More specifically, observations of Solar System bodies, such as planets, their moons, asteroids and comets have shed light on their characteristics and the underlying mechanisms that drive their evolution (Lissauer & de Pater^[1], McFadden et al.^[2]). Moreover, the study of circumstellar disks and the interstellar medium (ISM) has offered an insight into the formation of planets and stars, respectively (Lissauer & de Pater^[1]), while the detection and characterization of extrasolar planets has opened up new horizons in the quest for alien life (Impey^[3]). At the same time, research in the field of Extragalactic Astronomy has yielded important scientific breakthroughs related to the understanding of the formation, morphology and evolution of galaxies, as well as the composition of the intergalactic medium, and the mechanisms through which Active Galactic Nuclei (AGN) are powered by Supermassive Black Holes (SMBH) (Schneider^[4]).

Many of these observations have been performed with the aid of spaceborne observatories -such as the Hubble Space Telescope (HST) and the Spitzer Space Telescope-, which are capable of providing a higher spatial resolution and sensitivity for a certain aperture size, compared to their ground-based counterparts, since their performance is not influenced by the Earth's atmosphere and other sources of noise. Nonetheless, space missions are designed for limited lifetimes and are very expensive. Besides that, the payload mass and volume limitations have an impact on the achievable science goals, as they affect the versatility of the instruments onboard and restrict the aperture size of space telescopes, which defines the attainable angular resolution. To tackle this problem deployable telescopes can be employed, such as the James Webb Space Telescope (JWST), whose 6.5-m primary mirror renders it the largest and most powerful space telescope ever launched. However, the high cost and technological challenges engendered by the complexity of deployable telescopes do not allow for their rapid proliferation.

By contrast, mass and size constraints are not very stringent in the case of ground-based observatories, which can be built at a lower cost and can provide a multitude of observing modes by means of a multifunctional instrument suite. Also, terrestrial telescopes can have much larger apertures; thus, theoretically, they could offer a higher angular resolution were it not for the Earth's atmosphere. Fortunately, new techniques have been developed to mitigate the degradation of the image quality caused by the atmospheric turbulence. The first technique enables image restoration through the post-processing of short-exposure images (Labadie et al.^[5], McAlister^[6]). The second technique is based on Adaptive Optics (Tyson^[7], Hardy^[8], Roddier^[9]) and is mainly used when longer exposure times are necessary; for instance, when the objects of interest are rather dim, which is very often the case in astronomical observations.

The fact that the image quality resulting from the use of AO systems is comparable to that of images produced by space telescopes has led to their integration in many modern ground-based observatories, such as the Very Large Telescope (VLT) in Chile and the W.M. Keck observatory in Hawaii. Moreover, future large terrestrial telescopes, like the Extremely Large Telescope (ELT), are planned to be adaptive;

namely, they are designed with built-in AO components. Given the enhancement in the performance of terrestrial telescopes through AO, the benefits of a “collaboration” between spaceborne and terrestrial observatories cannot be disregarded; therefore, a synergy between JWST, ELT and other Earth-based facilities belongs to their long-term goals.

The operation of an AO system is based on one or more guide stars, which are sources of light that serve as reference for the sampling of the atmospheric turbulence in the vicinity of a science target (in terms of angular separation). This sampling enables the correction of the turbulence-induced wavefront aberrations in the incoming light in real time. The potential of AO systems can be further increased with the use of artificial guide stars, which are formed at relatively high altitudes with the aid of powerful laser beams. In that way, the scarceness of natural light sources can be partly overcome, as larger fractions of the sky are accessible for observations. For that reason, the ELT will be equipped with a facility comprising eight Laser Launch Telescopes, each of which will be able to form a Sodium-based artificial beacon in the sky.

The Mid-infrared ELT Imager and Spectrograph (METIS), which is one of the three first-light instruments on ELT, will focus on the study of circumstellar disks and planet formation, as well as on the detection and characterization of extrasolar planets (Brandl et al.^[10]). For the achievement of these science goals, the instrument will be equipped with an AO system which will use a natural guide star as reference for the mitigation of the effect of the atmospheric turbulence on the image quality. As discussed by Brandl et al.^[11], the contribution of METIS to the scientific output of the ELT could be increased if the scarceness of natural beacons could be overcome. For instance, observations of Solar System bodies could conduce to the research on the formation of the Solar System, while the instrument’s observing wavelength range, coupled with the high angular resolution the gigantic primary mirror will offer, could allow for observations of dim extragalactic objects. The benefits of this endeavor seem very compelling; therefore, the addition of a laser-assisted AO system to METIS is currently being investigated (Stuik et al.^[12], Arcier^[13], Tripsas^[14]).

Even though the use of more than one laser beacons by the supplementary AO unit of METIS would lead to a better performance, the high complexity and cost involved prohibit its realization. Optical studies have shown that the use of a single laser guide star will not severely compromise the performance of the AO system for the given observing wavelength range. Nonetheless, before selecting a single-laser AO system as baseline for the additional AO unit, a number of outstanding issues need to be resolved. In particular, the external single-laser AO unit will have to be designed and built within the given mass and volume limits and at an affordable price. The author will attempt to tackle this problem, as part of her MSc thesis, by developing a possible solution for the (opto)mechanical system of this supplementary AO unit.

The present thesis is organized as follows: Chapter 2 provides a brief description of ELT and METIS, and outlines the progress in the development of the Single Laser AO (SLAO) system for METIS. In Chapter 3 the objective of this thesis is specified and the system requirements are defined, while in Chapter 4 various design concepts are considered and the most favorable ones are selected. In Chapter 5 the preliminary (opto)mechanical design of the SLAO system is described and suggestions for its improvement are made. The various design choices are analyzed in Chapter 6 and the corresponding results are presented. In the same chapter the rough mass and cost estimates of the SLAO system are provided and a review of the set requirements is included. In addition, the future steps, related to the design of the SLAO system are delineated. Lastly, in Chapter 7 the conclusions drawn from this study are discussed and the potential impact of the employment of a SLAO system on the performance of METIS as well as other large telescopes in the future is considered.

2 Project background

In this chapter an overview of the ELT and a brief description of METIS are offered. In addition, the main characteristics of the AO systems in METIS are presented, their role in the instrument's performance is explained and their potential limitations are discussed. Lastly, the recent developments in the design of the laser-assisted AO system for METIS are summarized.

2.1 The Extremely Large Telescope

The Extremely Large Telescope, which will be located on Cerro Armazones in the Atacama Desert in Chile, will observe in the optical and infrared bands of the EM spectrum. It will be a reflecting telescope, boasting a segmented 39.3-m primary mirror (M1), which, with the aid of the installed AO systems, will provide (near) diffraction-limited angular resolution for a $f/17.75$ Nasmyth focal ratio and a 10-arcmin FoV. The dome and the main structure of the ELT are presented in *Figure 2.1*.

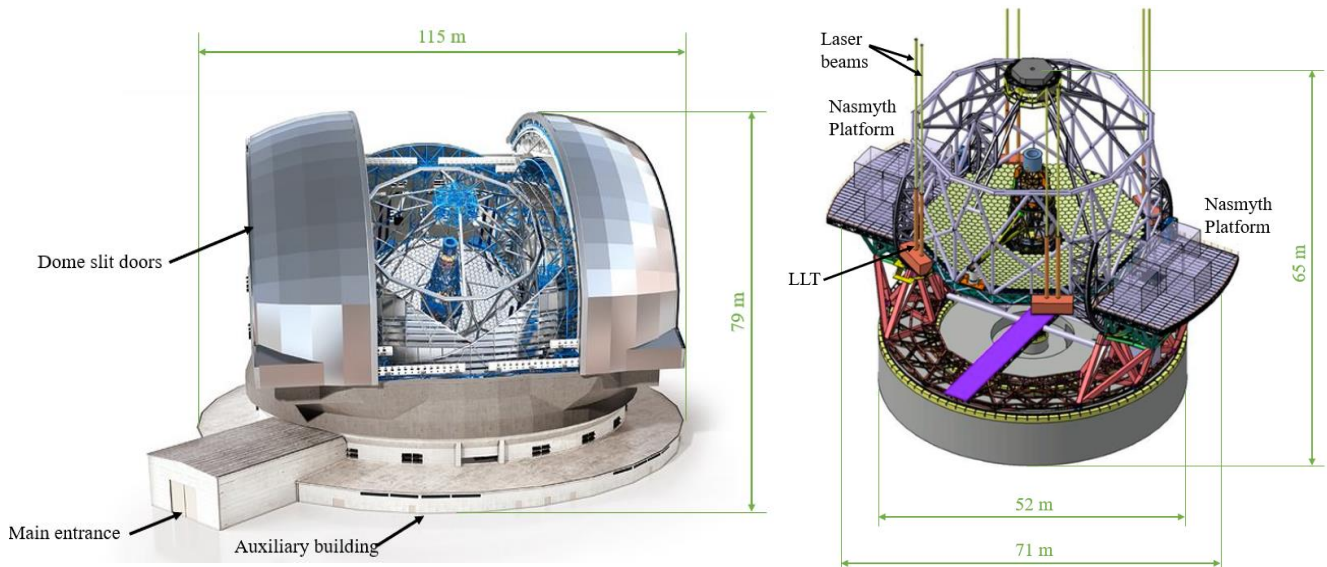


Figure 2.1. The dome (left) and main structure (right) of the ELT [15]. The instruments of the telescope will be mounted on the Nasmyth platforms. Eight LLTs will be located at the rim of M1.

The optical design of the telescope is based on a five-mirror scheme, which includes a Deformable Mirror (M4), equipped with 5316 contactless voice-coil actuators, and an elliptical fast-steering Tip-Tilt mirror (M5) for the correction of the high- and low-order, turbulence-induced wavefront aberrations, respectively. The slowly varying disturbances, caused by thermal gradients, wind loading and changes in the gravity vector (as the telescope alters its orientation), will be countered by actuators on the rear side of the 798 hexagonal segments comprising the M1, each of which is 1.4 m across. In *Figure 2.2* the optical design and the individual optical components are illustrated.

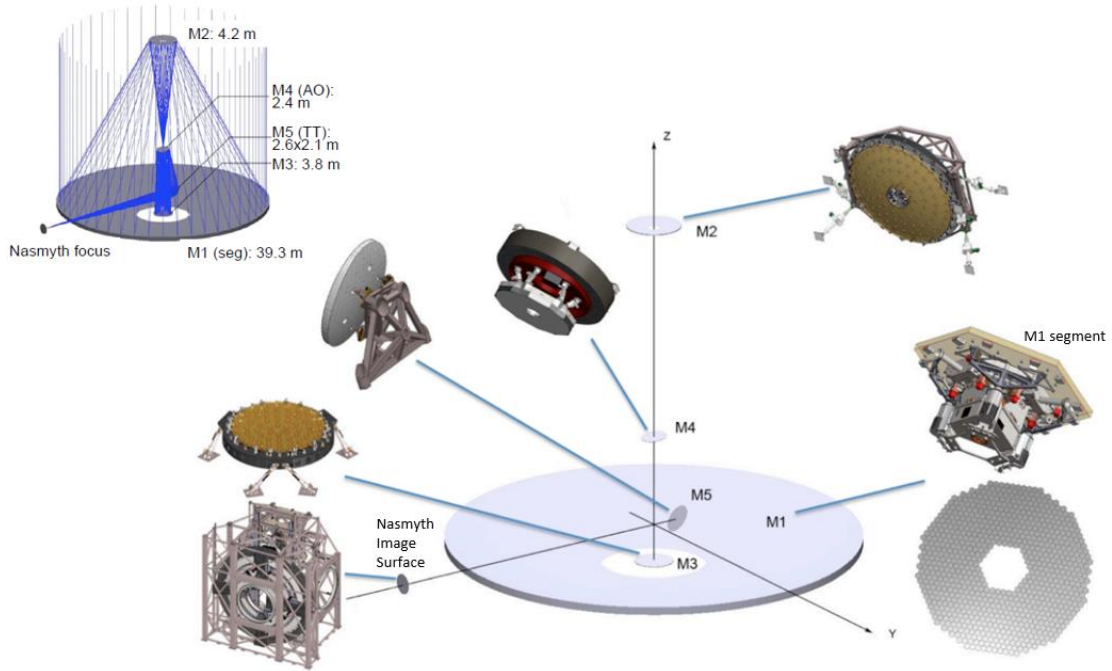


Figure 2.2. Optical design of the ELT [16], [17].

The incident light will be collected by the primary mirror M1 and will be reflected up to M2. Then, it will pass through the central hole of M4 and will reach the tertiary mirror (M3), where it will be reflected up to the quaternary Deformable Mirror (M4) and, subsequently, to the Tip-Tilt mirror (M5). The last reflection will direct the light into the instruments of the telescope, which are located on the Nasmyth platforms (*Figure 2.1*).

The types of AO systems used on ELT will not be the same for all instruments, but have been selected based on the observing wavelength range and the primary science goals of each one of them. The wide FoV offered by the primary mirror of the telescope will increase the probability of finding suitable NGSs for the operation of the AO systems. However, the sky coverage of the instruments will be further enhanced by eight Continuous-Wave (CW) laser beams, each of which will be able to form a Sodium LGS in the vicinity of the object(s) of interest (in terms of angular distance) and will be launched from dedicated LLTs, located at the rim of the M1 (*Figure 2.1*).

The reduction of the effect of the atmospheric turbulence on the image quality will enable ELT to observe the universe at an unprecedented angular resolution. The science goals of ELT include the observation of Solar System bodies, the detection and characterization of exoplanets, the study of protoplanetary disks, as well as the research on the life cycle of stars and the formation and evolution of galaxies. Furthermore, the activity of SMBHs at the centers of galaxies and the nature of dark matter and dark energy will be investigated. These goals will be achieved with the aid of a suite of instruments, the first-generation of which are MICADO (which will operate in combination with the MCAO module called MAORY), HARMONI and METIS. In *Figure 2.3* the positions of these instruments on ELT's Nasmyth platform are depicted. The present thesis focuses on METIS, however more information about the rest of the instruments can be found in the publications by Ramsay et al.^{[18],[19]}, ESO^[20] and Neichel et al.^[21].

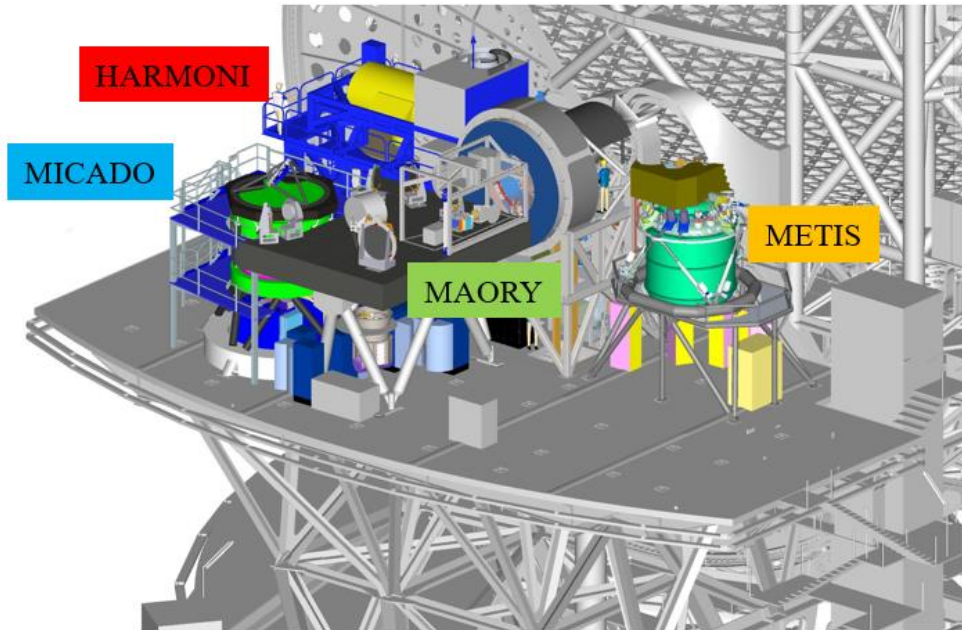


Figure 2.3. Positions of ELT's first-light instruments on the Nasmyth platform [18].

2.2 The Mid-infrared ELT Imager and Spectrograph

The primary scientific objectives of the Mid-infrared ELT Imager and Spectrograph (METIS) are the detection and characterization of extrasolar planets and the research on circumstellar disks and planet formation (Brandl et al.^[10]). The corresponding observations will be performed in a wavelength range spanning from 2.9 to 19 μm , which corresponds to the thermal infrared band of the EM spectrum, and is subdivided into the LM (2.9 – 5.3 μm) and NQ (7.0 – 19.0 μm) photometric bands. The instrument features three modules, each of which corresponds to a different observing mode: the LM- and NQ-Imager (IMG), and the LM-Spectrograph (LMS). These modules are depicted inside the blue box in the diagram presented in *Figure 2.4*. The LM- and NQ-Imager will perform imaging at the respective bands over a $10 \times 10 \text{ arcsec}^2$ FoV, including low-resolution, long-slit spectroscopy and coronagraphy for high contrast imaging. The LMS will be dedicated to high resolution integral field spectroscopy at the LM bands over a FoV of approximately $1.0 \times 0.5 \text{ arcsec}^2$ with an Integral Field Unit (IFU) (Brandl et al.^[10], Ramsay et al.^[19]).

Before entering the Imagers and Spectrograph, the light will pass through the Common Fore Optics (CFO) unit, where the elimination of the noise in the science beam will take place. Then, the light will propagate towards the CFO-AOP pickup mirror, which will forward the H and K bands into the built-in Single Conjugate Adaptive Optics system (SCA), where the measurement and correction of the turbulence-induced wavefront aberrations will be performed.

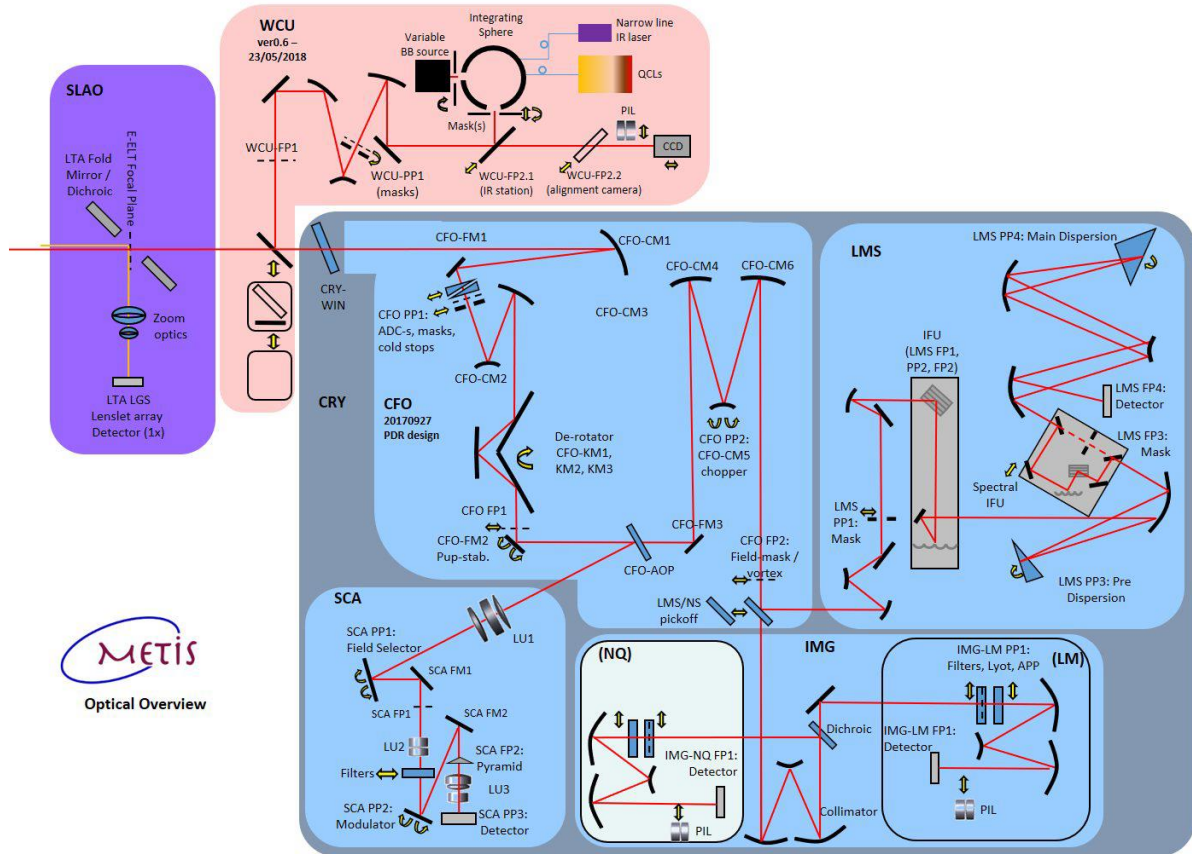


Figure 2.4. Overview of the optical subunits in METIS [10].

All the systems discussed so far will be kept inside a 4-m high and 3-m across cylindrical cryostat under vacuum (Figure 2.5), which will provide a stable thermal environment (40 K and 8 K for the LM and NQ bands, respectively), given that the instrument will observe in the thermal infrared spectral band. The controlled temperature inside the cryostat in conjunction with the beam chopper, which will detect and characterize any variations in the background radiation in the vicinity of the science target, will ensure the suppression of the noise in the signal, originating from the telescope, its environs and the sky.

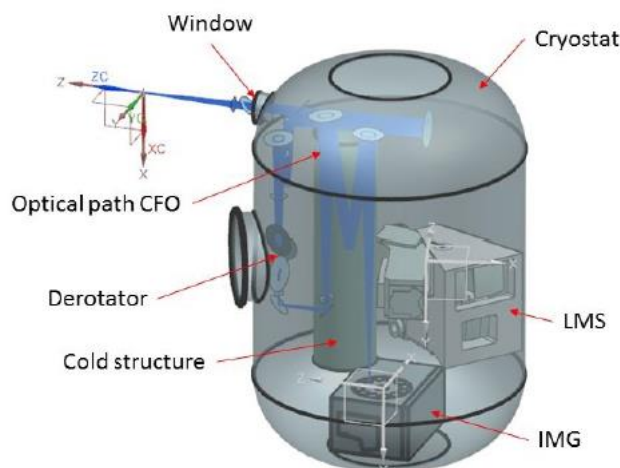


Figure 2.5. METIS's cryostat, containing the Imagers, the Spectrograph, the CFO and the SCAO system (not shown here) [22].

In addition, the Warm Calibration Unit (WCU), which is located above the cryostat and is depicted inside the pink box in *Figure 2.4*, will be used for the optical calibration and alignment verification of the instrument during the AIV process, as well as for routine daily calibrations. Lastly, the SLAO system, which is represented by the purple box in the same figure, will utilize a single LGS in order to increase the instrument's sky coverage, so that additional science goals can be achieved. For instance, the formation of the Solar System can be investigated through observations of Solar System bodies, while observations of high-redshift galaxies (which might be too faint to be observed with the aid of the SCAO system) will enable astronomers to research the formation and evolution of galaxies. A more detailed discussion of METIS's potential can be found in the publication by Brandl et al.^[11] The feasibility and performance study of the SLAO system has been conducted by Arcier^[13] as part of his MSc thesis. The present thesis is based on his work and constitutes a continuation of the project aiming at increasing METIS's sky coverage.

2.3 Adaptive Optics systems for ELT/METIS

The atmosphere can be thought of as a collection of air cells (also called scales) of various sizes and refractive indices, which are mixed together by the atmospheric turbulence. This mixing generates inhomogeneities in the optical properties of air, which give rise to time- and space-dependent fluctuations in the index of refraction within the atmospheric volume, leading to anisoplanatism. However, it can be assumed that within relatively small atmospheric volume fractions, the system is nearly isoplanatic, i.e. the atmosphere remains spatially coherent. In order to determine the size of the isoplanatic region and the time within which the system can be considered isoplanatic, the coherence length (also known as Fried parameter), r_o , and coherence time, τ_o , are defined. In much the same way, the isoplanatic angle, θ_o , is defined as the maximal angular separation between two observation points (e.g. the science target and the guide star), within which the assumption of spatial coherence still holds. All three parameters are wavelength-dependent and increase with wavelength.

The above-described parameters are key to the design of an AO system which can provide a (nearly) diffraction-limited performance. More precisely, the minimization of the residual errors in the correction of the wavefront aberrations is achieved if the angular distance between the science target and the guide star is smaller than the isoplanatic angle, θ_o , the spacing between the actuators on the Deformable Mirror(s) is smaller than the coherence length, r_o , and the frequency of the correction of the wavefront aberrations is higher than the inverse of the coherence time, τ_o .

An example of the performance of an AO system, employed for the imaging of planets, their moons and their atmospheres, is presented in *Figure 2.6*. This figure illustrates the images of Uranus at two different wavelengths in the IR range. At 1.6 μm the low-altitude clouds can be distinguished (brighter areas), while at 2.2 μm the planet's rings, three of its moons and the high-altitude clouds (bright spots near the right limb of the planet) are clearly visible. The darker color at 2.2 μm is attributed to the absorption of CH_4 gas existing in the planet's atmosphere. The same images, taken without the use of AO, are juxtaposed for comparison. It is obvious that the above-discussed details are not discernible if AO corrections are not applied.

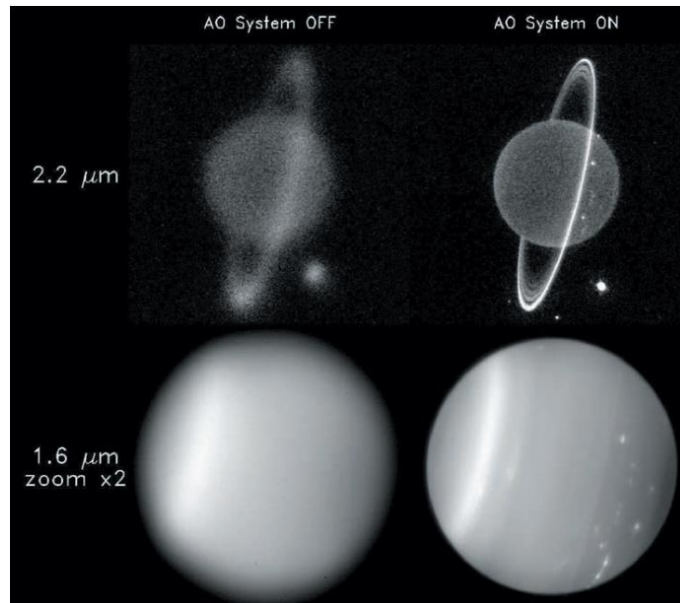


Figure 2.6. Images of Uranus in the IR range without and with the use of AO, produced at the W. M. Keck observatory [2].

As mentioned earlier, the image correction of METIS’s observations will rely on a built-in SCAO system, which will later be supplemented by an external, laser-assisted AO system. In the following discussion an overview of the design characteristics of the former and the status in the development of the latter are provided.

2.3.1 The Single Conjugate Adaptive Optics system

The SCAO system, which is located inside the cryostat together with the two Imagers, the Spectrograph and the Common Fore Optics unit, is equipped with a pyramid WFS (Hippler et al.^[23]) which, in conjunction with ELT’s M4 and M5, will measure and correct for the turbulence-induced wavefront aberrations. In *Figure 2.7* the location of the cryostat on the Nasmyth platform A and the optical path for the SCAO image correction are illustrated. On the righthand side of the figure the results of the simulated performance of the SCAO system are presented at two different wavelengths, using the exoplanet 51 Eridani b as test case.

The SCAO system will use an on-axis NGS as reference for the sampling of the atmospheric turbulence, which is assumed to be concentrated in a single layer at altitudes between 530 and 630 m above the aperture of the telescope (Hippler et al.^[23]). In general, the isoplanatic error due to angular anisoplanatism becomes significant as the angular distance between the guide star and the science target increases because of the loss in atmospheric coherence. Thus, an on-axis configuration ensures that angular anisoplanatism has no effect on the image quality.

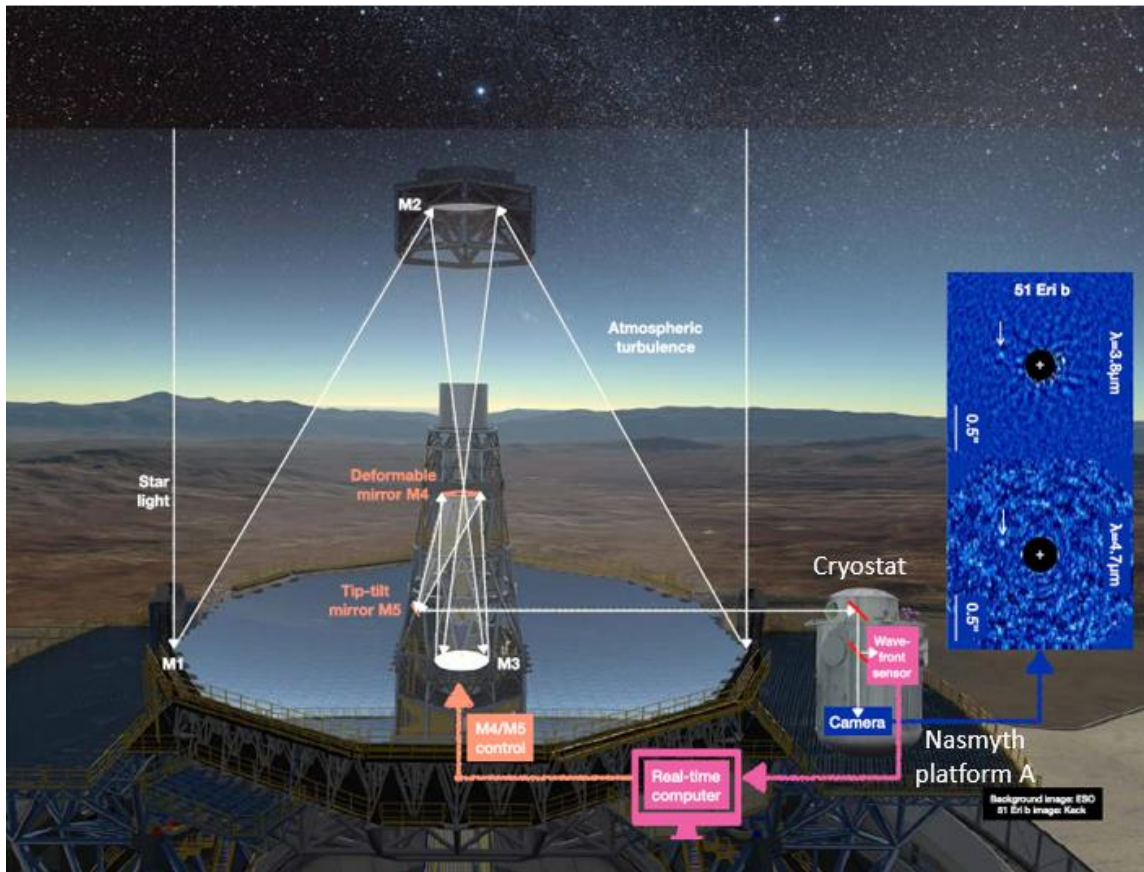


Figure 2.7. SCAO scheme for METIS [24].

Based on the working principle of a SCAO system, which is depicted in *Figure 2.8*, the WFS will be conjugate to ELT's DM (M4), which, in turn, will be conjugate to the turbulence layer above the telescope. This conjugation will offer a diffraction-limited instrument performance, since it will facilitate an optimal correction of the phase errors in the incoming light (Brandl et al.^[10], Stuik et al.^[12], Hippler et al.^[23]). The possibility of an on-axis operation of the SCAO system is ascribed to the fact that most of the instrument's science targets are either sufficiently bright or close to compact and bright objects. Consequently, the NGSs used by the SCAO system will be either the science targets themselves or light sources in their vicinity.

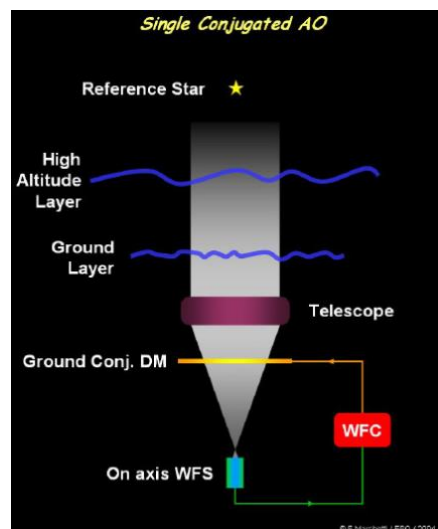


Figure 2.8. Layout of a SCAO system [25].

In the following table the most important design parameters of the SCAO system for METIS are summarized.

Wavelength range	1.45 μm – 2.45 μm
Field Selector FoV	\varnothing 27 arcsec
Selected FoV	\varnothing 2 arcsec
Optical wavefront decomposition	pyramid
Pupil sampling	0.5 m
Number of sub-apertures	77 x 77
Detector type	Leonardo Saphira eAPD
Detector geometry	256 x 320
Pixel per sub-aperture	1 per quadrant
Pixel size	24 μm
Frame rate	100 Hz – 1 kHz
Readout mode	Fowler-N
ADC for WFS	No
Field Selector	Yes
Modulator	Yes
Operating temperature	70 K
Command degrees of freedom	5316 +2
Command rate	\leq 1 kHz

Table 2.1. Key design parameters of the SCAO system for METIS [26].

Based on *Table 2.1*, any object within a FoV of 27 arcsec across can be observed every time. Moreover, as discussed by Hippler et al.^[23], the SCAO system shall guarantee a Strehl ratio of at least 93% at 10 μm , and at least 60% at 3.7 μm under median seeing conditions, at a zenith angle equal to 30° and for a NGS magnitude $m_K = 10$. In addition, the system shall provide image correction for zenith angles up to 60° with a degradation of the Strehl ratio not more than 40%, relative to zenith.

Although the available field size suffices for the achievement of the instrument’s main research objectives, it excludes observations of other objects of interest, such as extragalactic objects located outside the Galactic plane. The sky coverage of the instrument can be extended with the aid of an additional laser-assisted AO-system, which will also be capable of tracking objects inside the Solar System, such as planets, moons, asteroids and comets. In the following subsection, the progress in the design of the supplementary AO system for METIS is presented.

2.3.2 The Single Laser Adaptive Optics system

As discussed in Section 2.1, ELT is equipped with eight LLTs, each of which can launch one laser beam, tuned at a wavelength of 589 nm, so as to excite the Sodium atoms residing in the mesosphere (at approximately 90 km from sea level) to a higher energetic state. Every beam can, thus, form a LGS through the backscattering of the light produced by the Sodium atoms, as they return to their original energetic state. Given the finite altitude at which the LGSs are located, the cone effect (i.e. the inadequate

sampling of the atmospheric turbulence above the telescope) constitutes an important source of residual errors, as illustrated in the following figure. A Laser Tomography Adaptive Optics (LTAO) system, which employs a multitude of off-axis LGSs, can mitigate this problem.

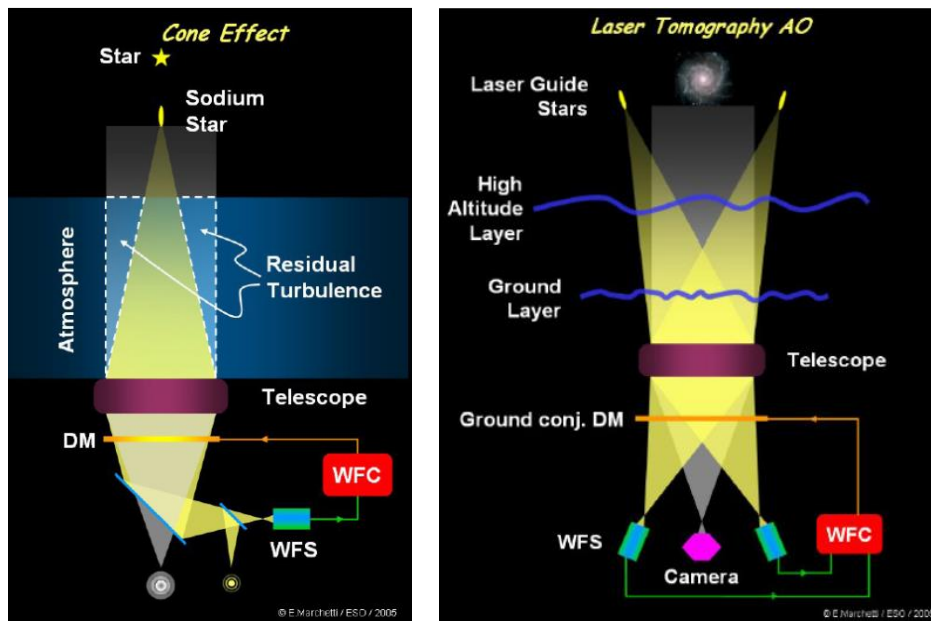


Figure 2.9. Residual error due to cone effect (left) and its reduction with an LTAO system (right) [25].

Generally, the degree to which the cone effect affects the performance of an AO system depends on the turbulence altitude, the aperture size and the observing wavelength. Assuming a constant altitude at which the turbulence layer is located and for a given observing wavelength, larger telescope apertures lead to higher residual errors, because the size of the unsampled volume fractions of the atmosphere above the full aperture increases. For that reason, the LTAO systems of the instruments on ELT will use no less than six LGSs to provide diffraction-limited imaging.

However, based on the earlier introduced notions of spatial and temporal atmospheric coherence, which are expressed with the parameters r_o (or θ_o) and τ_o , respectively, the atmospheric coherence is wavelength-dependent; namely, as the observing wavelength increases the atmosphere appears more coherent both spatially and temporally. Therefore, for given turbulence altitude and aperture size, the cone effect becomes less significant at longer wavelengths.

In the case of METIS, the baseline for the increase of its sky coverage was initially an external LTAO system, in order to minimize the influence of the cone effect on the image quality (Stuik et al.^[12]), given the large size of ELT's aperture. Even though this AO system type, generally, leads to a higher performance, it is more complicated and expensive. Therefore, a simpler and less expensive alternative is currently being investigated for METIS, involving the use of an on-axis Single Laser AO system, for which the name SLAO has been coined. This innovative approach is based on the fact that the instrument will perform long-wavelength observations, where the atmosphere is expected to be sufficiently coherent both in space and time, and thus, the cone effect will not significantly affect the quality of the observations.

Besides the cone effect, perspective elongation of the laser spot can have a negative impact on the performance of the SLAO system, given the large size of ELT's primary mirror. More specifically, even though it is considered that the maximum concentration of Na atoms can be found at an average altitude

of approximately 90 km above sea level, in reality these atoms are distributed within a layer of finite thickness (approximately 10 km), as illustrated in the following figure.

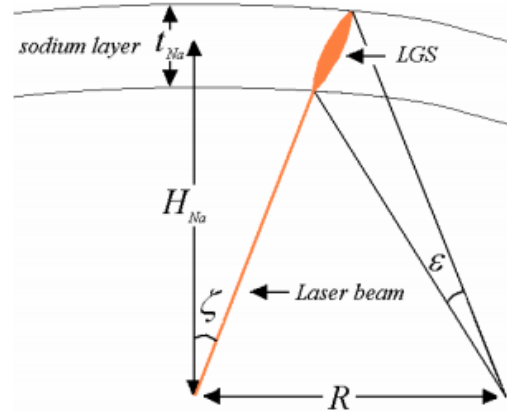


Figure 2.10. Perspective elongation of a Sodium LGS [27].

For a side launch of the laser beam, given the distance R between the LLT and the center of the telescope aperture (i.e. approximately the radius of the telescope aperture), the maximal spot elongation at zenith ($\zeta = 0^\circ$) can be approximated by the following expression:

$$\varepsilon \approx \frac{180 \times 3600}{\pi} \times \frac{R t_{Na}}{H_{Na}^2} \approx 0.255 R \text{ arcsec} \quad (2.1)$$

From the above equation, it can be observed that an increase in the size of the aperture leads to higher values of the spot elongation. Since the LGS is projected differently at different locations on the telescope pupil, the accuracy of the measurements of the wavefront aberrations and consequently the error correction become compromised.

Arcier^[13] studied the impact of both the cone effect and spot elongation on the performance of the SLAO system and concluded that the maximum attainable Strehl ratio at $3.8 \mu\text{m}$ and for typical atmospheric conditions can be up to 70% and the maximum sky coverage for a NGS magnitude $m_K = 16$ and a FoV of 10 arcsec is over 50%. These results prove that the performance of the SLAO system, although not ideal, could still help increase METIS's scientific output.

It should be noted that the SLAO system, when employed, will operate in tandem with the NGS-based SCAO system for the stabilization and focusing of the image in the telescope pupil. This "collaboration" is necessary for the elimination (or reduction) of both the high- and low-order wavefront aberrations, respectively. More precisely, a LGS-based AO system is insensitive to slowly-varying wavefront errors, i.e. global tip/tilt and absolute focus, because these low-order aberrations are compensated for during the round trip of the laser beam, as depicted in *Figure 2.11*. This effect is called tilt angular anisoplanatism (or angular anisokineticism) and manifests itself as loss of both image stability and sharpness in the telescope pupil. The measurement of the global tip and tilt is possible if a NGS is used in addition to the LGS(s), since the light emanating from the former follows a single route to reach the telescope aperture. The use of a NGS for the so-called "truth sensing" imposes limitations on the sky coverage of the instrument; however, the NGSs used to this end can be dimmer and at a greater angular distance from the science target.

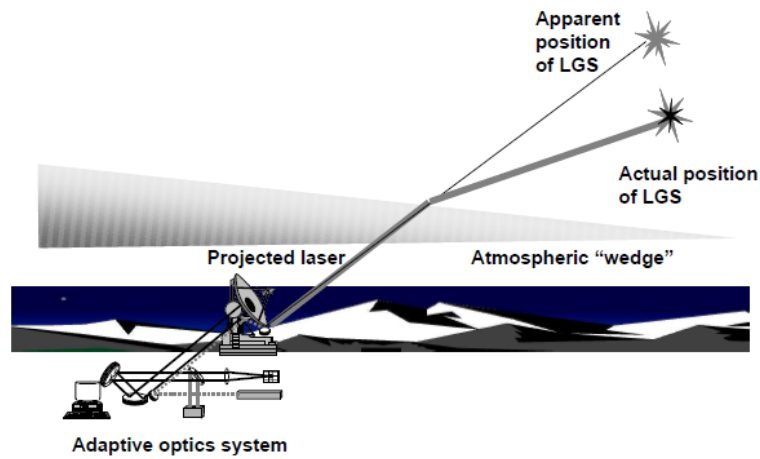


Figure 2.11. Difference between apparent and actual position of a LGS [7].

Another factor that can adversely affect the performance of a LGS-based AO system is the temporal and spatial variations of the Sodium concentration within the Sodium layer, which can lead to the detection of false wavefront aberrations. In addition, as the telescope alters its orientation to point at different targets in the sky, the zenith angle changes. As a result, the apparent distance between the LGS and the telescope varies, given that the LGS is formed at a finite altitude. This distance can be calculated as:

$$d = \frac{H}{\cos \zeta} \quad (2.2)$$

where H is the altitude at which the LGS is located and ζ is the zenith angle.

A change in the object distance results in a defocus of the laser beam on the WFS (if the WFS cannot move to compensate for the defocus). It is worth noting that based on the above equation, if a NGS is used, then changes in the zenith angle have no effect on the focus, since a NGS is located at infinity. In *Figure 2.12* the change in the apparent distance in the case of a Sodium LGS as a function of the zenith angle is illustrated and the position of a NGS is juxtaposed for comparison.

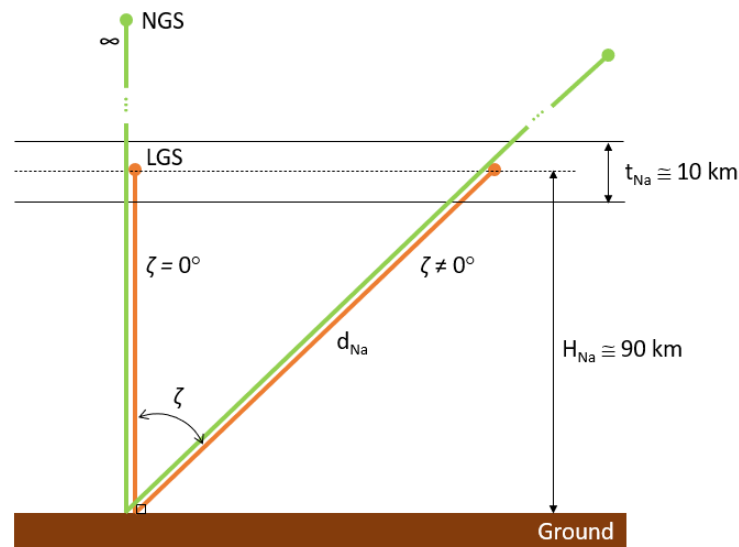


Figure 2.12. LGS and NGS positions for different zenith angles. The effects of the atmospheric refraction and curvature are not shown here.

The correction of the defocus caused by changes in the zenith angle and/or variations in the Sodium profile can be achieved with the aid of a refocusing stage, which allows the WFS to remain fixed at all times. This concept has been developed by Tripsas^[14], who improved the preliminary optical design of the SLAO system, which was initially created by Arcier^[13]. The current optical design of the SLAO system is presented in the following figure.

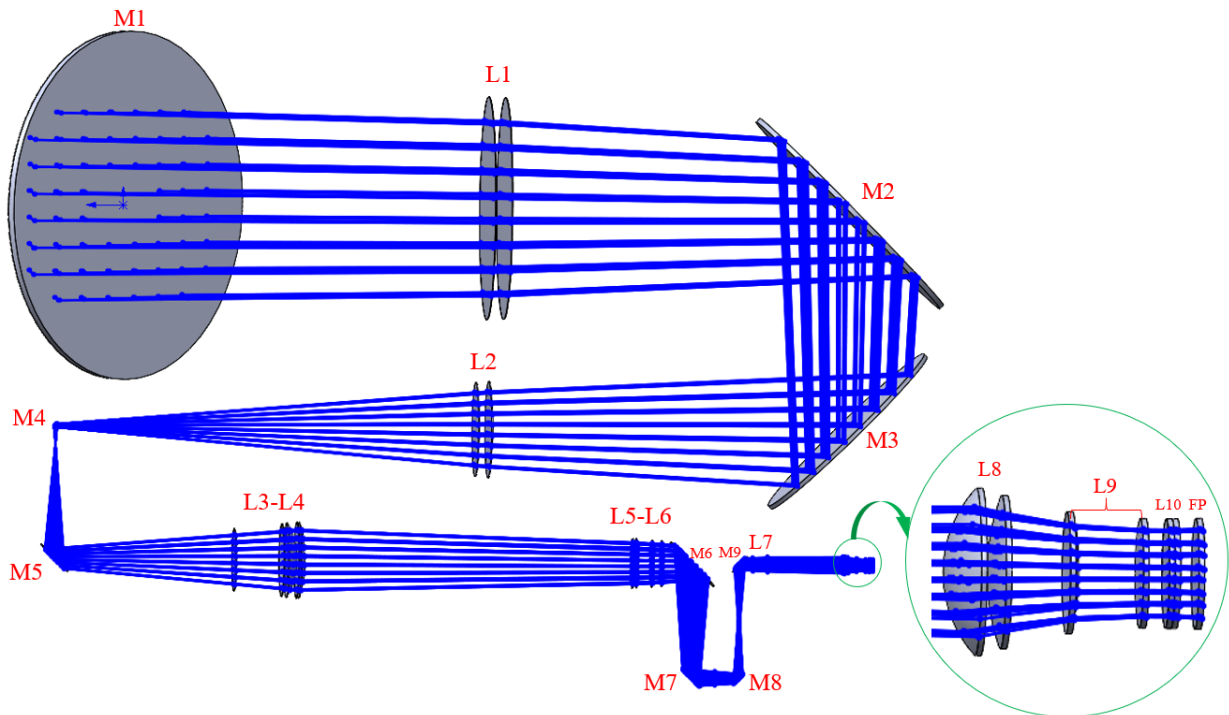


Figure 2.13. Current optical design of the SLAO system for METIS [14]. The letters M and L stand for mirror and lens, respectively. Only the front and back optical surfaces of the lenses are shown here.

This design proposes a solution for the separation of the science and NGS beam from the laser beam (represented by the red and orange lines, respectively, in *Figure 2.4*), which involves the use of an annular pickup mirror (M1), located at (or near) the focal plane of the ELT. This position has been selected on the grounds that there the size of the science field is minimal, since the science and NGS beams are in focus, whereas the LGS is completely out of focus (due to the fact that the science target and NGS are located at infinity, while the LGS is located at a finite altitude). At the position of M1 an image of the telescope pupil is formed, which does not contain any wavefront-related information at the center, because of the central obscuration of ELT's primary mirror. Consequently, the pickup mirror can transmit the science and NGS beam through a central opening and reflect the laser beam towards the WFS without major loss of information about the wavefront error and with a minimal size restriction of the scientific FoV.

Nonetheless, the projected size of the central obscuration is a function of the zenith angle; therefore, the size of the central opening in the annular pickup mirror has to be optimized. More specifically, a relatively large opening would increase the scientific FoV as well as the FoV of SCAO for the truth sensing, which, eventually, would lead to a higher sky coverage. On the other hand, a relatively small central opening would allow for a wider range of zenith angles. In practice, however, the performance of an AO system declines as the zenith angle increases, since the light beam has to travel a longer distance inside the atmosphere, along which the atmospheric coherence decreases. For that reason, 60° is currently considered the upper limit of the zenith angle range, for which the SLAO system will be operational, while the performance requirements can be met for zenith angles up to 45° .

It should be mentioned that the use of a dichroic has been considered as an alternative for the pickup of the LGS. However, the idea was jettisoned, since the component, being at room temperature, would introduce noise to the science and NGS signal, which, in turn, would deteriorate the performance of the instrument, especially at longer wavelengths.

Based on the current optical design of the SLAO system (*Figure 2.13*), after the first reflection of the laser beam from the pickup mirror (M1), the pupil is reimaged and directed towards the WFS through four reflections, realized with the aid of the fold mirrors M2, M3, M4 and M5. In addition, the mirrors M7 and M8 are movable in the vertical direction, so as to compensate for the defocus of the laser beam on the WFS as the zenith angle changes. Subsequently, lenses L7, L8 and L9 reimage the pupil on the lenslet array L10. The aspheric L9 renders the system image-space telecentric and the lenslet array generates sub-images of the pupil on the WFS, which is located at the focal plane (FP) of the system. The basic characteristics of the selected WFS are summarized in *Table 2.2*. In Chapter 4 the above-described optical design will be revisited and changes will be proposed, which will facilitate the (opto)mechanical design of the SLAO system.

WFS type	Shack – Hartmann
Lenslet array	40 x 40 sub-apertures
FoV per sub-aperture	10 arcsec
WFS Camera	LISA
Pixel array	800 x 800 pixels
Pixel size	24 μm
Pixels per sub-aperture	20 x 20 pixels
Pixel scale	0.5 arcsec/pixel

Table 2.2. Key design parameters of the selected WFS [13], [14].

3 Project objective and system specifications

Before delving into the (opto)mechanical design of the SLAO system it is necessary to define the various functions and constraints in the system, as well as the corresponding requirements it shall fulfill. In this chapter, the objective of the present project is defined and the specifications are discussed in detail. Moreover, the requirements are formulated, based on which different solutions for the (opto)mechanical design of the system will be studied.

3.1 Project objective

The objective of this project is to develop a validated (opto)mechanical design for the supplementary, SLAO system for METIS, which could help increase the sky coverage of the instrument. Clearly, the complexity of this system requires a careful analysis of the various aspects influencing its performance through a considerable number of iterations. Nonetheless, the limited timeframe within which the present thesis will have to be completed does not allow for such a detailed study. Thus, this thesis focuses on the development of the preliminary (opto)mechanical design of the SLAO system, based on the system specifications and requirements, which are discussed below. In addition, an optomechanical tolerance analysis will be performed and the total mass of the system as well as the resulting implementation cost will be estimated.

3.2 Engineering specifications

The optical performance of the system depends, to a large extent, on the way its individual components are held in position. More specifically, a mount shall ensure that the optical component will remain in position not only under the prevailing environmental conditions during integration, but also under potential environmental conditions that might compromise the achieved position accuracy and/or the health of the component (such as an earthquake or temperature variations). These environmental conditions, which must be known beforehand, have to be translated into load cases and studied carefully, so as to determine the behavior of the overall system in the worst case and define the corresponding Margins of Safety (MoS).

The pickup mirror (M1) plays a major role in the performance of the SLAO system, since its position accuracy determines the accuracy with which the laser beam is directed towards the rest of the system and whether the scientific FoV is vignetted or not. Therefore, it is important to eliminate any sources of alignment errors after integration. Moreover, a desirable property of the M1 is to be retractable, in order to avoid any restrictions in the scientific and SCAO FoV when the SLAO system is not employed, and to prevent a potential increase in the background radiation, due to the emission of thermal radiation by the component. Theoretically, this can be achieved either by a horizontal or vertical translation, or by a rotation, as indicated with the black dashed arrows in *Figure 3.1*. In Chapter 4 the most advantageous way to move this component will be investigated. Thus, repeatability is key to the development of a good design for the M1 subsystem, comprising the mirror mount and the translation system, so that the requirement related to the position accuracy of the M1's end position is met.

Besides that, as discussed in the previous chapter, the defocus of the laser beam on the WFS, which results from changes in the zenith angle of the telescope and/or fluctuations in the altitude of the Sodium layer, will be corrected with the aid of a zoom stage. On this stage the M7 and M8 will be mounted and, based on the current optical design, they will perform a vertical translation such that the focusing error is eliminated (*Figure 3.1*). In Chapter 4 the direction of this translation will be reconsidered in terms of implementation effort, and the possibility of using commercially available solutions that can cover the specific requirements of the subsystem (e.g. travel range, load capacity) will be examined.

Moreover, for some components position accuracy must be maintained in certain directions, while in other directions the mounting tolerances do not have to be very tight. For instance, in the case of M2 the tolerances for the in-plane translations and the rotation about the optical axis (roll angle) can be relatively loose; however, the out-of-plane translation and the tip and tilt angles have an influence on the optical path. By contrast, in the case of lenses large deviations from the optical axis are likely to lead to distortions and, thus, have to be avoided. This means that the lateral position accuracy needs to be relatively high.

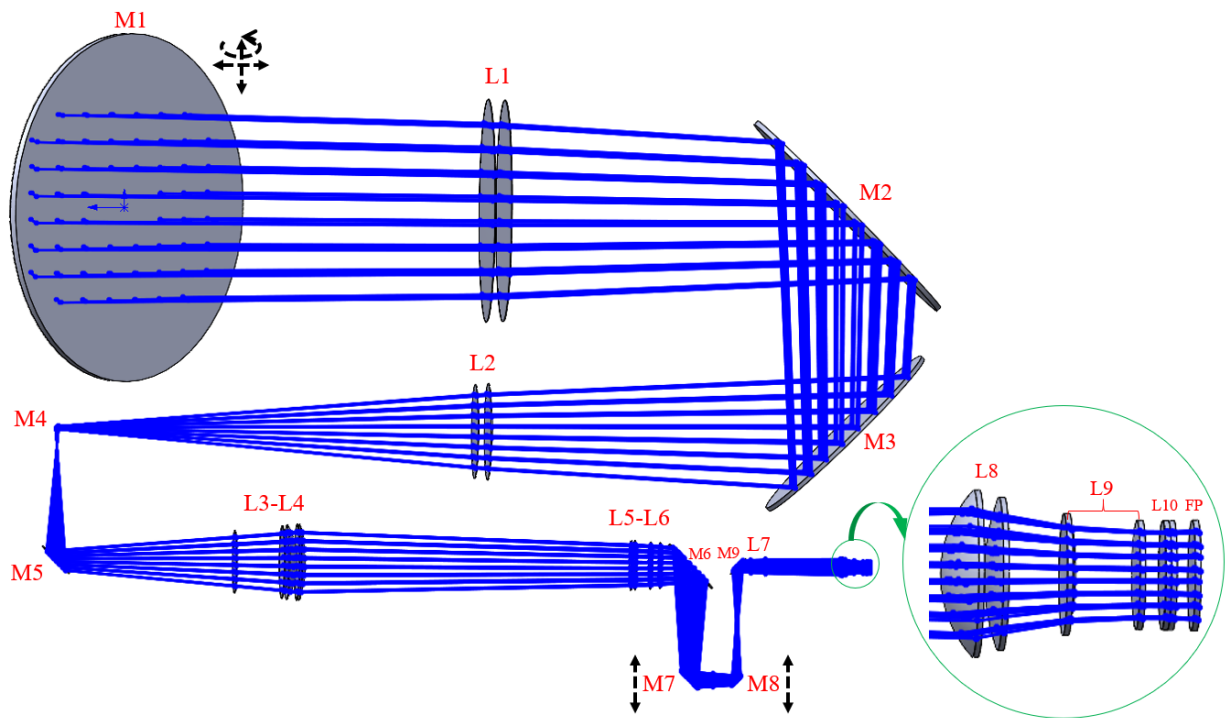


Figure 3.1. Functions within the SLAO system.

The SLAO system will be located between the Prefocal Station and METIS, and will be mounted on the platform of the instrument next to the cryostat, as illustrated in *Figure 3.2*. Therefore, there are limitations in the envelope and mass of the system. Furthermore, given that the support structure will provide the mounting interfaces (IFs) for all subsystems and components in the SLAO system, aside from mass and volume, thermomechanical stability and accessibility are of prime importance for its design. The boundary and ambient conditions, which will have to be taken into consideration for the (opto)mechanical design of the system, are summarized in *Table 3.1*.

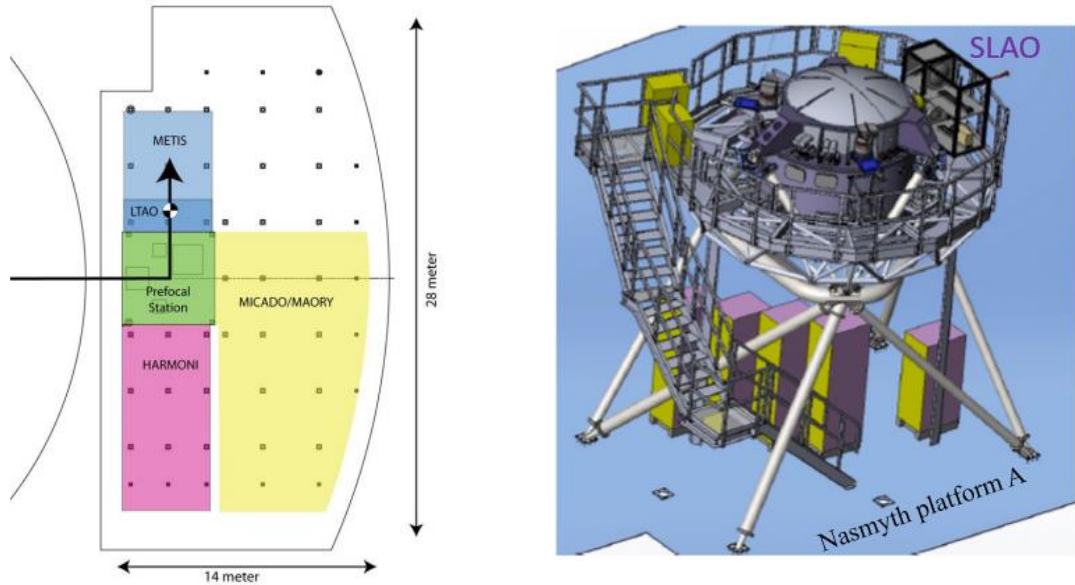


Figure 3.2. Location of the external SLAO (former LTAO) system for METIS on the Nasmyth platform (left) and on METIS's platform (right) [12].

Boundary conditions	
Allocated volume [mm ³] (length x height x width)	1500 x 1400 x 660
Allocated mass [kg]	1000
Operational Ambient Conditions	
Air temperature [°C]	0 to +15
Air gradient temperature [°C/h]	-0.55 to +0.5
Relative humidity [%]	5 to 80
Average wind speed [m/s]	< 2
Dust and sand levels	ISO 7.2 (median) and ISO 8 (90% percentile) according to EN ISO 14644-1: 1999
Aggressive atmosphere	NO ≤ 3ppb, NO ₂ ≤ 3ppb, SO ₂ ≤ 3ppb
Acceleration	N.A.
Survival Ambient Conditions	
Air temperature [°C]	-33 to +85 (during transportation and storage)
Air gradient temperature [°C/h]	-10.0 to +10.0 (over 30 min) -5.0 to +5.0 (over 1h)
Relative humidity [%]	3 to 100
Average wind speed [m/s]	< 16
Dust and sand levels	ISO 7.2 (median) and ISO 8 (90% percentile) according to EN ISO 14644-1: 1999
Aggressive atmosphere	NO ≤ 3ppb, NO ₂ ≤ 3ppb, SO ₂ ≤ 3ppb
Acceleration	3.5g (total QSL in any direction)

Table 3.1. Boundary and ambient conditions of the SLAO system.

3.3 System requirements

Based on the above-discussed functions and constraints, the requirements of the SLAO system and its subsystems are defined below.

Req. No.	Description
REQ-S-1	The SLAO system shall not violate the predetermined volume and mass limits, as defined in <i>Table 3.1</i> .
REQ-S-2	The design and implementation cost of the entire system shall not exceed 1 M€.
REQ-S-3	The design of the optics mounts shall ensure that the stresses in the optical components, resulting from the given load cases (<i>Table 3.1</i>), do not compromise their optical performance.
REQ-S-4	The design of the support structure shall provide the required stiffness for the given survival and operational loads, such that neither the structural health of the SLAO system nor the position accuracy of its subsystems and components are compromised.
REQ-S-5	The design of the support structure shall guarantee accessibility to the individual components of the system. <i>Rationale: Accessibility to the components and subsystems in the SLAO system can facilitate the integration, optical alignment and maintenance of the system.</i>
REQ-S-6	The design or selection of all subsystems and mechanical components in the SLAO system shall ensure that they can provide the necessary position accuracy at all times in the operational case and can withstand the corresponding loads in the survival case (<i>Table 3.1</i>).
REQ-S-7	The mechanical design of the SLAO system shall include measures that can increase the cleanliness levels of the unit.

Table 3.2. General design requirements for the SLAO system.

Req. No.	Description
REQ-M1-1	The dimensioning of the central opening of the M1 mirror shall guarantee that the vignetting in the scientific and SCAO FoV is lower than <TBD> arcsec.
REQ-M1-2	The translation/rotation system of the M1 mirror shall ensure that the component reaches its operational end position with an accuracy of <TBD> mm and/or <TBD> arcmin and with a repeatability of <TBD> mm.
REQ-M1-3	The translation/rotation system of the M1 mirror shall provide a travel range of no less than <TBD> mm or <TBD> degrees, in order to ensure that the component does not interfere with the science and NGS beam when the SLAO system is not employed.
REQ-M1-4	The translation/rotation system of the M1 mirror shall ensure that the component reaches its operational end position within <TBD> seconds.
REQ-M1-5	The position of the translation/rotation system of the M1 mirror shall ensure that it will not contribute to the instrument's background radiation. <i>Rationale: Any sources of thermal radiation (e.g. motor) located close to the science and NGS beam might introduce noise, which could have a negative impact on the instrument's performance.</i>
REQ-M1-6	The envelope of the translation/rotation system of the M1 mirror shall not violate the allocated volume for the SLAO system (<i>Table 3.1</i>).
REQ-M1-7	The design of the M1 subsystem, comprising the mirror mount and the corresponding translation/rotation system, shall ensure that the optical performance of the SLAO system is not degraded by any reflection artifacts.

Table 3.3. Requirements for the M1 subsystem.

Req. No.	Description
REQ-RFS-1	The M7-M8 refocusing stage shall provide a travel range of at least 125 mm.
REQ-RFS-2	The M7-M8 refocusing stage shall provide a MIM of at least <TBD> μm , in order to be able to accurately follow and correct for the defocus on the WFS for different object distances.
REQ-RFS-3	The M7-M8 refocusing stage shall guarantee that the two mirrors can reach their end position within <TBD> seconds.
REQ-RFS-4	The M7-M8 refocusing stage shall monitor and provide information about the current position of its carriage at any time.
REQ-RFS-5	The M7-M8 refocusing stage shall ensure that the pitch and yaw angles do not exceed <TBD> and <TBD> μrad , respectively.
REQ-RFS-6	The loaded M7-M8 refocusing stage shall be able to withstand the ambient conditions given in <i>Table 3.1</i> .
REQ-RFS-7	The envelope of the M7-M8 refocusing stage shall not violate the allocated volume for the SLAO system (<i>Table 3.1</i>).
REQ-RFS-8	The M7-M8 refocusing stage shall ensure that vignetting does not occur for zenith angles equal to or smaller than 45° .

Table 3.4. Requirements for the M7-M8 refocusing stage.

4 Design concept selection

This chapter focuses on the selection of the most suitable design concepts for the individual (opto)mechanical components and subsystems in the SLAO system. For this selection, different design options are considered and assessed, based on the specifications and requirements which have been defined in the previous chapter.

4.1 Conceptual design of the support structure

Prior to the selection of the most suitable design concept for the support structure of the SLAO system, i.e. the structure which will carry all subsystems and subassemblies, a review of the existing optical design is performed. The aim of this review is to investigate and evaluate any alternatives pertaining to the positions and directions of motion of the optical components, which could facilitate the mechanical design of the structure, reduce the integration effort, provide accessibility to the optical components and potentially reduce the implementation cost through the use of COTS components.

In Chapter 3 three different ways in which retractability of the pickup mirror M1 can be implemented have been briefly discussed. Given the size of the M1, the selection of the most suitable way to move the component away from the science and NGS beam has a direct impact on the design of the support structure. For that reason, the advantages and disadvantages of every option are discussed in this section and the selection of the most favorable concept is made.

Based on the first concept, which is presented in *Figure 4.1*, the M1 is retracted through an eccentric rotation about the axis passing through the edge of the component (indicated in red). The figure illustrates the front and top view of the entire system, the science and NGS beam (in green), as well as the allocated volume of the SLAO system (light blue contour). Although the rotation stage might not require a lot of space, it can be observed that the M1 in the retracted state violates the allocated volume. Furthermore, the mount of the M1 will require additional space, which will exacerbate the problem.

Nonetheless, even if the envelope could be increased, this solution is likely to lead to a poor mechanical performance due to the high mass of the optical component in conjunction with the given survival acceleration levels (*Table 3.1*). More precisely, the eccentric loading of the bearings in the mechanical system will result in uneven wear and thus degradation of the position accuracy overtime. Moreover, in the long term, the lifetime of the bearings will be shorter than the nominal. A rotation of the M1 about its axis of symmetry would be mechanically more favorable; however, it is out of question, since vignetting is very likely to occur. Lastly, the motor of the rotating stage will have to be located close to the science beam and might therefore contribute to the thermal noise.

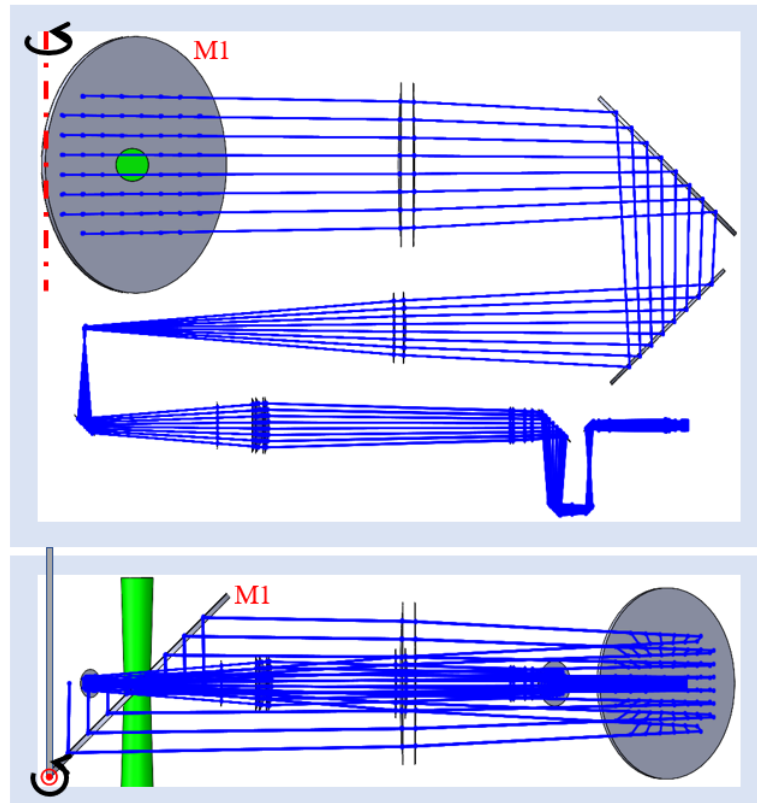


Figure 4.1. Retraction of the M1 through an eccentric rotation.

Another way to retract the M1 is through a horizontal translation towards L1. In that case the travel range is limited by the position of L1, as presented in *Figure 4.2*. Although this concept requires more space, the system stays within the allocated volume at all times. Nevertheless, if the thickness of M1 is taken into account, including a margin for its mount, chances are the science and NGS beam will be partly blocked. Besides that, similar to the previous concept, given the close proximity of the motor to the science beam, the thermal radiation it emits might degrade the overall performance of the system.

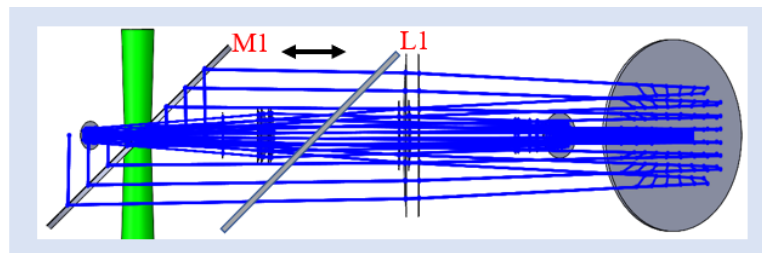


Figure 4.2. Retraction of the M1 through a horizontal translation.

Lastly, a vertical translation of the M1 could be implemented if the mirrors M4 and M5 were relocated, as illustrated in the following figure. A translation in the vertical direction would require more space, without, however, exceeding the allocated volume. In that way the travelling distance can be much longer, which would ensure that the M1 and the science beam are sufficiently far apart. Moreover, the motor can be positioned far away from the science beam without any additional modifications of the optical design.

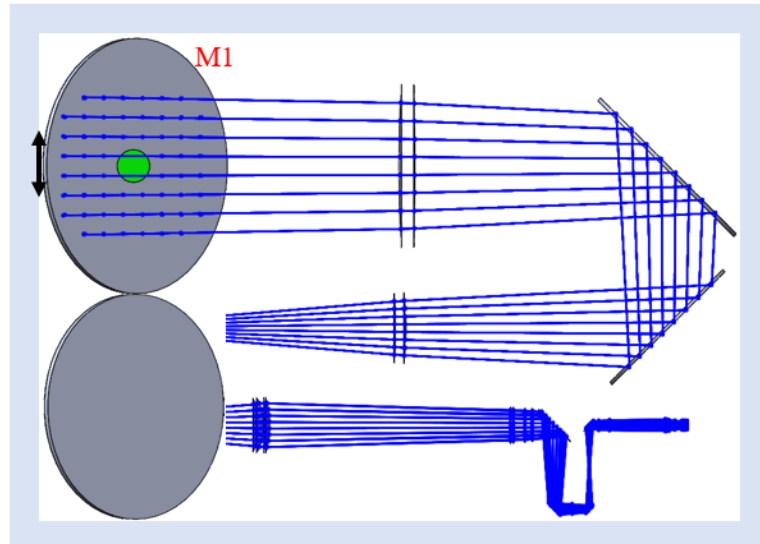


Figure 4.3. Retraction of the M1 through a vertical translation.

Based on the above discussion and given that a rearrangement of the M4 and M5 positions is possible, the most favorable way to retract the M1 is by means of a vertical translation. The implementation of this translation is discussed in detail in subsection 4.3.1. Aside from shifting the M4 and M5 to the right in order to clear the volume below the M1, the two mirrors could also be positioned on the same horizontal plane, so that they are mounted on the same plate, which would facilitate the integration and optical alignment of the components. This can be accomplished by pivoting the M5 by 90° , relative to the position of the M4. This rotation would, however, require a more efficient utilization of the space available in the horizontal plane, such that both optical components fit inside the allocated volume. To this end, a three-dimensional rotation of the M2 and M3 should be performed.

Another advantage of positioning the M4 and M5 on the same horizontal plane is that the translation of the mirrors M7 and M8 can be performed horizontally. More specifically, based on the current optical design (Figure 2.13), the mirrors M7 and M8 perform a vertical translation for the compensation of the defocus on the WFS for varying zenith angles. Ideally, a commercially available translation stage could be used for the implementation of this motion. The author investigated whether the required travel range can be covered by any vertical translation stage existing on the market and found out that this was not possible. If, however, the translation was horizontal, a plethora of options would be available. In order to make this possible, the components M7 and M8 will have to be rotated as a system about the optical axis passing through L3 and L4 by 90° . A more detailed discussion pertaining to the selection of the translation stage for the M7-M8 group is offered in subsection 4.3.2.

The resulting optical system representing the above-discussed rearrangements of the optical components is depicted below. In this figure the three-dimensional models of all optical components and the envelope of the LISA camera, carrying the WFS, are presented. On the left-hand side of the figure the front and top views are provided and on the right-hand side the top view is repeated with the components M2 and M3 hidden for clarity. Moreover, the black double-sided arrows represent the directions of the necessary motions in the system. In addition, the science and NGS, as well as the laser beams are included. It should be noted that by no means does this new optical scheme reflect an optical design.

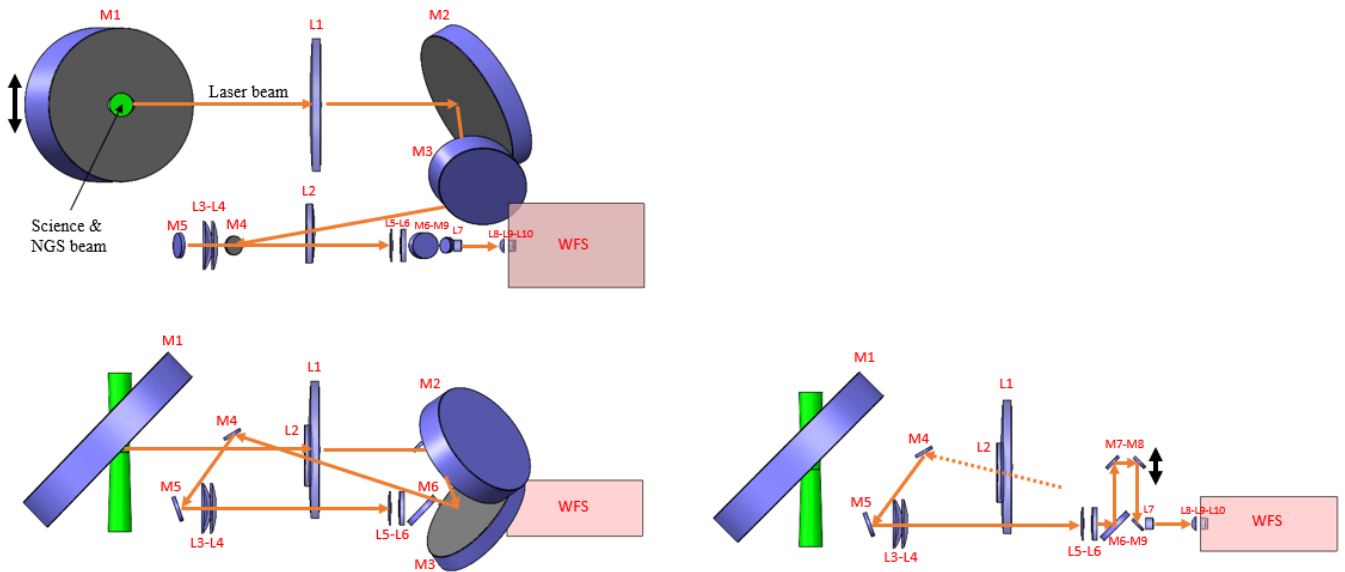


Figure 4.4. New optical scheme of the SLAO system.

With the above optical scheme as input, different concepts for the corresponding mechanical design of the support structure can be developed. *Figure 4.5* presents the first concept, based on which two horizontal blocks, which are connected with six vertical beams, are used for the mounting of the optical components of the system. This design offers accessibility to the individual components, whose integration is not expected to require excessive effort. Although the resulting mass is estimated to be relatively low, this concept is very likely to have a poor dynamic behavior. More precisely, if the structure is thought of as a vertical cantilever beam for the sake of simplicity, then the force and deflection at the free end, i.e. at the upper block, will be relatively high, given that at this location a high mass is connected. The inferior structural behavior is bound to lead to an unsatisfactory optical performance as well.

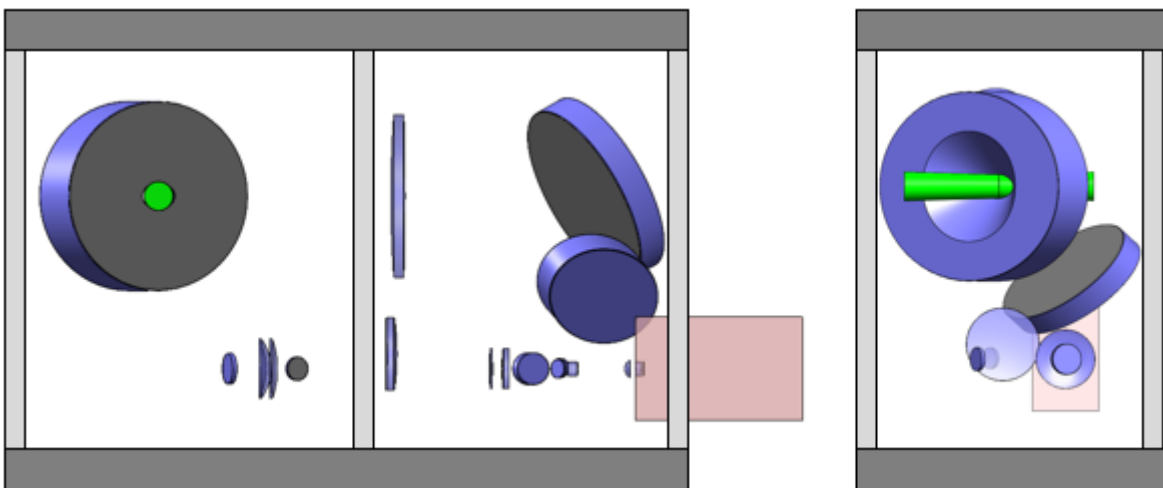


Figure 4.5. Concept A for the design of the support structure of the SLAO system. The front and side views are presented.

In *Figure 4.6* a second concept is illustrated. Two large blocks are located in front and behind the optical components of the SLAO system and are connected with six beams. An additional base plate is added to the system to minimize torsion. The two blocks will carry the majority of the components and, if necessary, the base plate can be also used for that reason. Although the stability of the system is expected to be better than that provided by the previous concept, the overall mass will be much higher. Furthermore, the accessibility of the components will be poor and the integration quite cumbersome.

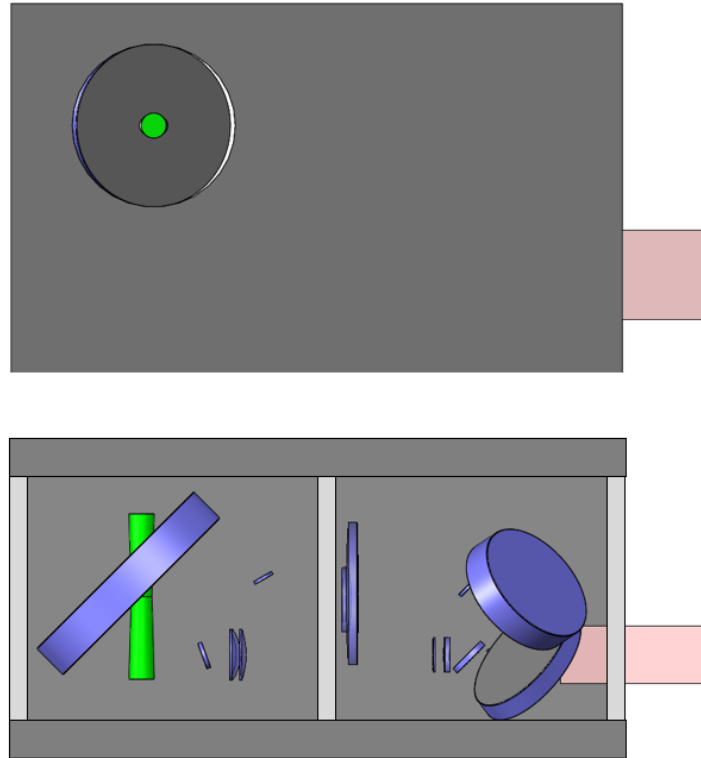


Figure 4.6. Concept B for the design of the support structure of the SLAO system. The front and top views are presented.

Lastly, a third concept is depicted in *Figure 4.7*. In this case, the support structure comprises three vertical blocks, which are connected with eight horizontal beams, and a base plate. The optical components are mounted on the three vertical blocks either directly or indirectly, i.e. on transverse mounting plates supported by the blocks. The main disadvantage of this concept is that torsion might lead to misalignments in the upper part of the system. The mass of the system is estimated to be higher than that of concept A but lower than that of concept B. However, the optical components are well accessible and their integration into the system is not expected to be particularly difficult. An additional advantage of this concept is that it separates the system in different volume sections, which facilitates the inclusion of mechanical parts (e.g. sheet metals) that can protect most of the components from contamination. It should be noted that in the above-discussed concepts, the dimensions of the mechanical components, illustrated in the corresponding figures, do not represent their actual dimensions.

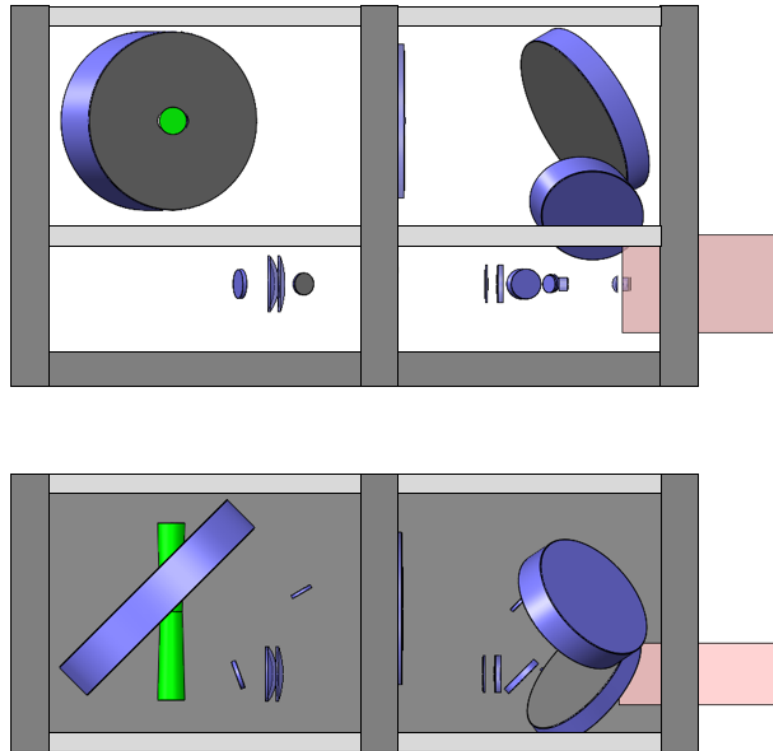


Figure 4.7. Concept C for the design of the support structure of the SLAO system.
The front and top views are presented.

For the selection of the most advantageous conceptual design of the support structure, a tradeoff can be made. This evaluation is realized with a Pugh matrix, for which a rating is defined, expressing the performance of every concept for a specific criterion. This rating can take three distinct values: -1 if the performance of the concept in question has a negative impact on the overall system, 0 if the concept is adequate, or 1 if the concept leads to excellent results. Every rating is weighted by a weighting factor on a scale from 1 to 5, assigned to every criterion. The value of every weighting factor reflects the impact of the corresponding criterion on the overall system. The sum of the weighted performance for every criterion expresses the total score of every concept.

In the following tradeoff stability, mass and cost receive the highest weighting factor. Stability is directly linked to optical performance; thus, in the case of the support structure instability is likely to lead to a chain of misalignments of the individual components, resulting in a degradation of the overall performance of the system. In addition, mass and cost are the main design limitations for the realization of the SLAO system, therefore they are of prime importance. The integration effort and the accessibility of the individual components receive a weighting factor equal to 4, given that difficulties in integration and accessibility often require additional tooling, which increases the implementation cost of the system. Lastly, the weighting factor for cleanliness is equal to 2. Measures which ensure that the system remains clean over long periods of time are desirable, but do not play a decisive role in the design of the support structure.

Criteria	Weighting factor	Concept A	Concept B	Concept C
Stability	5	-1	1	0
Mass	5	1	-1	0
Cost	5	1	-1	0
Integration effort	4	0	-1	1
Accessibility	4	0	-1	1
Cleanliness measures	2	0	0	1
Results		5	-13	10

Table 4.1. Tradeoff for the selection of the conceptual design for the support structure of the SLAO system.

Based on the above tradeoff, concept C has received the highest score and is, therefore, deemed to be the most favorable design option for the support structure of the SLAO system. It should be noted, however, that since the performed tradeoff is qualitative, a more detailed study of some of the criteria is necessary, such as the stability of the system.

4.2 Mounting of optical components

In three dimensions, a rigid body has six Degrees of Freedom (DoFs): three translations and three rotations, as indicated by the letters T and R, respectively, in the following figure. These DoFs can be controlled through constraints which are characterized by high stiffness in the direction of motion that needs to be restricted; the rigidity of such constraints guarantees that through the resulting reaction force the body will maintain its position. In order to ensure no loss of contact between the body and the constraints, a preload force is often applied. It is worth noting that this constant force is not considered a constraint.

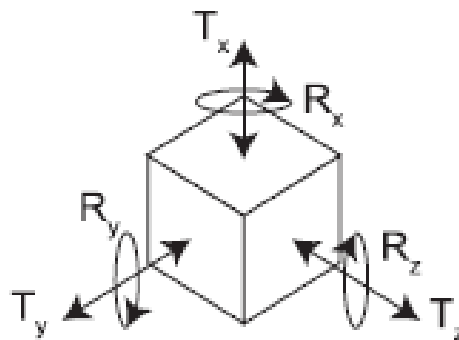


Figure 4.8. Degrees of freedom of a body in space [28].

Generally, an object is exactly constrained if it is both kinematically determinate (i.e. it has no unintended DoFs) and statically determinate (i.e. it has no redundant constraints). In this case, neither will the object perform any unwanted motions, nor will the precision of its position be compromised by small manufacturing errors or self-stress; namely, the build-up of internal stresses. Thus, an exactly constrained system can offer high stability and precision without requiring tight manufacturing tolerances. For that

reason, this principle is used very often for the mounting of optical components, for which position accuracy, low internal stresses and repeatability in assembling are key to high performance.

4.2.1 Mounting techniques

The constraining of an optical component can be achieved either through bonding, i.e. with the use of an adhesive, or by means of mechanical clamping. The selection of the most appropriate technique depends on the specific application. Therefore, the advantages and disadvantages of both techniques need to be taken into consideration in order to develop a design that not only performs to specification, but also does not require unnecessary effort and cost for its implementation. The main characteristics of each technique are summarized in the following table.

Aspect	Bonding	Mechanical clamping
Stability	Very good Although outgassing and aging might be sources of instability.	Good/Fair The motion is constrained through friction. If the external load is too high, the component will start moving.
Required time	Requires several days.	Requires a few hours.
Required effort	Requires many steps. Additional equipment and experience are necessary.	Requires only a few steps.
Repairability	Very difficult	Easy
Performance under thermal loads	Good/Fair The most common failure mode is thermal loading.	Good The compensation of thermal stresses is relatively easy.
Performance under mechanical loads	Good If the bondline is properly sized.	Good/Fair The most common failure mode is mechanical loading.

Table 4.2. General characteristics of bonding and mechanical clamping.

In the case of the SLAO system a tradeoff between the two mounting techniques is presented in the following table. For this system cost is the driving parameter, followed by system performance. Therefore, all criteria associated with cost receive the highest weight (5). Stability is directly linked to performance; thus, the value of the corresponding weighting factor is 4. Lastly, although the performance of every method under thermal and mechanical influences greatly the overall performance of the system, the former can be controlled through the selection of the most suitable materials and the generation of the appropriate geometries in the design phase. For that reason, the last two criteria receive a weight equal to 3.

Criteria	Weighting factor	Bonding	Mechanical clamping
Stability	4	1	0
Required time	5	-1	1
Required effort	5	-1	1
Repairability	5	-1	1
Performance under thermal loads	3	0	1
Performance under mechanical loads	3	1	0
Results		-8	18

Table 4.3. Tradeoff for optics mounting techniques.

Based on the result from this tradeoff, mechanical clamping is the most advantageous technique for the mounting of the optical components in the SLAO system.

4.2.2 Optical components in the SLAO system

In the following tables all optical components of the SLAO system are listed together with their dimensions and approximate masses. All optical components are made out of BK7 and all mirrors are plane and most of them have an aspect (diameter to thickness) ratio of 6:1. More information about the shape and clear aperture of the optical components can be found in Appendix A.

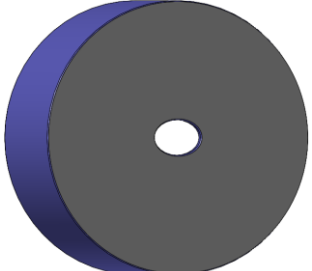
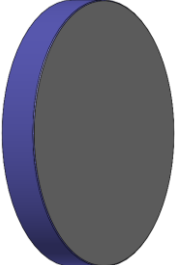
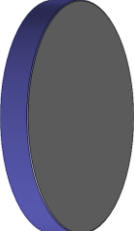






	Component	Mechanical dimensions [mm]	Mass [kg]
M1		536 x 402 x 90	33.500
M2		405 x 300 x 68	16.500
M3		355 x 215 x 56	8.000
M4		50 x 8	0.040
M5		65 x 10	0.085
M6		95 x 68 x 15	0.193
M7		45 x 8	0.032
M8		40 x 8	0.025
M9		40 x 6.5	0.020

Table 4.4. List of all mirrors in the SLAO system.







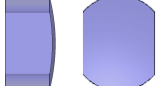



	Component	Mechanical diameter [mm]	Mass [kg]
L1		345	6.000
L2		155	0.900
L3		125	0.250
L4		125	0.280
L5		85	0.080
L6		85	0.200
L7		40 x 30	0.056
L8		38	0.015
L9		30	0.023
L10		30	0.004

Table 4.5. List of all lenses in the SLAO system.

Based on the shapes of the optical components, as presented in the two tables above, all but M1, M2, M3, M6 are axisymmetric. The component L7 is highly oversized in the vertical direction, however, the clear aperture remains axisymmetric. Rotational symmetry renders these components insensitive to a rotation about the optical axis; thus, there is no need to control this DoF. This property becomes important when considering the different design options for the holding of the optical components. Nonetheless, if the appropriate margins are applied for the definition of the mechanical dimensions, small rotations about the optical axis have no impact on the performance of the optical components.

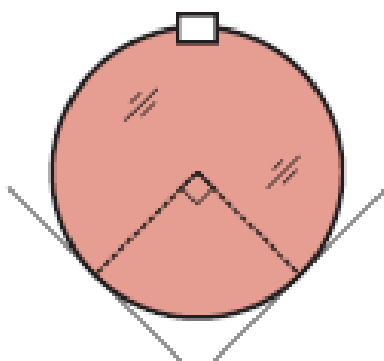
4.2.3 Mirror mounting concept selection

In the following subsections various concepts for the mounting of both large, non-metallic, vertical mirrors and small mirrors are discussed.

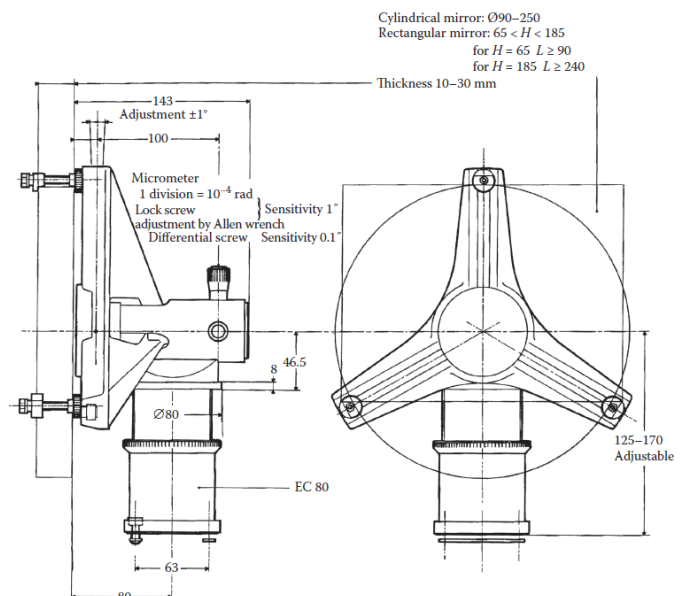
4.2.3.1 Mounting of large, non-metallic, vertical mirrors

The classification system determining whether a mirror is considered small or large is not rigorously defined; in fact, there are two criteria that are most commonly used. The first criterion is based on the handling of the component and the second on its self-weight deflection (Yoder & Vukobratovich^[29], Vukobratovich & Yoder^[30]). Assuming an aspect ratio of 6:1, mirrors which are up to 370 mm in diameter are considered small, while the range from 370 mm to 500 mm defines the transition from small to large mirrors. In this thesis, the mirrors M1, M2 and M3 are regarded as large.

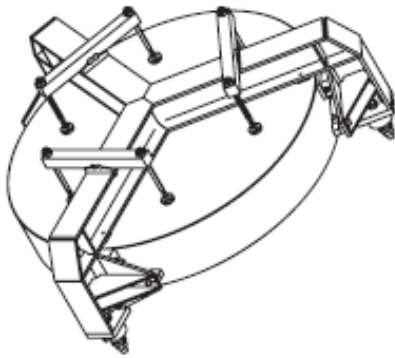
Despite the size ambiguity, the consensus view regarding the mounting of larger mirrors is that it is often quite complex and expensive. In the following figures, different concepts are illustrated for the mounting of relatively large, non-metallic mirrors, whose optical surface is perpendicular to the optical axis.



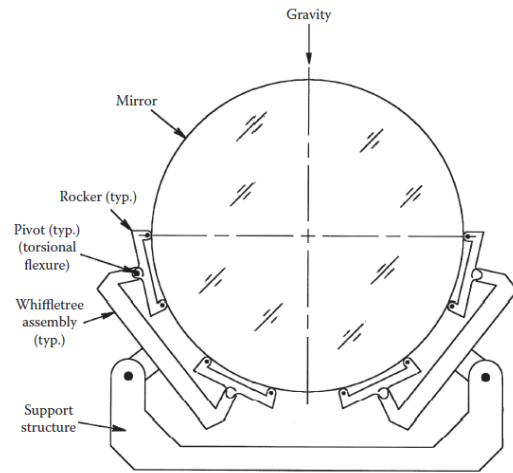
(a) V-mount: the rim of the mirror is supported at two locations, 90° apart. A safety clip at the top of the mount provides axial support. The rear side of the mirror is usually supported by a three-point support [28].



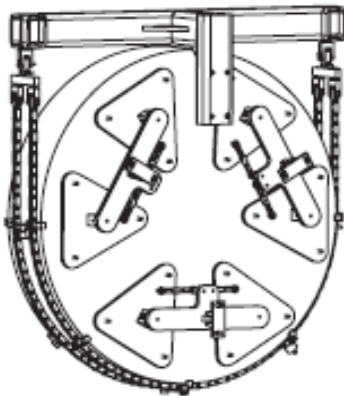
(b) A commercial V-mount which can support circular or rectangular mirrors of various sizes. Tilt and translation are adjustable [29].



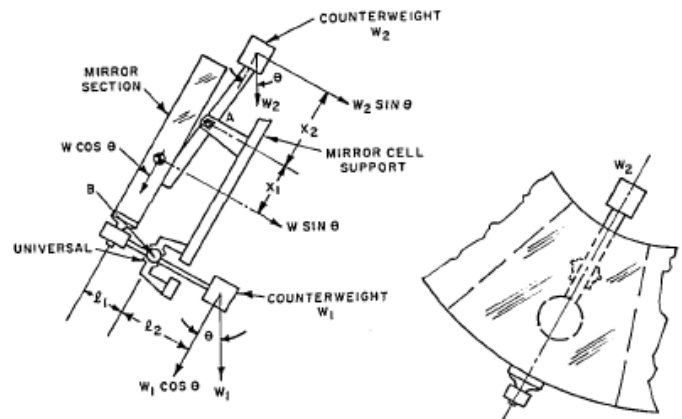
(c) Whiffletree mount: the mirror is supported laterally and axially at multiple points [28].



(d) Whiffletree mount providing lateral support for the mirror. Gravity acts as the nesting force that keeps the component in position [29].



(e) Dual roller-chain: the mirror is supported laterally by means of two chains [28].



(f) Counterweight support: the mirror is actively supported by weighted levers. The levers can self-adjust for different mirror orientations [31].

Figure 4.9. Mounting concepts for the support of large, non-metallic, vertical mirrors.

A V-mount is a relatively simple solution for the mounting of large, vertical mirrors. It can be realized in a number of ways, depending on the application. For instance, the contacts might be cylindrical posts, as illustrated in view (b) of Figure 4.9, or spheres. In the latter case, even though the position accuracy is higher, the point contacts might lead to high contact stresses. Moreover, the upper post must provide (apart from the nesting force) a degree of compliance (e.g. through a spring) to compensate for variations of the external loads acting upon the component; for instance, due to temperature variations or acceleration. In the contrary case, the component would be overconstrained, which can lead to position inaccuracies and difficulty in predicting the component's mechanical behavior under stress.

Whiffletree mounts comprise a system of lever mechanisms, which are arranged in a cascade fashion. The contact points support a mirror at multiple locations, leading to an even distribution of the applied constraints in space. Furthermore, if the friction at the contact points is minimized (or ideally eliminated),

the applied load is evenly distributed at the contacts. Similar to the V-mount, if the areas of these contacts are relatively small, then the mounting is semi-kinematic. Despite the advantages of this mount, its design is quite complex and thus expensive. In addition, due to the cascade configuration, the requirements in space are relatively high.

Roller chains provide lateral support for the mirror with low friction and allow for a rotation about its axis. These constraining elements are commercially available at a low cost and in different sizes and load capacities. Moreover, the assembled system does not demand much space. Nevertheless, due to the point contact between the rollers and the mirror's rim high stresses are to be expected.

The use of counterweight supports provides optimum performance in cases where the supported mirror does not have a fixed orientation. The self-adjustment is possible with the use of either ball bearings or flexures, with the latter providing higher position accuracy due to the elimination of friction. However, these active supports are often very complex and expensive.

In the following Pugh matrix, a tradeoff is made for the selection of the most suitable mounting concept for the large mirrors in the SLAO system. The counterweight support is not included in the evaluation, since a variation of the orientation of any of the mirrors in SLAO is not necessary. The weighting factor can take values from 1 to 5. The cost receives that highest weighting factor, followed by the volume and dynamic performance, since they determine the feasibility and health of the system. Lastly, the position accuracy receives a weighting factor equal to 3, because through the shimming process the alignment of the component is still possible.

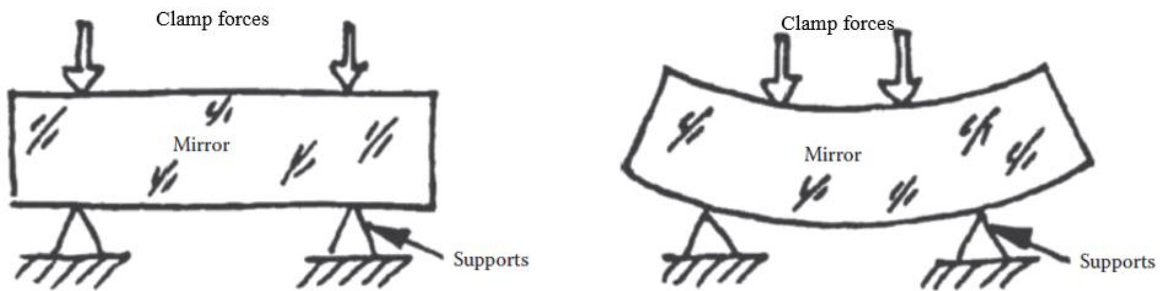
Criteria	Weighting factor	V-mount	Whiffletree mount	Roller chain
Cost and complexity	5	1	-1	1
Position accuracy	3	0	1	-1
Volume	4	1	-1	1
Dynamic performance	4	0	0	-1
Results		9	-6	2

Table 4.6. Tradeoff for the selection of the mounting concept for the large mirrors in the SLAO system.

Based on the above tradeoff the V-mount has received the highest score and is therefore considered the most suitable concept for the mounting of the large mirrors in the SLAO system.

4.2.3.2 Small mirrors

Small mirrors are often mounted in a semi-kinematic way. Such a mount involves a well-defined reference surface or surfaces on which the component rests, and one or more elements that provide the preload force (e.g. springs). In order to avoid the development of bending moments, which result in deformation, it is recommended that the lines of action of the clamping forces are perpendicular to the faces of the component and pass through the support points, located on the opposite side. This arrangement and the result of a deviation from it are presented in *Figure 4.10*.

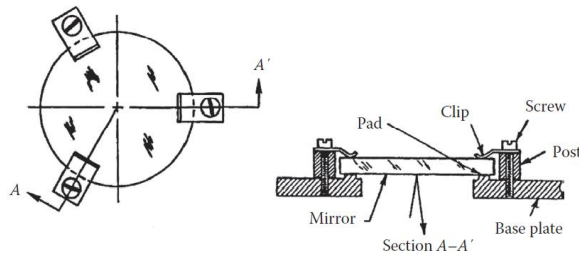


(a) The preload and reaction forces from the supports are colinear. No bending moments are developed.

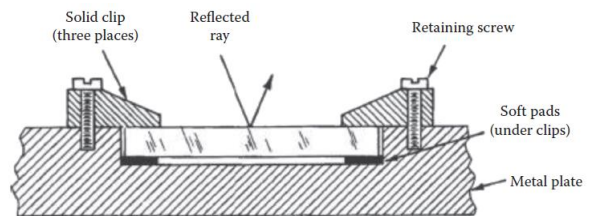
(b) The distances between the preload and reaction forces generate bending moments that deform the component.

Figure 4.10. Application of the clamping forces [32].

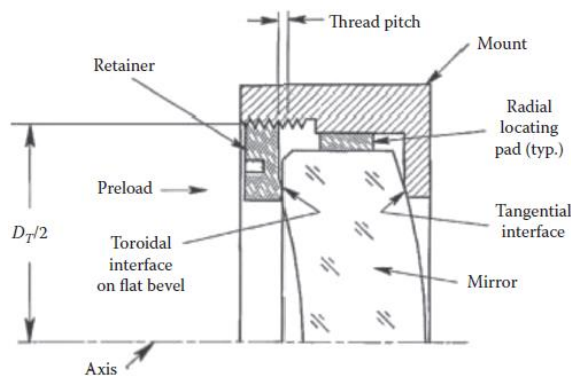
In the following figure various design configurations, which are based on the above-described mounting principle, are illustrated.



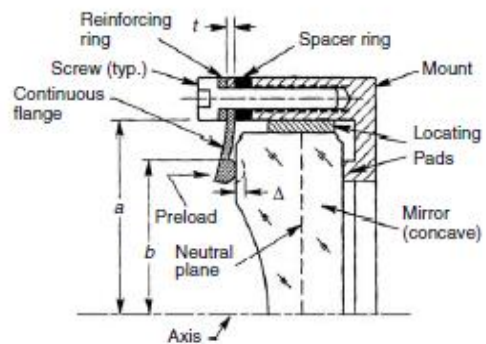
(a) Semi-kinematic mounting of a plane mirror. The preload is applied by three spring clips against three coplanar lapped pads.



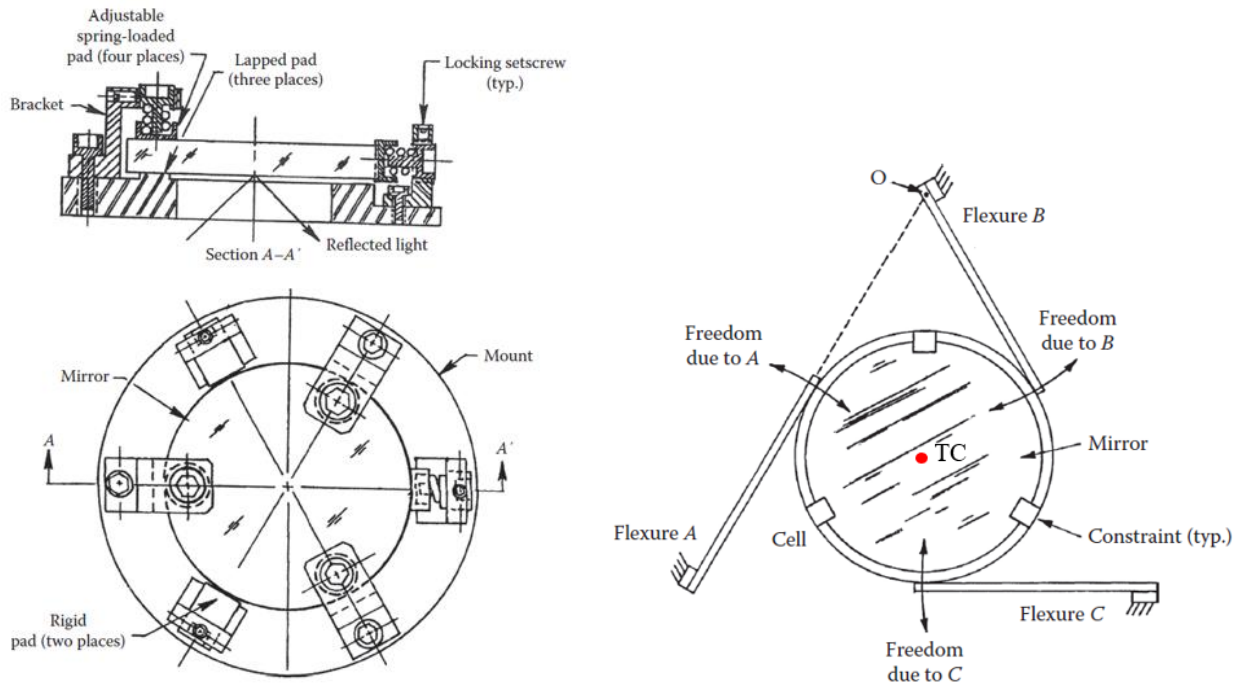
(b) Semi-kinematic mounting of a first-surface mirror. The rigid clips press against three soft, resilient pads.



(c) Mounting of a second-surface, meniscus-shaped mirror. The preload is applied through a threaded retainer.



(d) Mounting of a first-surface, concave mirror. The preload is applied through a continuous flange.



(e) Semi-kinematic mounting of a plane mirror. The component is preloaded with three springs in the axial direction and with one spring in the radial direction.

(f) In-plane (radial) flexure mounting of a plane circular mirror.

Figure 4.11. Mounting concepts for the support of small mirrors [32].

The mounting concepts presented in views (a) and (b) of Figure 4.11 constrain the translation along the optical axis, tip and tilt. The lateral movement and rotation about the optical axis are constrained only by friction; thus, if the component experiences high external loads it might shift from its original position. This, however, is not a problem if the component is insensitive to these DoFs. In view (a) the reflecting surface can be further protected against scratching (apart from the lapping of the reference surfaces) by adding Kapton or Mylar foil between the optical component and the pads. An advantage of concept (b) is that flatness and thickness variations of the mirror or the mount can be accommodated by the soft pads. Nonetheless, compression set and aging of the pads might influence the magnitude of the applied preload.

In (c) and (d) the lateral movement of the component is constrained as well and the only DoF remaining is the rotation about the optical axis. In (c) the mirror rests on the tangential interface, provided by the mount, while the flat bevel on the front side of the component is in contact with a toroidal interface. In (d) the mirror is pressed against the reference surface of the mount by a flange. This flange exerts a preload force, whose magnitude depends on the flange dimensions (inner and outer radii and thickness) as well as the mechanical properties of the selected material (Poisson's ratio and Young's modulus). It is worth noting that the design illustrated in (c) requires additional tooling for the application of a well-defined tightening torque.

If temperature variations are expected, then compliance should be introduced in the design of the mount. For instance, in (c) and (d) the radial locating pads might not fit anymore inside the gap between the mirror and the mount for large temperatures differences. The solution presented in (e) compensates for the effect of a temperature change. This design includes two constraints in the radial direction (hard stops), providing a spherical-contact interface, and a spring for the application of the preload in the same direction.

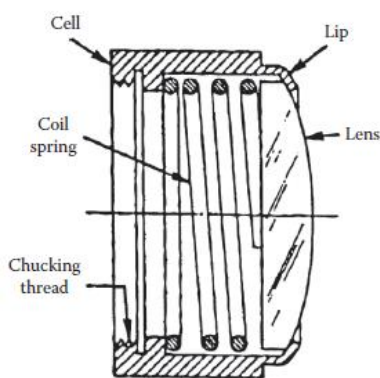
Generally, the constancy of the applied axial preload may be compromised by temperature variations; namely, the differential expansion or contraction may decrease or increase the preload. The selection of materials with similar CTEs and/or compliance for the preloading of an optical component can mitigate the problem. In addition, a proper choice of the interfaces, the dimensions and the thread class (the fit in the retainer threads), if a threaded retainer is used, can ensure minimal contact stresses.

Lastly, in (f) flexures are used for the mounting of a small circular mirror. This configuration guarantees that any differential thermal expansions of the mirror in its cell and the mount will not result in deformations of the optical component. Also, provided that the three flexures are of equal length, the optical axis passes through the Thermal Center (TC) of the system at all times; thus, misalignments due to temperature variations can be prevented.

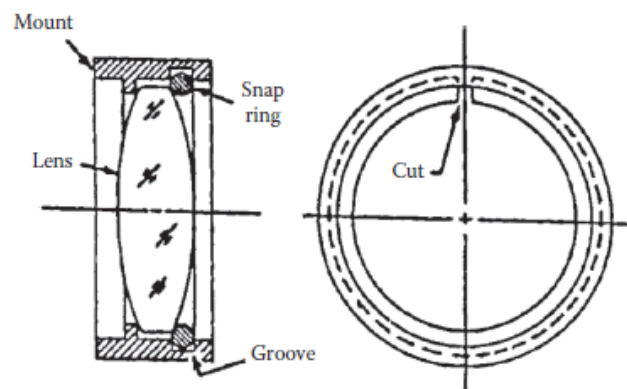
Although a common approach has been selected for the mounting of the larger mirrors M1, M2 and M3, the selection of the most suitable concept for the design of the small-mirror mounts in the SLAO system will be examined separately, given that the boundary conditions of every component differ. More specifically, the selection will be based primarily on the space available, the required preload for every optical component and the expected optomechanical performance.

4.2.4 Lens mounting concept selection

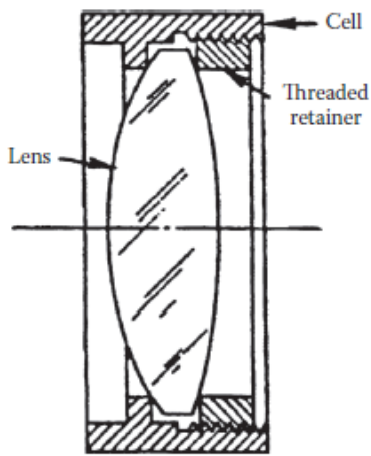
Even though plane mirrors are insensitive to lateral motion, the decentering of a lens can affect its performance. Generally, in the case of lenses the decenter and tip/tilt of the optical axis relative to the mechanical axis might be the result of fabrication error of either the lens, or its mount, or the combination of both, as discussed by Yoder & Vukobratovich^[32]. Depending on the required position accuracy, different design concepts can be found in literature. The following figure provides an overview of the most common configurations. It can be observed that in some cases the designs of the lens mounts are similar to the earlier-discussed mounts for small mirrors.



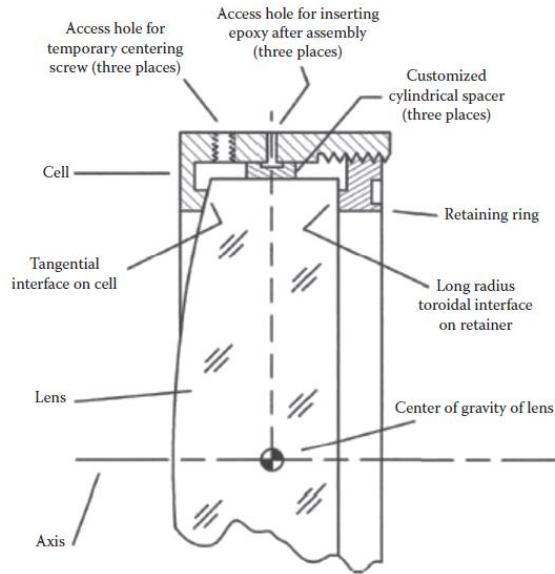
(a) Burnished-in lens mounting. The lens is pressed against the lip with a coil spring.



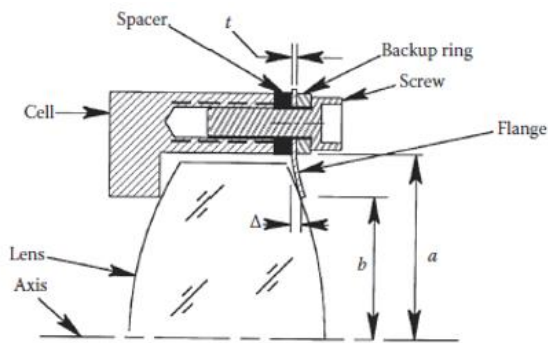
(b) Lens mounting with a snap ring of a circular cross section.



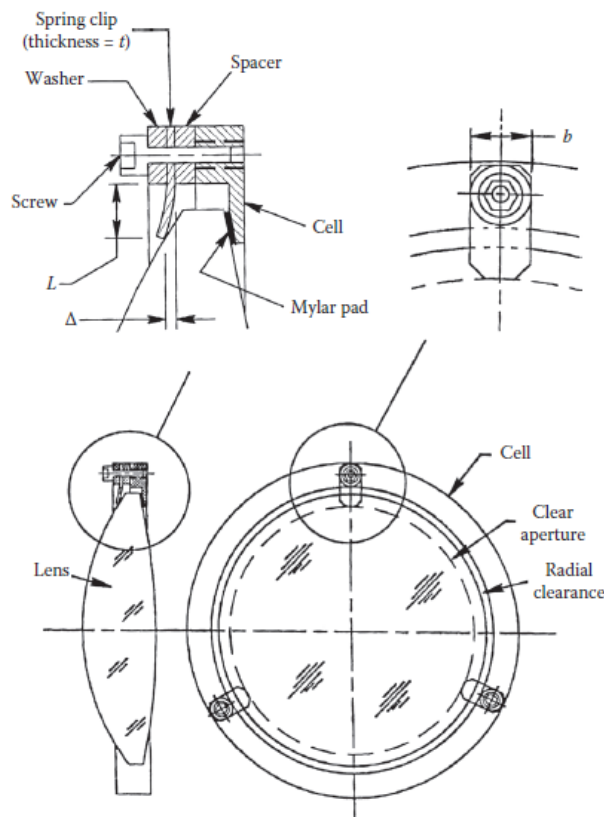
(c) Lens mounting with a threaded retainer. Here the contact interfaces are sharp corners.



(d) Mounting of a plano-convex lens with a threaded retainer. Lateral adjustment is possible with temporary centering screws.



(e) Two concepts of mounting a lens in a cell. A flange-type retainer exerts the axial preload on the optical component.



(f) Lens mounting in a cell. The lens is preloaded locally with three radially oriented cantilevered spring clips.

Figure 4.12. Mounting concepts for the support of lenses [32].

The design presented in view (a) of Figure 4.12 provides a relatively low position accuracy. However, it is inexpensive and performs well if the lens is under stress due to external loads or subjected to shock, thanks to the compliance offered by the coil spring.

In view (*b*) the snap ring is mounted inside the machined groove on the inner side of the cell. Similar to the concept presented in view (*a*), the achieved position accuracy is relatively low, but the design is simple and inexpensive. However, compliance is not included; thus, the preload may vary if the ambient conditions are not stable. The disassembling of the system is very difficult, because the removal of the snap ring from the groove is quite cumbersome.

The concept presented in view (*c*) is an example of “surface-contact” mounting (as opposed to “rim-contact” mounting), based on which the polished optical surfaces are used for the mounting, rather than the lens rim or a bevel. The radial clearance existing between the lens rim and the inner diameter of the mount shall guarantee that there is no contact between the two surfaces at any time. The advantage of the surface-contact mounting is that it allows for the relaxation of some manufacturing tolerances, since only the already relatively accurate polished optical surfaces are used. In view (*c*) the tightening torque applied to the threaded retainer provides the axial preload that presses the lens against the contacting mechanical interface of the cell. This design offers the possibility of an easy assembling and disassembling of the system. However, additional tooling is required for the verification of the tightening torque. Furthermore, the threaded retainer might become loose due to temperature variations, vibrations and/or shock.

Similar to case (*c*), the concept represented in view (*d*) uses a threaded retainer for the clamping of the lens. In general, lenses with relatively short radii of curvature may self-center to the mechanical axis of the mount. However, when the radius or radii of curvature are very long, self-centering is quite difficult in practice; therefore, active centering might be necessary. The lens in view (*d*) is a plano-convex; thus, the design provides the possibility of lateral alignment with the aid of temporary screws and curved spacers, which are centered axially at the plane of the lens’s CoG, so that moments are not introduced. When the centering of the lens has been completed, the axial preload is applied and the curved spacers are locked in position with the use of an adhesive. Sometimes, the lens is fixed at the desired position only with adhesive (without the use of curved spacers). Furthermore, Lamontagne & Desnoyers^[33] and Lamontagne et al.^[34] propose two innovative ways in which passive centering is possible for lenses with long radii of curvature, i.e. for small clamping angles. Based on these methods, either the thread angle or the radius of curvature of a spherically shaped threaded retainer can be calculated such that the mount-induced tilt and decenter of the lens are minimized. In any case, if temperature variations are expected CTE mismatches are to be avoided.

Instead of a threaded retaining ring, other elements can be used for the application of the axial preload. In view (*e*) two concepts are presented, where a continuous flange is used for the clamping of a lens. In the upper view the flange is fixed to the lens cell with multiple screws, while in the lower view it is constrained with a treaded cap. In both cases spacers of specific thickness are used to control the deflection of the flange and thus the axial preload. In the first concept, the maximum bending moment of the flange is located near the screw heads. Therefore, a backup ring is used to reduce the bending of the flange at this location and also to stiffen its rim. Moreover, similar to the concepts depicted in views (*c*) and (*d*), the concept using the treaded cap requires additional tools to ensure that the applied tightening torque is well-defined.

Finally, the concept presented in view (*f*) uses three cantilevered spring clips for the application of the axial preload. The lens is pressed against three thin Mylar pads, which are attached to the inner surface of the cell. Provided that the surface areas of the pads are small, the design is considered semi-kinematic. Similar to the concept in view (*e*), the deflection of the cantilevered springs is defined by the spacer thickness. The Mylar pads offer a degree of compliance in the system (albeit small), which allows for the relaxation of the manufacturing tolerances of the cell and renders the lapping of the shoulder surface

unnecessary. Depending on the lens geometry, different spring clip interfaces can be used, as discussed by Yoder & Vukobratovich^[32].

The selection of the most suitable mounting concept for the design of the lens mounts inside the SLAO system is made again with the aid of a Pugh matrix. It should be noted that for this tradeoff no distinction has been made between the use of a continuous flange and spring clips, because the selection among those two depends on the application; i.e. on the required stiffness (a continuous flange has a higher stiffness than a spring clip for a certain thickness). For the following tradeoff the weighting factor can take values between 1 and 5. The weighting factors are assigned to the various criteria based on the motivation discussed in subsection 4.2.3.1.

Criteria	Weighting factor	Burnished-in	Snap ring	Threaded retainer	Continuous flange or spring clips
Cost and complexity	5	1	1	0	0
Position accuracy	3	-1	-1	0	0
Volume	4	-1	1	1	1
Disassembling possibility	4	-1	-1	1	1
Dynamic performance	4	1	-1	0	1
Results		-2	-2	8	12

Table 4.7. Tradeoff for the selection of the mounting concept for the lenses in the SLAO system.

It should be mentioned that the position accuracy of the mounts using either a threaded retainer, a flange, or spring clips can be increased with the aid of radial centering screws, as discussed in the case presented in *Figure 4.12(d)*. Also, depending on the shape of the flange or spring clip, the cost and complexity of the design may vary.

Most of the designs discussed above are realizations of the “surface-contact” mounting concept, since the contact is established between the clamping element or the cell and the polished surfaces of the lens. For that reason, it is important to define the clearance between the clear aperture and the mechanical diameter, which can be used for the mounting of the optical component. According to Fischer et al.^[35], the difference between the mechanical diameter and the clear aperture should be at least 2 mm, or 5% of the aperture. Between those two limits the greatest value is to be used. Based on this definition, the size of the coated areas can be determined as well, as illustrated in *Figure 4.13*. In this figure, the term “diameter” refers to the mechanical (or physical) diameter of the component and the “mechanical inner diameter (ID)” defines the location on the polished surface where the lens registers against the mount.

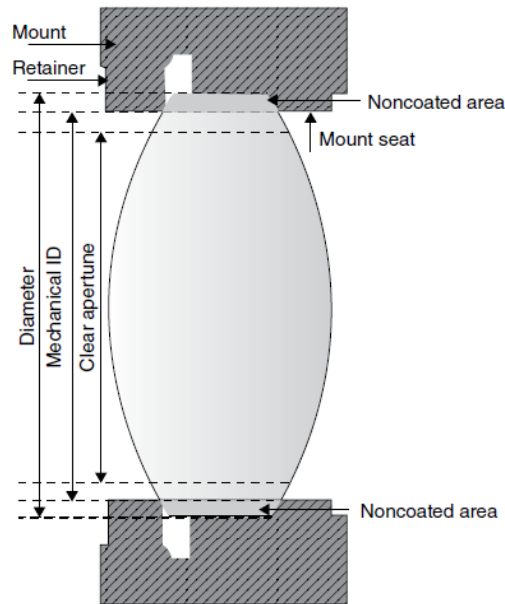
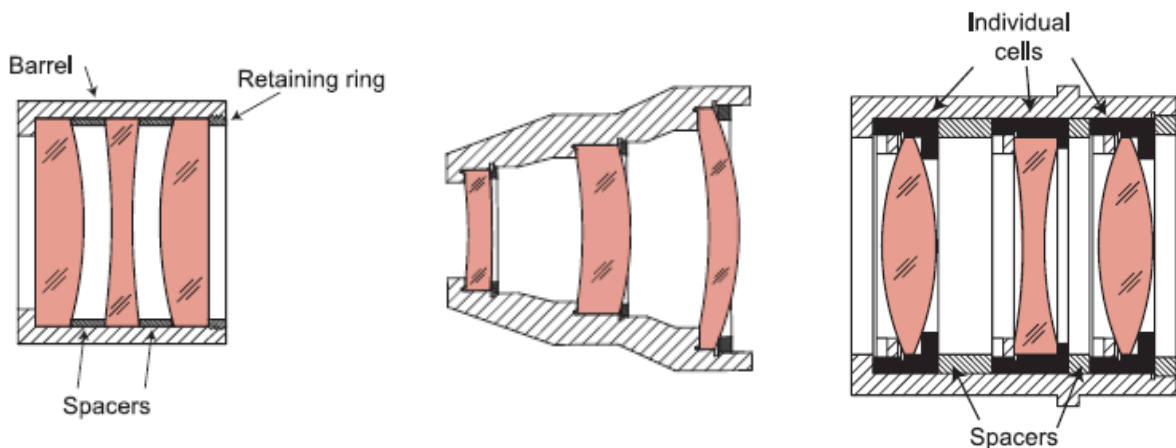


Figure 4.13. Definition of the clear aperture, over which fabrication, coating quality and mounting clearance are specified [36].

4.2.5 Multielement mounting concept selection

The above discussed mounting concepts can be generalized for the mounting of multiple lenses in a single cell (or barrel). Such a mounting configuration is relevant for some of the lenses in the SLAO system, such as the L3 and L4 (Figure 4.4). In this arrangement, the positions of the lenses can be defined either by precision spacers or by machined seats in the barrel. In the following figure three different configurations are presented.



(a) Straight-barrel design. Lenses of the same diameter are separated by spacers.

(b) Stepped-barrel design. Lenses of different diameters rest on machined seats and are held in position with retaining rings or spacers.

(c) Subcell mounting. Individual lenses are mounted in their own subcells. The subcells are then inserted into the barrel.

Figure 4.14. Multielement mounting in a common barrel [28].

The design presented in view (a) is quite simple, inexpensive and requires low integration effort. In this design concept, the position accuracy of the lenses is defined by the manufacturing tolerances of the spacers. The stepped-barrel design, illustrated in view (b), allows for the integration of lenses of different

sizes in a single barrel. The manufacturing of such a barrel is more complex than a straight one, given that the seats have to be machined precisely; nonetheless, the achieved position accuracy of the lenses is relatively high. For both the straight- and the stepped-barrel design the position accuracy in the lateral direction can be increased with additional lateral adjustment. In the case of the subcell mounting (view (c)) every lens is centered in its subcell and then integrated into the barrel. The interference fit between the subcells and the barrel ensures that the lenses remain centered. Clearly, the inner diameter of the barrel needs to be manufactured very precisely. The manufacturing and integration effort of such a system is quite high; however, the achievable precision is very high.

The selection of the most suitable barrel design for the mounting of multiple lenses inside the SLAO system is made with the aid of a Pugh matrix. For this tradeoff the weighting factor can take values between 1 and 5. Similar to other cases, the cost and integration effort (which is often related to cost) receive the highest weighting factor. Moreover, while for the selection of the most suitable design for the mount of individual lenses the weighting factor for the position accuracy was 3, for the mounting of multiple components it has been raised to 4. The reason is that individual optical components are often easily accessible after integration and the correction of their position can be performed through shimming the entire assembly at a later stage. However, the mounting of multiple components in the same barrel does not allow for such interventions after integration. Lastly, the possibility of disassembling the integrated components is also important, because if they are not accessible anymore (e.g. if they are glued to the barrel), repairs or cleaning of the optical surfaces become impossible. For that reason, a weighting factor equal to 4 is assigned to this criterion.

Criteria	Weighting factor	Straight barrel	Stepped-barrel	Subcell mounting
Cost and complexity	5	1	0	-1
Integration effort	5	1	1	-1
Position accuracy	4	0	0	1
Disassembling possibility	4	1	1	-1
Results		14	9	-10

Table 4.8. Tradeoff for the selection of the barrel design for the mounting of multiple lenses together in the SLAO system.

Based on the above tradeoff, the straight barrel is the most suitable design for the mounting of multiple lenses of similar sizes in the SLAO system.

4.2.6 Axial preload and optomechanical contact interfaces

Two important parameters that define the performance of a mechanically clamped optical component are the magnitude of the applied axial preload and the shape of the contact interfaces. The design goal is to minimize the contact stresses and bending moments, which develop in the optical component as a result of the mounting. A brief discussion pertaining to the calculation of the minimum required axial preload and the selection of the most suitable optomechanical contact interface is provided below.

4.2.6.1 Axial preload

As mentioned earlier, the application of a preload ensures that alignment is maintained even in the most severe anticipated load case, e.g. in the presence of inertia and/or thermal loads. In the case of external accelerations, an equivalent RSS of all the expected accelerations can be defined as worst case, based on which the required preload can be calculated for a component with mass m . This equivalent acceleration, a_G , is defined as a multiplier of the gravitational acceleration, g . In addition, a safety factor, f_s , (usually between 1.5 and 2) has to be included in the calculation to compensate for any approximations and potential design uncertainties. Thus, the required preload is:

$$F = m \cdot a_G \cdot g \cdot f_s \quad (4.1)$$

For mount designs that are based on the “surface-contact” principle, the axial preload is often applied to a curved (usually spherical) surface. In the presence of a radial acceleration a_G , the required axial preload that can prevent the radial movement of the component is defined as (Yoder & Vukobratovich^[32]):

$$F = \frac{m \cdot a_G \cdot g \cdot f_s}{\mu} \cdot \cos^2(\alpha) \quad (4.2)$$

where μ is the coefficient of static friction between the mechanical interface and the optical component, and α is the clamping angle, as shown in the following figure (in the right view a plano-convex lens is considered).

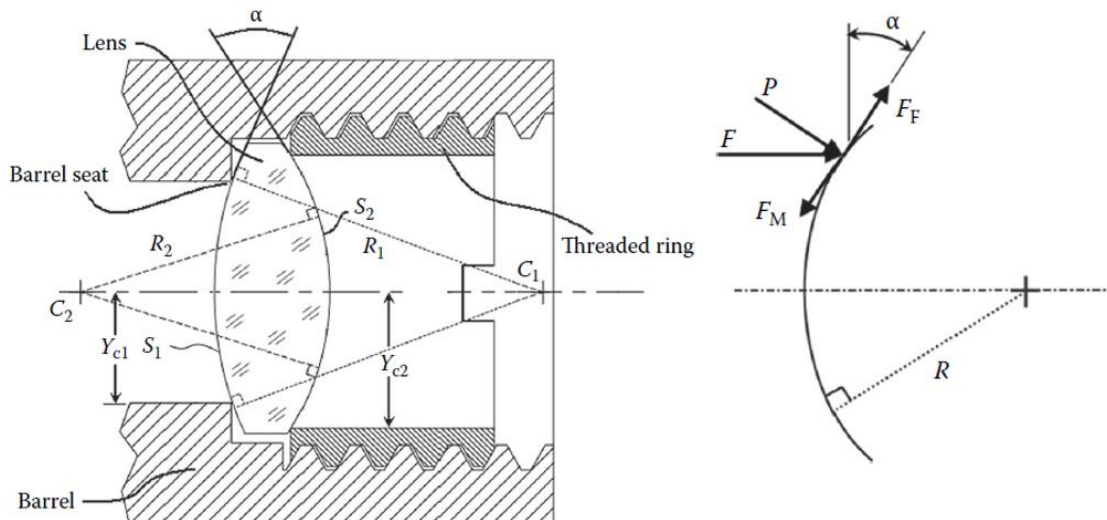


Figure 4.15. Clamping angle and analysis of forces acting upon a clamped lens (the reaction force due to the presence of radial acceleration is not shown here) [37].

For a lens with radii of curvature R_1 and R_2 , which is clamped at distances Y_{c1} and Y_{c2} from the axis connecting the two centers of curvature C_1 and C_2 , the clamping angle is defined as (Yoder & Vukobratovich^[32]):

$$\alpha = -\sin^{-1}\left(\frac{Y_{c1}}{R_1}\right) + \sin^{-1}\left(\frac{Y_{c2}}{R_2}\right) \quad (4.3)$$

It should be noted that the radius of curvature is positive for convex and negative for concave surfaces. In the book by Yoder & Vukobratovich^[32] the clamping angle is calculated for optical surfaces of various shapes.

In *Figure 4.15*, F represents the applied axial preload and P is the resulting pressure force acting normally to the surface of the optical component. The motion force F_M tends to center the lens as a result of the preload application and F_R is the opposing friction force. Clearly, self-centering can occur only if $F_M > F_R$, i.e. if the friction is minimized between the mechanical interface and the lens. These forces are defined as:

$$P = F \cos(\alpha) \quad (4.4)$$

$$F_M = F \sin(\alpha) \quad (4.5)$$

$$F_R = \mu P \quad (4.6)$$

From *eq. (4.2)* it can be observed that large clamping angles require lower preloads, since the high curvature of the component prevents it from becoming misaligned (self-centering effect). However, for a combination of very small clamping angles and very low friction coefficients, *eq. (4.2)* leads to high preloads, and consequently to high contact stresses.

In the case of a plane parallel plate or a lens with flat bevels on both sides, which rests on flat mechanical interfaces oriented perpendicular to the optical axis, *eq. (4.2)* becomes:

$$F = \frac{m \cdot a_G \cdot g \cdot f_s}{\mu} \quad (4.7)$$

Besides the inertia loads, temperature variations result in changes in the applied preload forces, which can compromise the alignment and/or optical homogeneity of the component, or even lead to catastrophic failure due to high contact stresses caused by differential expansion or contraction. In the case of rim-contact designs, the maximum radial contraction and expansion need to be taken into account so that sufficient radial clearance is present. For a surface-contact mount subjected to a temperature change ΔT , (significant) CTE mismatches between the materials used generate a change in the axial preload, which is calculated by (Yoder & Vukobratovich^[32]):

$$\Delta F = K_3 \cdot \Delta T \quad (4.8)$$

where K_3 is the rate of change of the preload with temperature and depends on the design.

4.2.6.2 Contact interfaces

For optomechanical designs that rely on the “surface-contact” principle the shape of the contact interfaces has an impact on the magnitude of the mount-induced contact stresses. There are four types of contact interfaces: the sharp-corner, the tangential, the toroidal and the spherical. Depending on the shape of the optical component different options are available, as presented in the following figure.

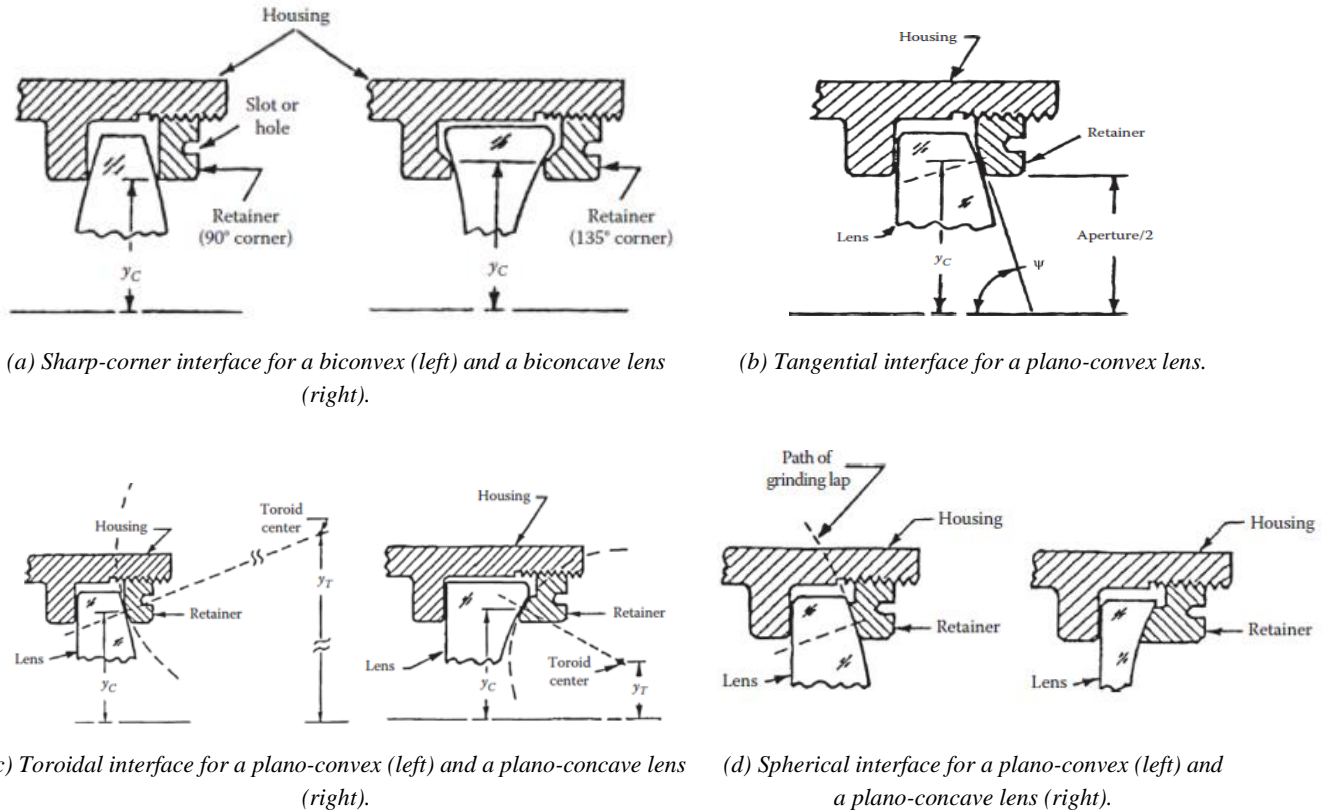
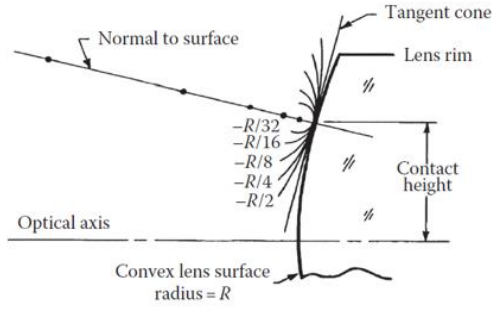


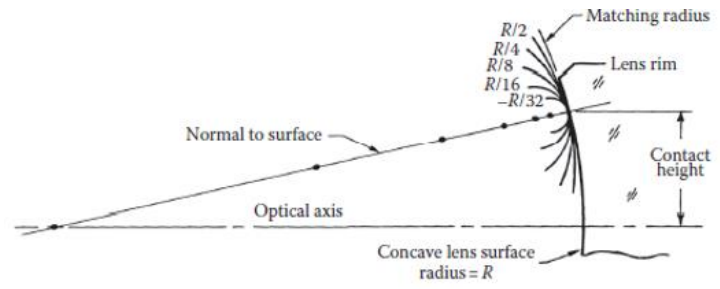
Figure 4.16. Optomechanical contact interfaces for different lens surfaces [32].

Apart from the tangential interface, which can be used only with convex surfaces, the rest can be used with all lens shapes. The sharp-corner interface can be fabricated easily and provides high position accuracy when properly manufactured; however, the resulting contact stresses can be relatively high. The tangential and toroidal interfaces require low to medium manufacturing effort and can reduce the magnitudes of the contact stresses significantly. Lastly, the contact stresses can be minimized with a spherical interface. Nonetheless, such an interface must have relatively tight manufacturing tolerances so that the lens and mount surfaces match perfectly. For that reason, the less ideal solution of a tangential or toroidal interface is often preferred if the resulting contact stresses are sufficiently low.

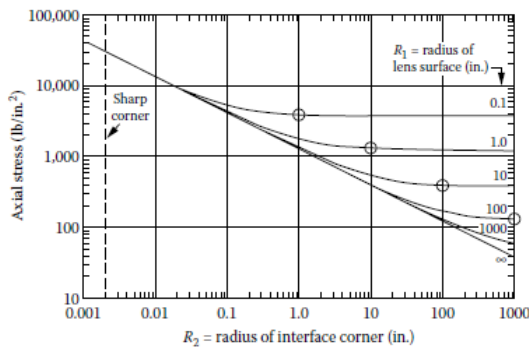
In the following figure, views (a) and (b) represent the interface shapes for different radii of the toroidal interface in the case of a convex and concave lens surface, respectively. In views (c) and (d) the impact of the interface geometry on the axial stress is illustrated both for a convex and a concave lens surface. As expected, for a constant preload the magnitude of the axial stress decreases as the radii of curvature of the lens and/or the toroidal interface increase.



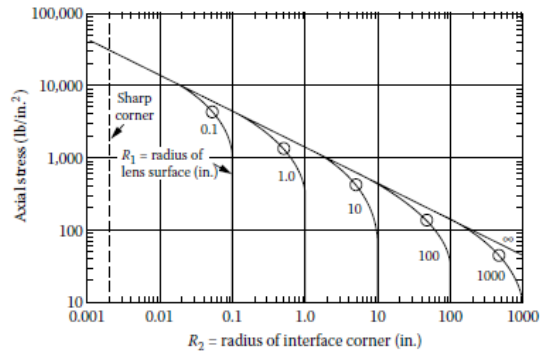
(a) A convex lens surface of radius R interfacing with convex toroidal surfaces of different radii. The tangent cone is a limiting case [32].



(b) A concave lens surface of radius R interfacing with convex toroidal surfaces of different radii. The matching radius (or spherical interface) is a limiting case [32].



(c) Variation of axial stress with toroidal interface radius R_2 for different convex lens radii R_1 and at a constant preload [37].



(d) Variation of axial stress with toroidal interface radius R_2 for different concave lens radii R_1 and at a constant preload [37].

Figure 4.17. Optomechanical contact interfaces for different lens surfaces.

For an annular contact, the peak compressive contact stress at the mounting interface is (Yoder & Vukobratovich^[32]):

$$\sigma_c = 0.798 \left(\frac{K_1 p}{K_2} \right)^{\frac{1}{2}} \quad (4.9)$$

where K_i is a function of the interface shape and is calculated for a sharp-corner, tangential and toroidal interface, respectively, as follows (Yoder & Vukobratovich^[32]):

$$K_1 = \frac{D_1 \pm 0.102}{0.102 D_1} \quad (4.10)$$

$$K_1 = \frac{1}{D_1} \quad (4.11)$$

$$K_1 = \frac{D_1 \pm D_2}{D_1 D_2} \quad (4.12)$$

In the above equations D_1 is twice the radius of curvature of the optical surface and D_2 is twice the sectional radius of the toroid. In eq. (4.10) and eq. (4.12) the positive sign is used with a convex lens

surface and the negative with a concave lens surface. A spherical interface is not included, because for perfectly matching spherical surfaces the contact stresses are negligible. If, however, the manufacturing accuracy of the interface is not sufficiently high, this assumption becomes invalid.

The variable p represents the preload per unit length of the annular contact. Thus, for a preload F and a contact height Y_c , p is given by:

$$p = \frac{F}{2\pi Y_c} \quad (4.13)$$

For a short-line contact of length b , and F_i the preload per contact (e.g. per spring clip) the above equation can be modified as:

$$p = \frac{F_i}{b} \quad (4.14)$$

The variable K_2 depends on the mechanical properties of the interfacing materials and is calculated as follows (Yoder & Vukobratovich^[32]):

$$K_2 = \frac{1-\nu_G^2}{E_G} + \frac{1-\nu_R^2}{E_R} \quad (4.15)$$

where ν_G , ν_R , E_G and E_R are the Poisson's ratios and Young's moduli of the glass and the mechanical retainers, respectively.

Besides compressive stress, tensile stress is also present at the contact interface and is directed radially. This stress is given by (Yoder & Vukobratovich^[32]):

$$\sigma_t = \frac{1-2\nu_G}{3} \sigma_c \quad (4.16)$$

Lastly, similar to the spherical contact interfaces, for accurately machined flat bevel interfaces the mount-induced contact stresses can be ignored because the area of contact on a bevel is usually sufficiently large. Nonetheless, if the contact is not perfect, then a sharp-corner interface might occur.

From *Table 4.5* it can be observed that the lenses used in the SLAO system cover all the above-discussed surface geometries. Moreover, based on the survival ambient conditions presented in *Table 3.1*, the tangential and toroidal are deemed to be the most suitable contact interfaces, otherwise the mount-induced contact stresses would be considerably high, as will be proven in Section 6.1.

4.3 Implementation of motions in the SLAO system

As mentioned earlier, one of the driving parameters for the design of the SLAO system is cost, which can be reduced if COTS components are used when possible. In this section, it is investigated whether the two translations inside the SLAO system can be performed with the use of commercially available motorized translation stages. Aside from the price of these components, their suitability for the SLAO system is mainly defined by their travel range and load capacity. Of course, other characteristics, such as the MIM, are also important and have to be taken into consideration for the selection of the best candidate.

4.3.1 Pickup mirror

In Section 4.1 it was concluded that the most advantageous way to retract the M1 is through a vertical translation. From *Figure 4.3* it can be observed that the required travel distance is relatively long (approximately 400 mm). Moreover, based on the mass of the mirror (*Table 4.4*) the required load capacity is quite high. More specifically, if a (worst-case) margin of 50% is used in order to include the mass of the mirror mount, then, for the given maximum acceleration (*Table 3.1*) and for a safety factor equal to 2, the required load capacity can be estimated as follows:

$$LC = 1.5 \cdot m_{M1} \cdot a_G \cdot g \cdot f_s \approx 3,450 \text{ N} \quad (4.17)$$

These two parameters (travel range and load capacity) are used for the preliminary search for commercially available vertical translation stages. The results of this search are summarized in the following table.

Model name (Manufacturer)	Travel range [mm]	Vertical load capacity [N]	Horizontal load capacity [N]
M-IMS300V (Newport) ^[38]	300	400	400
VTS300-200 (Aerotech) ^[39]	200	4500	900
MOZ-300-200-H (Optics Focus) ^[40]	200	1000	n.a.
8MT195Z-340-10 (Standa) ^[41]	340	100	400
960-0115-340-2.5 (EKSMA) ^[42]	340	100	600
OSMS26-300(Z)-M6 (SIGMAKOKI) ^[43]	300	40	n.a.

Table 4.9. Commercially available vertical translation stages.

Based on the characteristics of the vertical translation stages found, none of them meets the travel range and load capacity requirements. For that reason, a vertical translation system for the retraction of the M1 needs to be designed.

In general, a motorized translation stage consists of the rails or sliders, along which the desired motion is performed, the carriage, on which the load is mounted, the power transmission system, the motor, the motor driver, the position sensors (e.g. limit switches, (opto)interrupters) and the power supply system. In

the present report the focus is placed on the first three subsystems. *Figure 4.18* presents three types of guide systems. The first two rely on different kinds of rolling bearings, which ensure a smooth and precise movement along the translation axis with low (or no) tilting. Moreover, depending on the bearing type used, the load capacity can be increased significantly. Despite their excellent mechanical characteristics, the space limitation in the case of the SLAO system renders them not a viable option. The translation system depicted in view (c) employs two sliders and a power screw for the implementation of the motion. Although this may not be as precise as the first two, it is more compact. Given that for the translation of the M1 precision in the motion is not important as long as the repeatability in reaching the upper end position can be ensured, the latter concept is selected for the design of the vertical translation system for the M1.



(a) Precision rail guides [44].



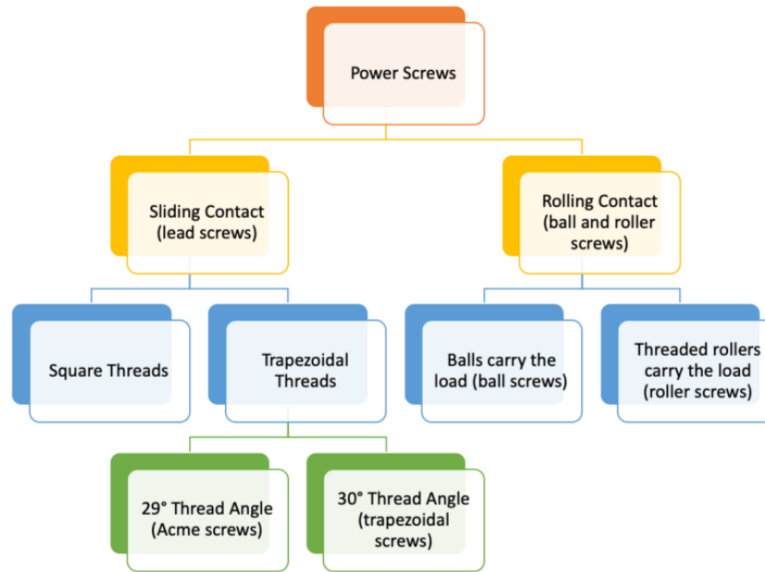
(b) Profile rail guides [45].



(c) Linear slider [46].

Figure 4.18. Examples of guide systems.

A power screw can rely on a sliding contact (lead screw) or on a rolling contact (ball screw), as illustrated in the following figure.



(a) Categorized power screws [47].



(b) Lead screw and lead nut [48].



(c) Ball screw [49].

Figure 4.19. Power screw types.

In general, lead screws are less efficient due to friction; thus, they require greater torque and consequently a larger motor. Another side effect of friction is the temperature increase during operation. Moreover, lead screws underperform in cases where high-speed translation is needed or in continuous or long cycle times. Besides that, the service life of a lead screw is not very long. On the other hand, this type of power screw is inexpensive and given that it is self-locking, theoretically, it does not require a braking system. For that reason, it is considered the best option for vertical translation systems.

By contrast, the impact of friction on the efficiency of a ball screw is negligible. As a result, lower operating temperatures are observed and longer service lives are possible. Apart from that, ball screws provide a higher accuracy and require lower torques. However, a disadvantage of the high efficiency of a ball screw is that a braking mechanism is required to prevent the occurrence of back-driving. For that reason, the ball screw is not considered a good option for vertical applications. Lastly, this type of power screw requires lubrication and is relatively expensive.

In the case of METIS, the SLAO system is not planned to be employed frequently, neither is a high-speed translation of the M1 required. Therefore, given the direction of intended motion, a lead screw is deemed a better option for the specific application.

A motorized lead screw can be used in two different configurations: the rotating screw- and the rotating nut, as presented in *Figure 4.20*. In the first configuration (view (a)), the fixed motor rotates the lead screw, which, in turn, forces the lead nut and the load attached to it to move. In that case, the rotation of the lead nut must be constrained. The rotating nut configuration (view (b)) can be implemented in two ways. In the first way, the fixed motor contains a rotating nut within its body. As a result, the lead screw and the load attached to it can move. Alternatively, the rotation of the lead screw can be constrained and the motor, to which the load is now attached, can move.

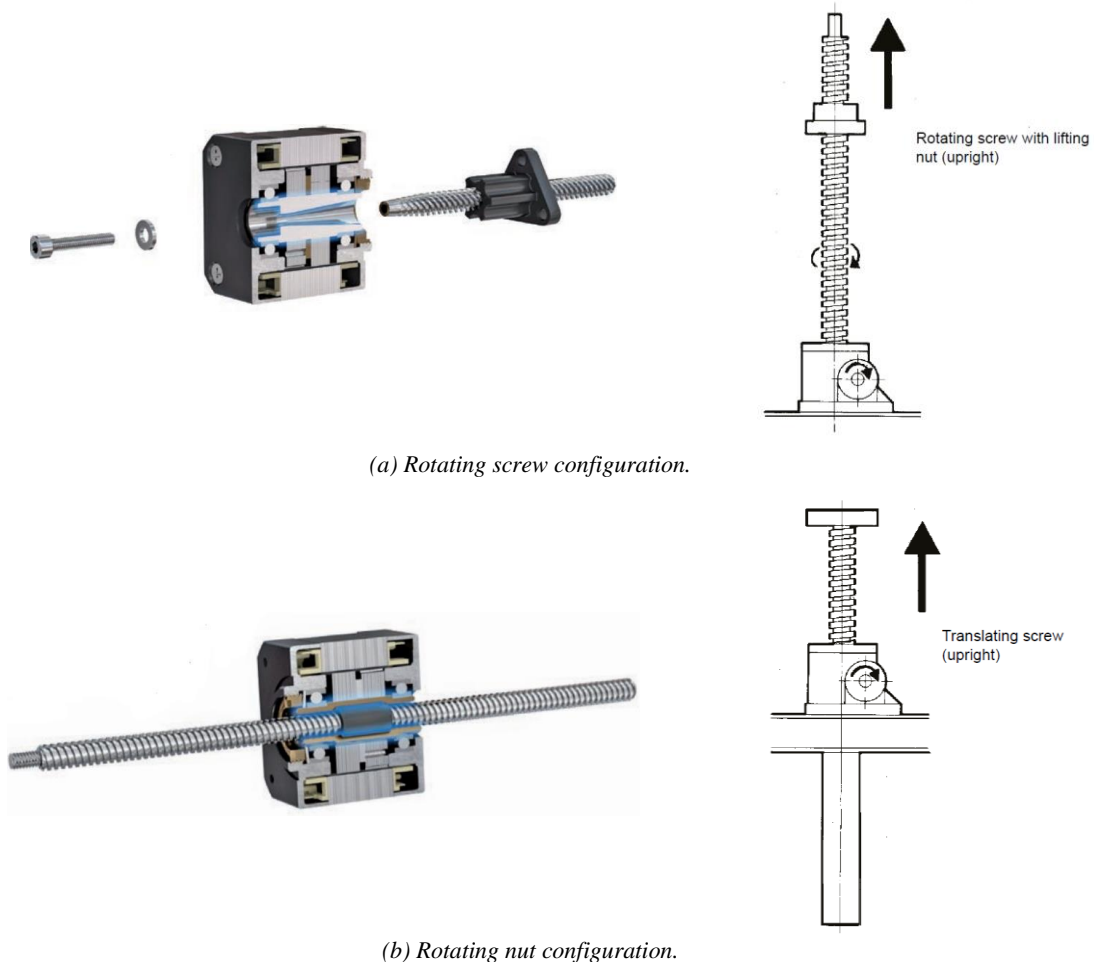


Figure 4.20. Motorized lead screw configurations [50], [51].

The second configuration with a fixed motor and a translating screw requires space on both sides of the motor; as a result, for a given envelope the travel range is reduced. The alternative of a translating motor and a fixed lead screw has the disadvantage that the cables of the motor will be moving as well, which might lead to damage of the cables and/or other parts of the system. For that reason, the first configuration is considered the best option for the vertical translation of the pickup mirror.

In all the above-discussed configurations it can be observed that the motor and lead screw are connected on the same axis. In practice, a hard connection between those two is avoided because slight misalignments will introduce lateral loads, which can damage the motor. This can be prevented if a shaft coupler is connected in between. This component is axially stiff and laterally compliant; thus, the requirements regarding the alignment between the motor and the lead screw can be relaxed. However, the use of such a component increases the demand for space in the axial direction.

Alternatively, the motor can be positioned next to the lead screw if a screw jack is used. This component comprises a pair of gears (worm and worm wheel) which causes an angular shift of the rotation axis by 90° , as illustrated in the following figure. A screw jack not only makes the system more compact, but also acts as a break, preventing a potential back-driving of the lead nut. In addition, due to the mechanical advantage provided by the gears, a smaller motor can be used. Nonetheless, the higher torque output is provided at the expense of the travel speed. Lastly, lubrication of the gears is necessary to ensure a smooth motion and prevent wear in the teeth. In subsection 5.2.1.2 the preliminary design of the vertical translation system for the pickup mirror is discussed.

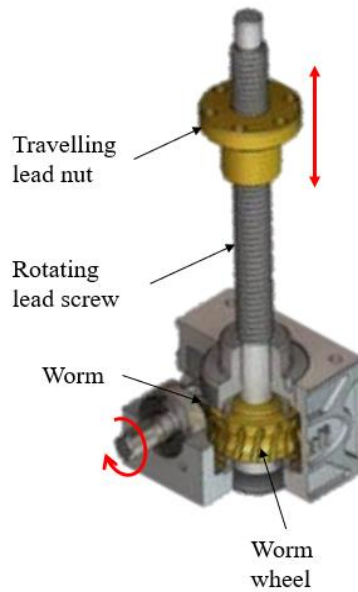


Figure 4.21. Screw jack connected to a rotating lead screw [52].

4.3.2 Zoom optics

According to the current optical design (Tripsas^[14]), the required travel range for M7 and M8 is 122.24 mm, in order for the SLAO system to be capable of covering all zenith angles between 0° and 60°. Furthermore, based on the developed CAD models of the individual components comprising this subsystem, a rough estimate of the required load capacity is 25 N. Besides that, given the volume limitation, the envelope of the translation stage has to be considered as well. These requirements are used as input for the search for commercially available horizontal translation stages for the implementation of the desired motion. The results of this search are presented in the following table.

Model name (Manufacturer)	Travel range [mm]	Vertical load capacity [N]	Horizontal load capacity [N]	Velocity [m/s]	MIM [nm]	Envelope [mm ³]
V-508.6 PIMag (PI) ^[53]	170	100	n.a.	0.7	1	80 x 25 x 405
V-551.4x (PI) ^[54]	130	150	50	0.5	0.5-2	160 x 50.5 x 420
XMS160-S (Newport) ^[55]	160	100	n.a.	0.3	1	125 x 50 x 410
DL125 (Newport) ^[56]	125	20	n.a.	0.5	75	124 x 44.45 x 290
PCR32...0135 (Prismatics) ^[57]	135	45	n.a.	0.5	n.a.	97.5 x 32 x 355
ALS1000-150 (Aerotech) ^[58]	150	500	250	0.75	5-1000	246.4 x 82.5 x 431
ANT130L-160 (Aerotech) ^[59]	160	120	100	0.35	1	130 x 45 x 440

Table 4.10. Commercially available horizontal translation stages. All stages are equipped with a position sensor.

In the above table, the model DL125 is included although its load capacity is slightly lower than the required because the latter has been roughly estimated.

Although all of the above translation stages meet the requirements, it has been decided that a customized (shorter) version of the horizontal translation stage LMS-270KSHO^[60] from PI will be used. This decision is based on the fact that the software for the motion control has been implemented for another system; thus, the know-how exists already. The main characteristics of this translation stage are presented below.

Model name (Manufacturer)	Travel range [mm]	Vertical load capacity [N]	Horizontal load capacity [N]	Velocity [m/s]	MIM [nm]	Envelope [mm ³]
LMS-270KSHO (PI)	300	500	500	0.8	50	270 x 100 x n.a.

Table 4.11. Main characteristics of the translation stage LMS-270KSHO.

It should be noted that for this translation system the specified operating temperature range is from 10°C to 50°C, while the operating temperature range of the SLAO system is from 0°C to 15°C. For that reason, it should be verified that this discrepancy does not have an adverse impact on the health and performance of the selected translation stage.

5 Preliminary (opto)mechanical design

In Chapter 4, the different design options for the subsystems and mechanical components in the SLAO system have been considered and the most suitable concepts have been selected. Based on this study the preliminary (opto)mechanical design of the SLAO system has been developed. This design is discussed in detail in the present chapter.

5.1 Design of the support structure

The preliminary design of the support structure is based on the concept presented in *Figure 4.7*. The structure comprises three 60 mm thick, vertical aluminum blocks, which are connected with eight aluminum beams^[61], as illustrated in *Figure 5.1*. The middle block has three openings for the mounting of the L1 and L2, and for the aperture between the L4 and L5. Moreover, this block carries an aluminum plate for the mounting of the M4, M5, L3 and L4.

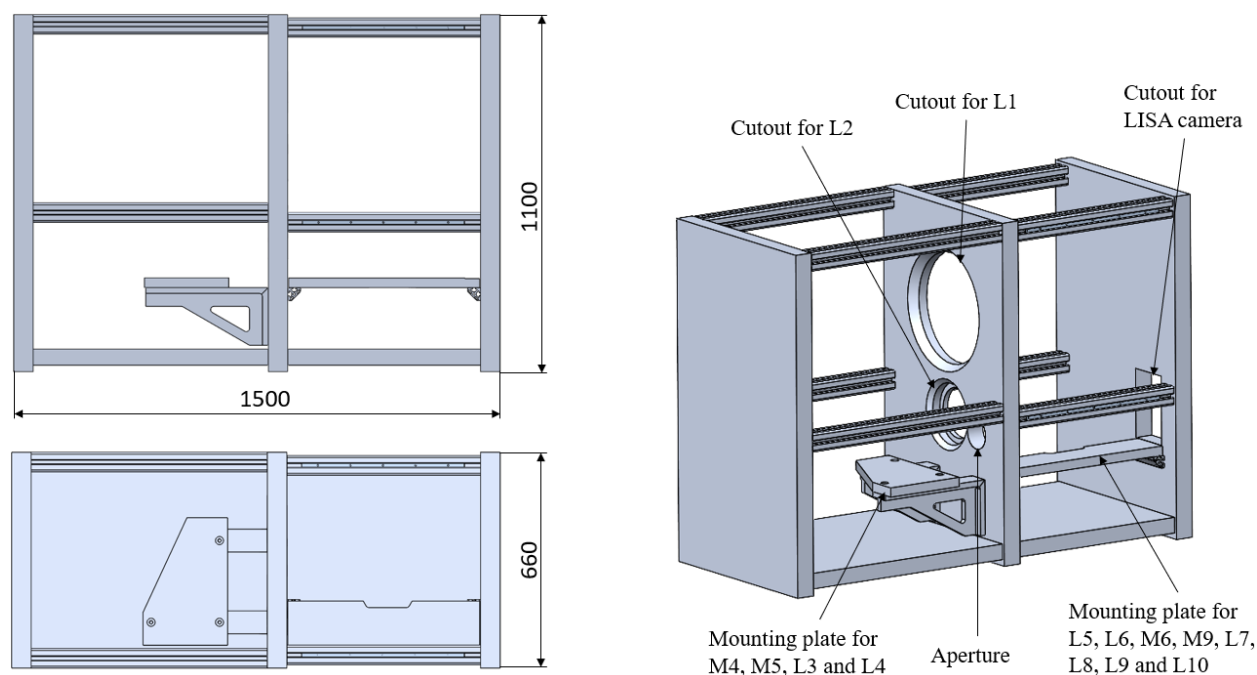


Figure 5.1. Preliminary design of the support structure.

The right block has an opening for the mounting of the LISA camera. At this stage, the mounting IF of the camera is not known, however, it would be advantageous in terms of integration and accessibility if the camera could be slid through the opening from the rear side of the right block and then mounted to it when most of the components have already been integrated. Moreover, the right block will carry the M2 and M3. Lastly, on the rear side of the middle block and the front side of the right block two aluminum beams of triangular cross section^[62] are attached, to which an aluminum plate is connected for the mounting of the L5, L6, M6, M9, L8, L9 and L10.

This design does not include the definition of the mounting IF between the SLAO system and METIS's platform. Furthermore, stiffening elements have to be added between the blocks to prevent their relative motion. Besides that, the stiffness and mass of the support structure (which is currently approximately 496.5 kg) need to be optimized with a detailed Finite Element Analysis (FEA). However, in order for the FEA results to be realistic, rough estimates of the masses and positions of the individual components and subsystems carried by the support structure are necessary. The rest of this chapter focuses on the definition of these parameters through the development of the design of all (opto)mechanical parts in the SLAO system.

5.2 Design of the (opto)mechanical components and subsystems

In the following subsections, the preliminary design of the mounts for all optical components in the system is discussed. The order in which the individual designs are presented is based on the positions of the corresponding optical components with respect to the propagation of the laser beam inside the system.

5.2.1 M1 subsystem

The M1 subsystem consists of the M1 mount and the vertical translation system. In the following subsections the two assemblies are discussed.

5.2.1.1 M1 mount

The design of the mount for the pickup mirror is based on the V-mount concept, presented in *Figure 4.9*. As illustrated in the following figure, the triangle-shaped M1 mount carries two posts on which the mirror rests. These posts consist of a metallic core and an outer layer of a material characterized by a low wear and friction coefficient as well as high Young's modulus, for instance ZrO_2 ^{[63],[64]}, to improve the position accuracy of the mount. Alternatively, a low friction and low wear coating (such as Teflon) can be applied to the metallic posts. It is worth noting that the relatively small diameter of the metallic core requires the use of a high strength stainless steel, such as X8CrNiMoAl15-7-2^[65] (EN Designation); otherwise, the core diameter has to be increased.

The nesting force is provided by two coil springs in the radial direction. These compression springs are held together in an assembly with the aid of a Clevis pin. Given that the springs are laterally compliant, two dowel pins prevent the in-plane rotation, which would have a negative impact on the contact between the spring assembly and the rim of the mirror. It is advisable that Kapton tape is added at the interface between the spring assembly and the mirror, so that any asperities on the surfaces do not generate localized stress concentrations. The magnitude of the axial preload can be adjusted with the use of shims between the M1 mount and the radial spring assembly (not shown in the figure).

In the axial direction the preload is applied by means of three compression springs, at the top end of which the mechanical contacts are located. These mechanical contacts press the mirror axially against three hard stops, each exerting one third of the axial preload on the component. Between all contacting surfaces Kapton tape is used, while the magnitude of the axial preload can be adjusted with washers. As it can be observed in the figure below, the edge of the central opening is beveled on the rear side of the mirror to prevent the occurrence of reflection artifacts. The bevel angle is equal to 47° (taking into account the orientation of the M1 relative to the science beam and the $f/\#$ of the telescope). However, this angle needs to be optimized as part of the optical design. Moreover, a recess in the M1 mount prevents

the occurrence of vignetting of the science and NGS beam. Nonetheless, the close proximity between the two (the distance is slightly over 4 mm) needs to be further investigated in terms of optical performance. In addition, threaded holes are included in the axial and lateral direction to facilitate the handling of the M1 assembly.

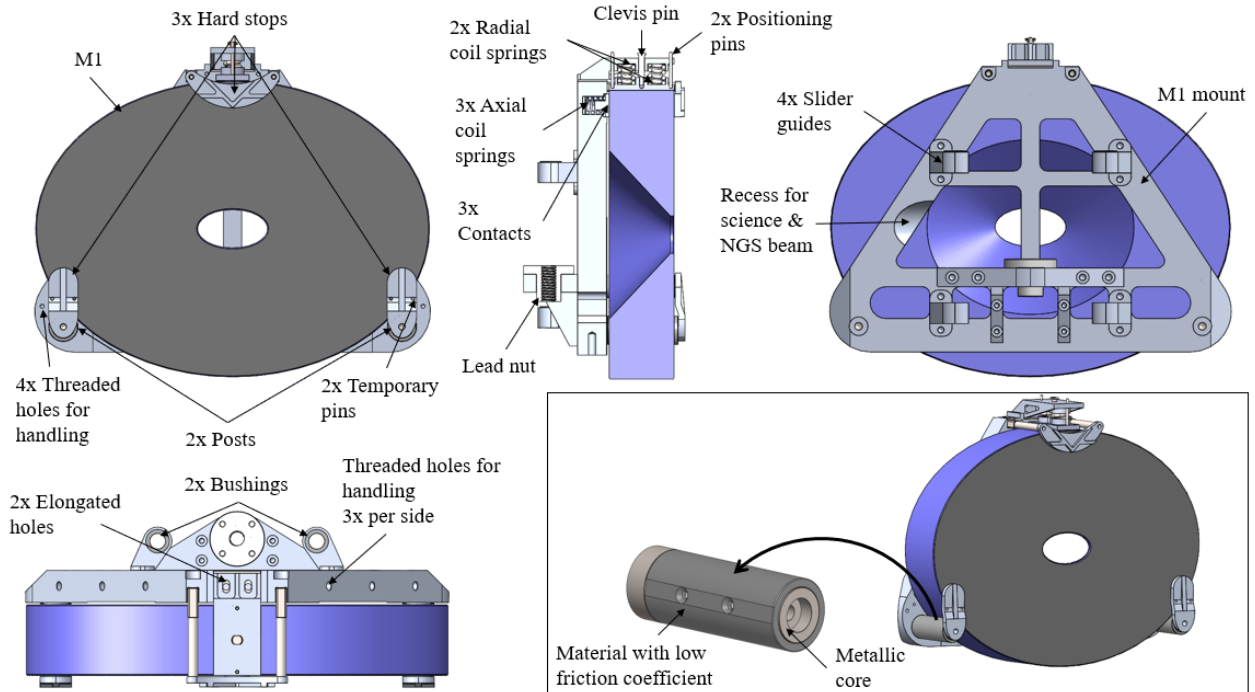


Figure 5.2. Preliminary design of the M1 mount.

On the rear side of the M1 mount a plate is attached, on which the lead nut is mounted. Furthermore, four slider guides are fixed directly to the M1 mount and in the inner surface of the two upper slider guides two bushings are inserted, so as to reduce the friction between the guides and the sliders. The bushing model is ZFM-2023-21^[66] and has been selected because of its low wear, low friction and high loading capacity. However, other models providing low wear and low friction would also be suitable for the application. The functionality of all aforementioned components is discussed in the following subsection. The total mass of the M1 assembly is approximately 46.2 kg.

5.2.1.2 M1 translation system

In subsection 4.3.1, a number of commercially available vertical translation stages have been presented and the conclusion was drawn that none of the options found fulfills the requirements in travel range and load capacity. Furthermore, the basic principles, based on which a translation system is designed, have been discussed. In this subsection the conceptual design of a vertical translation system for the pickup mirror is presented.

A motor, which is mounted on the base plate of the support structure (*Figure 5.3*), rotates a lead screw via a screw jack. The upper end of the lead screw is attached to a ball bearing, whose inner ring is preloaded for better performance. The rotation of the lead screw forces the lead nut and the load connected to it (i.e. the M1 assembly) to travel in the vertical direction. More precisely, the M1 assembly slides along two sliders, which are supported by two vertical beams. A high positioning accuracy at the upper end position of the M1 assembly can be achieved with the use of a limit switch. Moreover, two safety springs are added at the bottom ends of the sliders to keep a safe distance between the M1

assembly and the motor, e.g. during integration. A rough estimate of the mass of the M1 translation system is 40 kg. In *Figure 5.4* the M1 assembly is depicted at its two end positions.

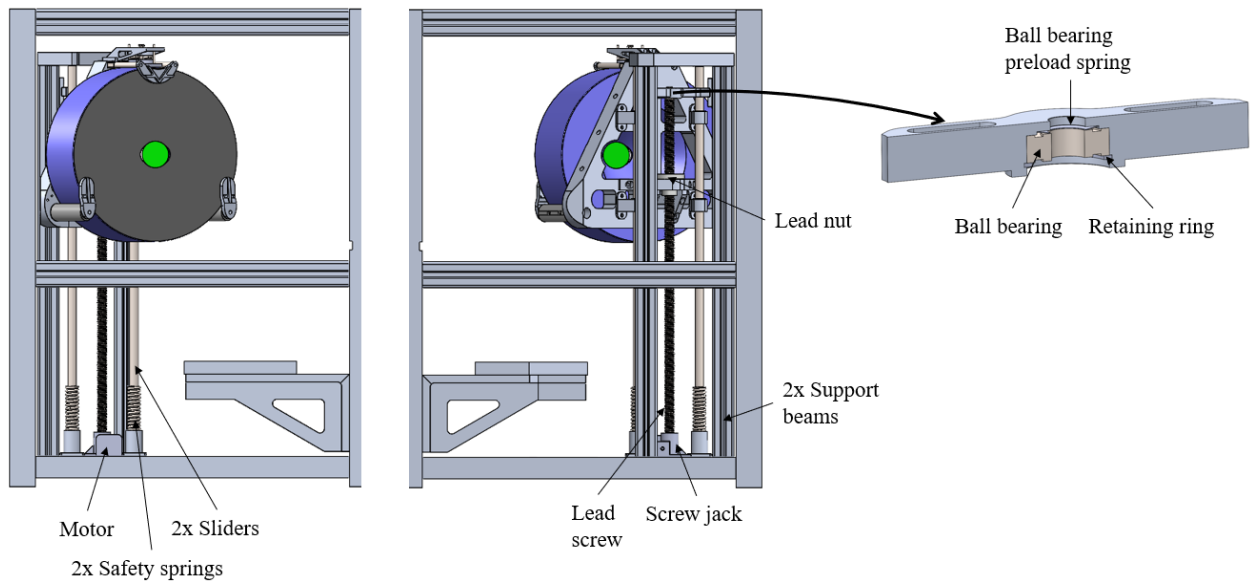


Figure 5.3. Preliminary design of the vertical translation system for M1.

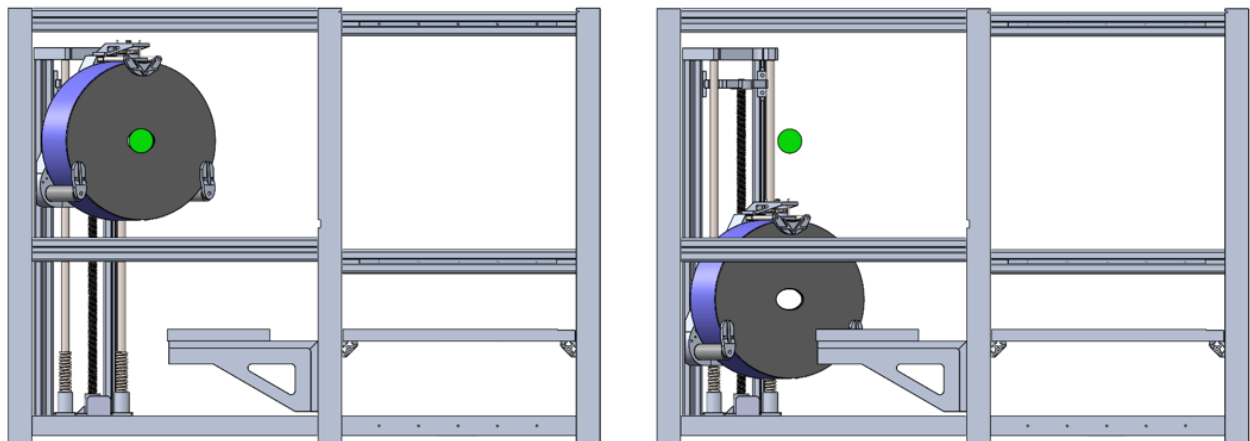


Figure 5.4. M1 position when the SLAO is employed (left) and in its retracted state (right).

The above-presented solution for the retraction of the pickup mirror should be regarded as preliminary; therefore, a more detailed study of the structural behavior of the system is necessary. For instance, the buckling of the lead screw for the given axial load has to be prevented and the load capacity of the sliders and the support beams has to be sufficient to withstand the expected inertia loads. In addition, for the selection of the travel speed the critical speed of the lead screw needs to be taken into account, i.e. the maximum rotational speed beyond which damage can occur to the lead screw and nut due to high-amplitude vibrations. Two additional factors affecting the travel speed is the gear ratio of the screw jack as well as the motor speed. Lastly, the behavior of the lead screw to back-driving needs to be optimized and a fail-safe braking system should be included, so as to increase safety.

5.2.2 L1 mount

The design of the L1 mount is a variation of concept (c) in *Figure 4.12*. The L1 is inserted into an aluminum cell between two spacers, which provide the contact interfaces. Since the L1 is a biconvex lens, tangential contact interfaces have been selected on both sides of the component. The diameter of the cell is slightly larger than that of the lens, so that clearance between the two is maintained over the entire survival temperature range.

The mechanical parts providing the tangential interfaces are made of PEEK GF30^[67], which as a structural plastic provides the necessary stiffness and stability. It should be noted that instead of using the front spacer, the inner contacting surface of the cell, oriented perpendicular to the optical axis, could be machined appropriately in order to provide the tangential interface. In that case this surface would need to be lapped, or, alternatively, the use of a foil (e.g. Kapton) would be necessary to avoid stress concentration at the asperities located on the contacting surfaces. The advantage of this option is that fewer components would contribute to the tolerance chain. Nonetheless, it has been considered a better option to keep the shape of the cell as simple as possible and use a front spacer, because in case of a manufacturing error or damage the latter could be replaced more easily than the entire cell. In addition, the use of the front spacer results in lower contact stresses due to the lower Young's modulus of the plastic (compared to that of aluminum). The omission of the rear spacer, however, is not advisable, because it provides an even distribution of the preload on the optical surface.

The application of the required axial preload is achieved with the use of a wave spring. More precisely, the aluminum back ring presses the wave spring against the rear spacer through which the lens is held in position. The necessary axial preload to prevent radial shift can be calculated based on *eq. (4.7)*. It is often desirable that the preload is adjustable; therefore, in this design concept the magnitude of the preload can be altered with the use of stainless-steel shims of different thicknesses, located between the back ring and the lens cell. Lastly, the L1 assembly, whose total mass is approximately 6.9 kg, is mounted to the middle block of the support structure at three locations.

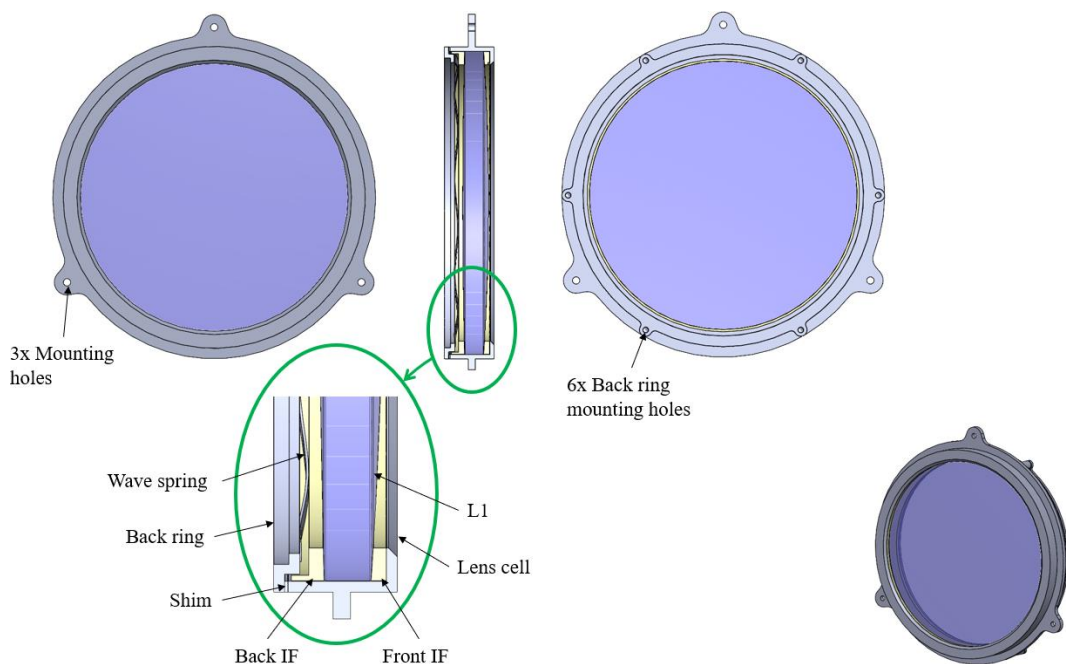


Figure 5.5. Preliminary design of the L1 mount.

5.2.3 M2 mount

The design of the M2 mount is similar to that of the M1 in that it is based on the V-mount concept. The M2 mount consists of three arms, with the lower two carrying two posts on which the M2 rests, as illustrated in the figure below. Much like the posts used to carry the M1, these posts have a metallic core and an outer layer providing low friction. A spring clip at the top of the M2 provides the nesting force in the radial direction. For better performance (i.e. lower friction coefficient and preload distribution along the line of contact) it is advisable that Kapton tape is used between the spring clip and the mirror.

In the axial direction, the preload is applied by three compression springs, each of which carries a mechanical interface at its free end. On the upper surfaces of these interfaces, contact with the rear side of the M2 is established and the mirror is pressed against three hard stops. The magnitude of the axial preload can be adjusted with washers of different thicknesses. Again, the use of Kapton tape at the contact interfaces is advisable for the same reason mentioned earlier. Based on the design of the support structure, the M2 is mounted on the right block (*Figure 5.1*). In *Figure 5.6* the preliminary design of the mounting interface between the M2 and the right block of the support structure is depicted. The mass of the overall assembly, including the M2 mounting interface, is approximately 20 kg.

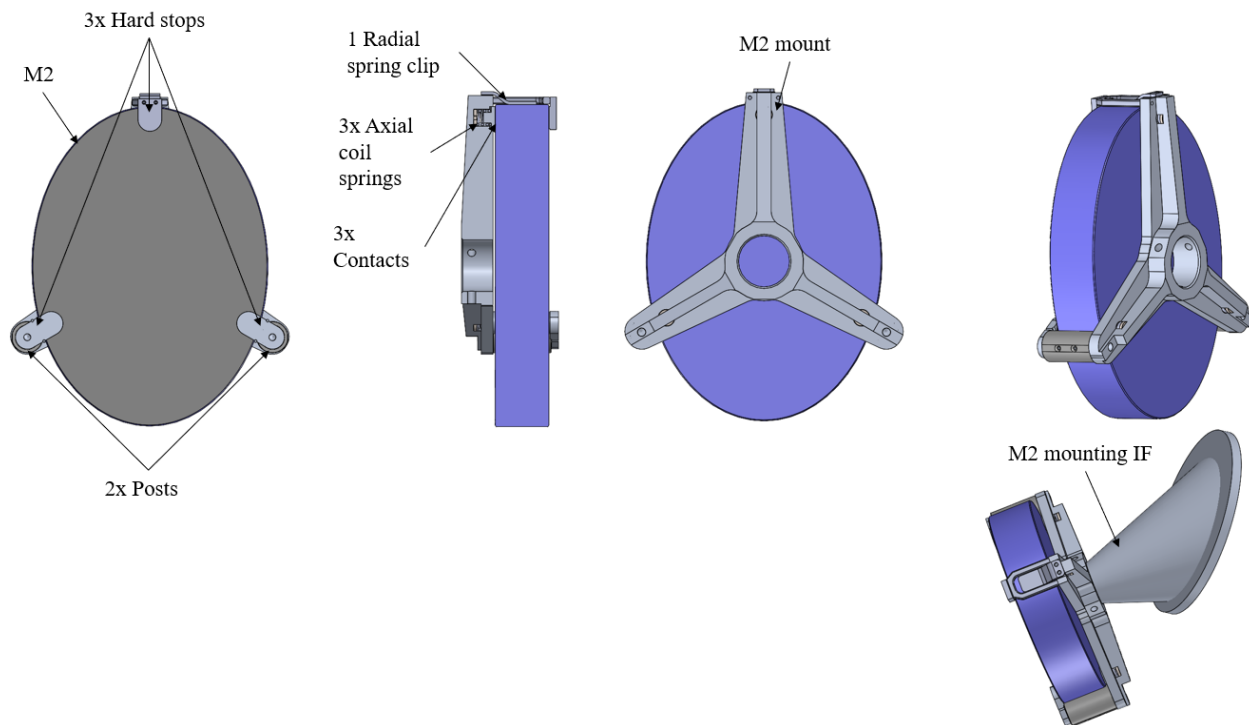


Figure 5.6. Preliminary design of the M2 mount.

Generally, spring clips are used for the application of low-magnitude preloads. Given the mass of the M2 (*Table 4.4*), a better solution needs to be found for the application of the required preload, which is calculated in Chapter 6. Besides that, the size of the hard stops should be reconsidered based on the footprint of the laser beam on the mirror, so that optimal use of the optical surface is ensured. Moreover, the structural behavior of the M2 assembly requires optimization. It is worth noting, however, that the mechanical design of the interface between the right block and M2 is particularly challenging, since the latter is rotated in space (i.e. about all three axes). For that reason, information about the exact position and orientation of the M2 has to be provided by the optical designer after the update of the optical design before embarking on any changes in the mechanical design.

5.2.4 M3 mount

Similar to the design of the mounts for the M1 and M2, the design of the M3 mount is also based on the V-mount concept. The two lower posts, which are of the same design as those for the M1 and M2, are connected to the corresponding arms of the M3 mount and provide the vertical support for the optical component, as presented in the following figure. Again, the nesting force is provided by a spring clip.

The axial preload, which is adjustable (with the use of washers), is exerted on the M3 through three compression springs and the provided contact surfaces. The three hard stops, against which the M3 is pressed, provide the reference for the optical surface. Lastly, the M3 is located below the M2 and is also carried by the right block of the support structure. In the figure below, the mounting interface of the M3 assembly is depicted. The mass of the M3 assembly, including its mounting interface, is approximately 10 kg.

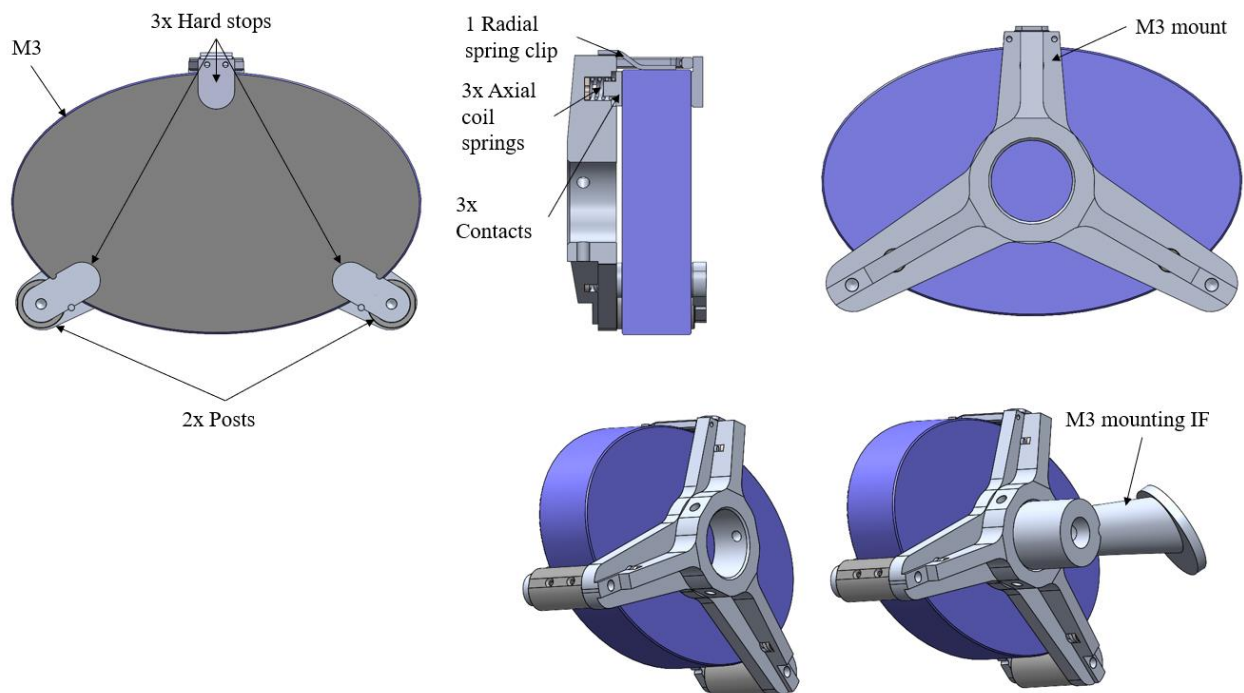


Figure 5.7. Preliminary design of the M3 mount.

Given the great similarity between the M2 and M3 mounts, the same recommendations hold for the improvement of their mechanical design. Besides that, it should be noted that the M3 mounting interface is partly within the envelope of the LISA camera. Collision between the two can be prevented if the height of the overall SLAO system is increased, so that the relative distance between the M3 and the camera becomes longer. Considering the SLAO envelope alone, this change would be possible, since the current design of the support structure does not make use of the entire allocated volume in the vertical direction.

5.2.5 L2 mount

As it can be observed from *Figure 5.8*, the design of the L2 mount resembles that of the L1 mount. More precisely, the lens is held in position between two spacers inside an aluminum cell. In this case, however, the lens is a positive meniscus; thus, the front interface is tangential and the back is toroidal. Again, the inner diameter of the cell is slightly oversized to accommodate the differential thermal contraction (which is the worst case) of the components in the radial direction.

The required axial preload is applied by a wave spring with a circular cross section. Although this wave spring type has a relatively high stiffness (i.e. the preload changes significantly for small spring deflections) it is more compact than that with a rectangular cross section. Moreover, a stainless-steel shim is located between the aluminum back ring and the lens cell, so that the magnitude of the axial preload can be altered if necessary. The L2 assembly is mounted to the middle block of the support structure at three locations, as indicated in the figure below, and has a total mass of approximately 1 kg.

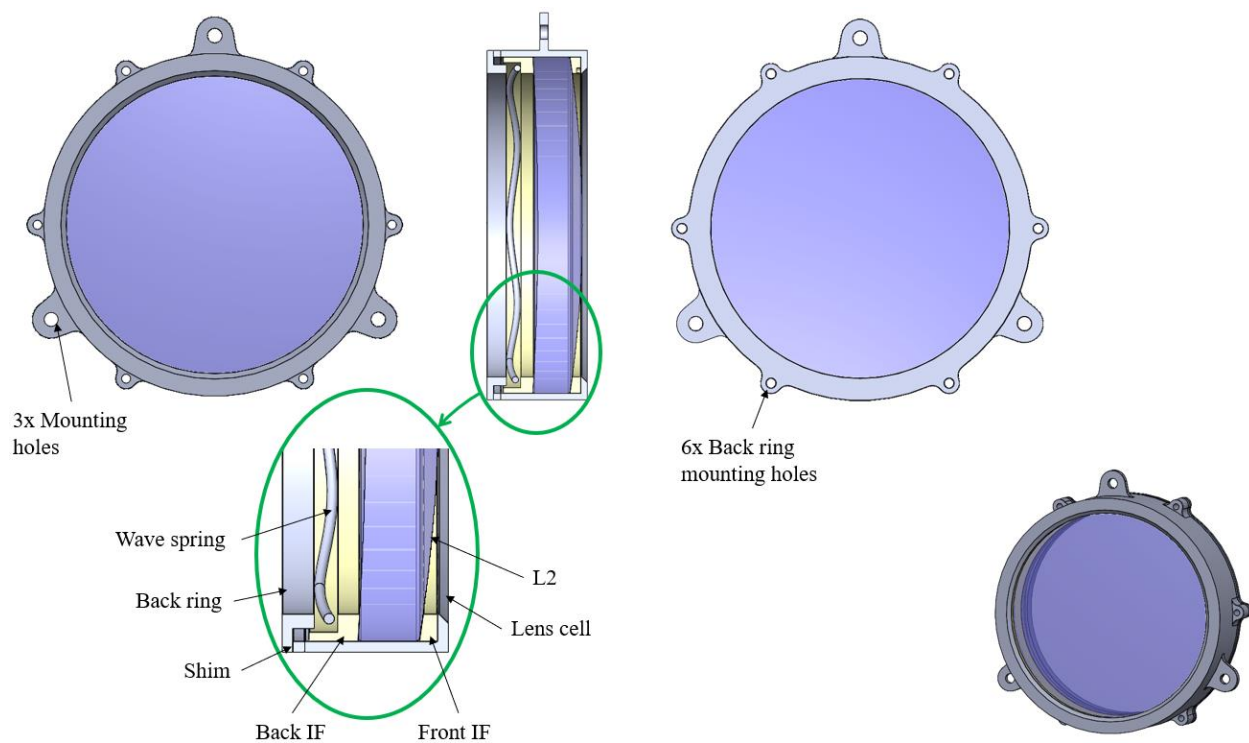


Figure 5.8. Preliminary design of the L2 mount.

5.2.6 M4 mount

The design of the M4 mount is based on concept (b) in *Figure 4.11*. The mirror is inserted into the recess of the aluminum mount with its rear side resting on an elastomeric O-ring, as presented in the following figure. Then, a Kapton foil is placed on the reflecting surface in order to protect it from scratches and to prevent the occurrence of any point contacts (which lead to localized stress concentrations), and subsequently, the aluminum retainer is connected. Two mounting holes are used for the mounting of the M4 assembly on the corresponding mounting plate of the support structure (*Figure 5.1*).

The compressed O-ring presses the M4 against the retainer, which provides the reference for the optical surface. For that reason, any manufacturing inaccuracies on the rear side of the mirror and/or the recess where the O-ring is placed as well as any thickness variations due to temperature changes can be accommodated by the compliance provided by the O-ring. It should be noted that the Kapton foil will be compressed, too; thus, its thickness will change slightly. However, given the small mass of the component and due to the fact that a shift in the lateral direction has no impact on its optical performance (because the mirror is flat), the magnitude of the required axial preload is relatively low. As a result, the change in the thickness of the Kapton foil can be considered negligible. Furthermore, the radial clearance between the M4 and its mount is selected such that temperature variations do not lead to the development of radial stresses in the component. The M4 assembly has a total mass of approximately 0.4 kg.

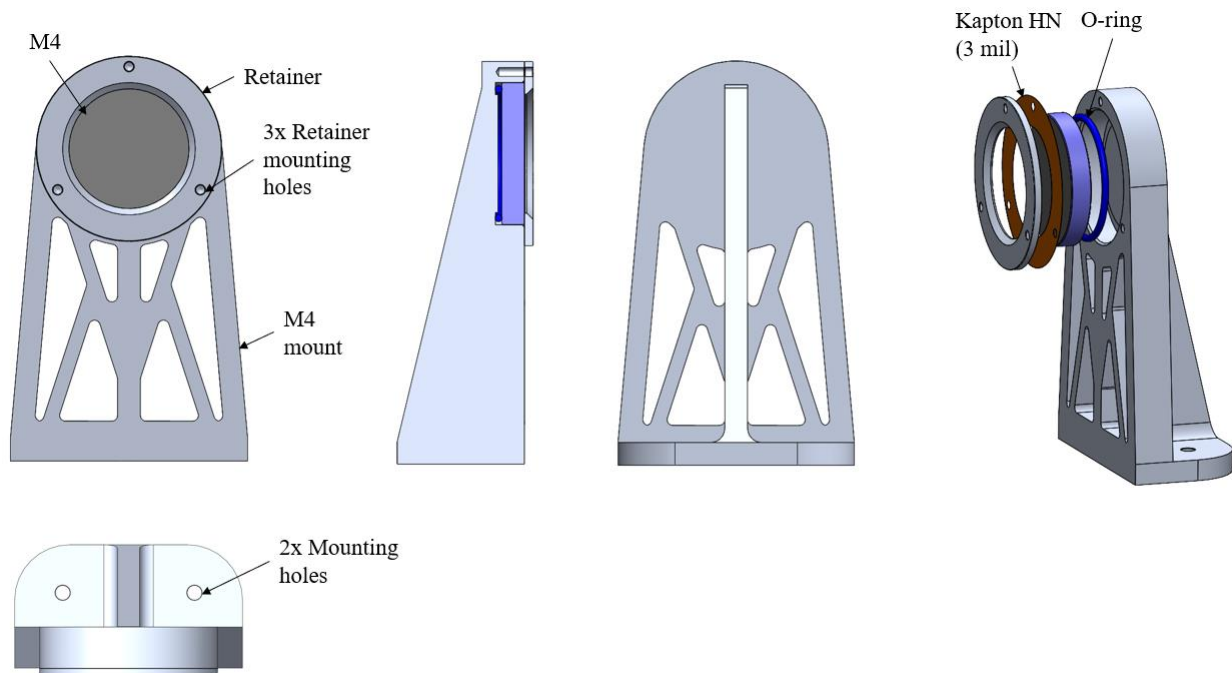


Figure 5.9. Preliminary design of the M4 mount.

Generally, metals are preferred to elastomers when accurate constraining of components is required for a number of reasons. Firstly, the mechanical characteristics (especially the stiffness) of a metallic spring can be determined without significant error; thus, the applied preload is well-defined. However, this is not the case for elastomers, for which a range of preload magnitudes is given for a specific percent compression. Secondly, elastomers suffer from compression set, i.e. a small plastic deformation, which occurs after the application of a load and at a certain temperature. Consequently, compression set, whose magnitude depends on the compound (for a given load) results in a slight preload loss over time. Thirdly, aging can have an impact on the stiffness of the elastomer, leading to a change in the applied preload in

the long run. In addition, elastomers have relatively high CTEs; as a result, temperature changes might affect the magnitude of the preload.

Nonetheless, the use of an O-ring renders the design more compact in cases where the preload is so low that a connection of multiple metallic springs in series is necessary, as this would require a lot of space. For instance, an alternative to the O-ring used for the application of the axial preload in the case of the M4 would be a multiple-turn wave spring, whose turns are connected in a crest-to-crest configuration. Such a spring becomes excessively long; therefore, the envelope and mass of the assembly would increase.

Yet another solution for the application of the preload in the case of the M4 would be the use of three soft pads, which can be cut from an elastomeric sheet. These pads would press the rear side of the component against three references; thus, a well-defined reference plane would be used for the mounting of the mirror. Finally, as a next step for the improvement of the mechanical design of the M4 mount, a detailed study of its structural behavior under the given load cases (*Table 3.1*) is necessary.

5.2.7 M5 mount

From the following figure it can be observed that the design of the M5 mount resembles that of the M4 mount very closely. The only difference is the larger size, and thus the higher mass, of the M5. However, this deviation has an impact only on the size and type of the O-ring used, so that the mirror is held properly in position (i.e. according to the principle presented in *Figure 4.10*) and with the required axial preload. The M5 assembly, whose total mass is equal to 0.5 kg, is mounted on the same plate as the M4 at two locations, as indicated in *Figure 5.10*. Lastly, regarding the improvement of the mechanical design, the recommendations made in the case of the M4 hold for the M5 as well.

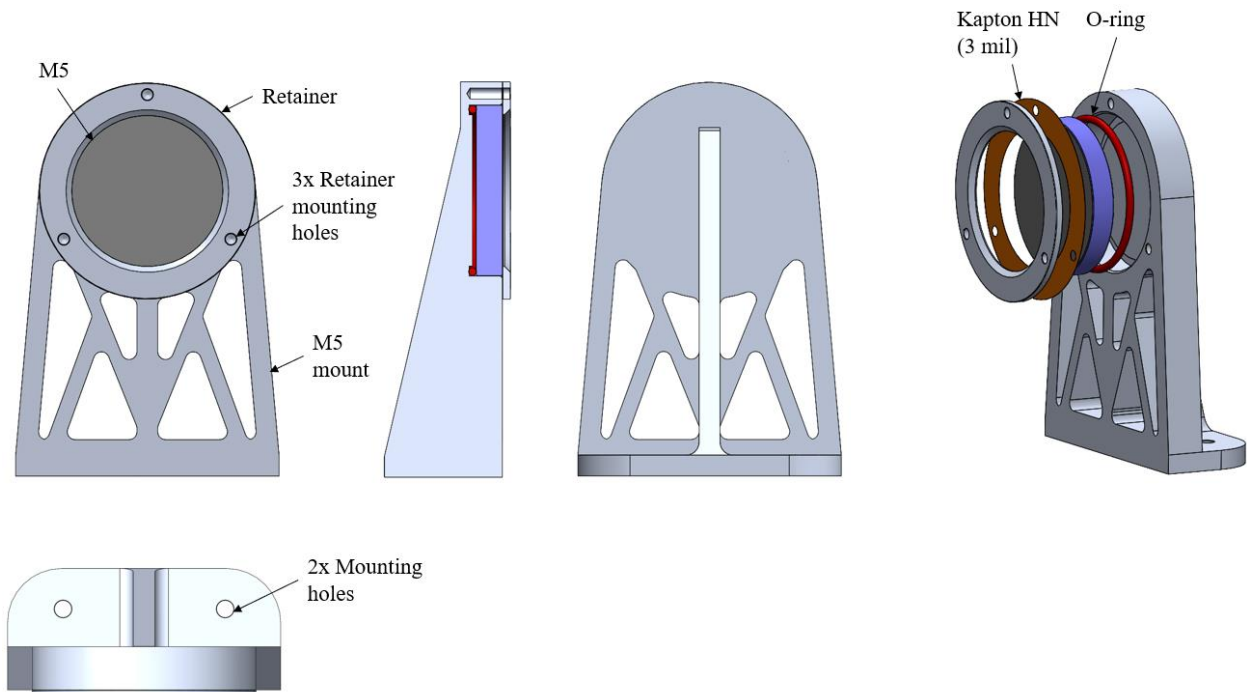


Figure 5.10. Preliminary design of the M5 mount.

5.2.8 L3-L4 mount

The lenses L3 and L4 can be mounted together in a single tube (or barrel), given the short distance between them. Moreover, since they are of the same size, the concept presented in view (a) of Figure 4.14 would be suitable for the design of the tube. As illustrated in the following figure, both lenses have the shape of a negative meniscus; thus, both toroidal and tangential contact interfaces are used. More precisely, the rear surface of the front spacer provides a toroidal interface, the front and back surfaces of the middle spacer offer a tangential and toroidal interface, respectively, and the front surface of the last spacer contacts the rear optical surface of L4 tangentially. All the above components are inserted into the aluminum tube and are held in position with the use of a wave spring with a circular cross section and the back ring. A stainless-steel shim is mounted between the lens tube and the back ring, in case the axial preload needs to be adjusted.

In the radial direction, the magnitude of the clearance between the inner surface of the barrel and the rims of the lenses ensures that the latter will not be squeezed by the tube as the temperature drops. It should be noted that in the case of a multielement mounting the relative distance between the centers of the optical components is important. A large radial clearance might require lateral alignment of the lenses inside the tube, depending on the decenter tolerance defined by the optical design. For this particular optomechanical design the maximum decenter between the two lenses is 0.15 mm. However, given that both lenses are highly curved, based on eq. (4.2) through (4.6), self-centering occurs for relatively low axial preloads. The calculated magnitude of the minimum axial preload can be found in Chapter 6. Besides the mounting of the two lenses, the L3-L4 mount provides three mounting holes for the fixing of the assembly on the corresponding mounting plate of the support structure. Lastly, the total mass of the L3-L4 assembly is equal to 1.5 kg.

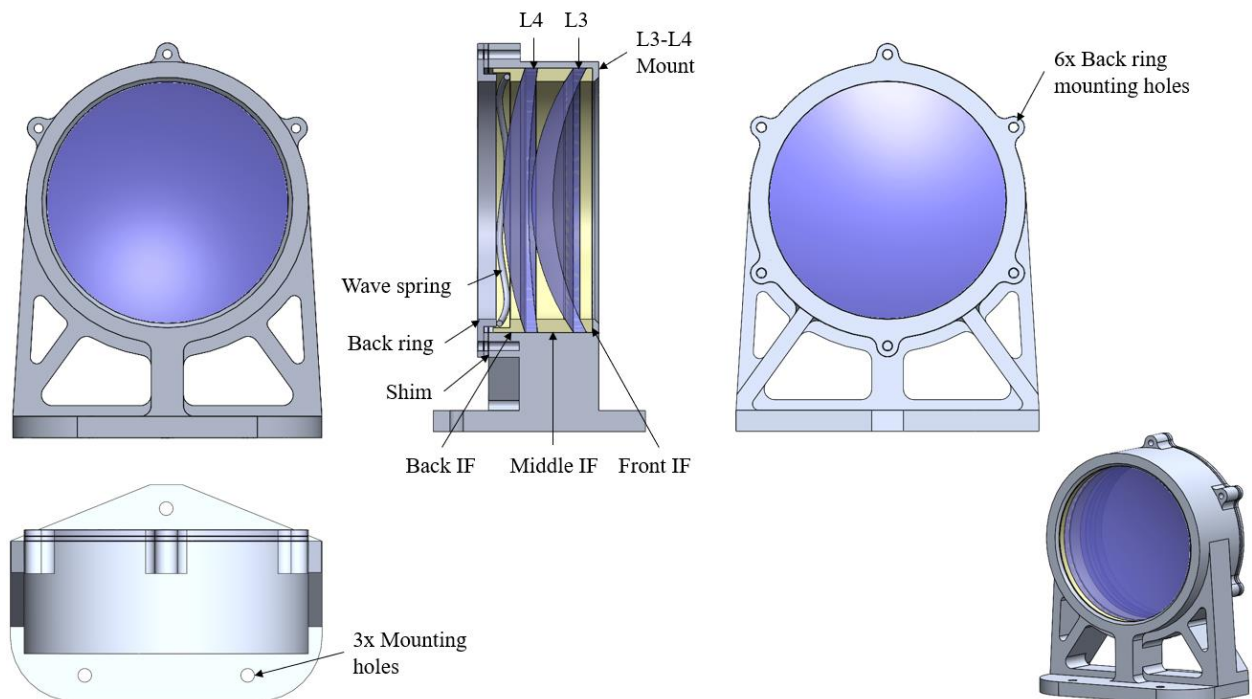


Figure 5.11. Preliminary design of the L3-L4 mount.

5.2.9 L5-L6 mount

Similar to L3 and L4, the relatively short distance between lenses L5 and L6 allows for a single-cell mounting of the two components. As it can be observed from the following figure, the L5-L6 mount resembles that for the L3 and L4 in that the components are inserted in an aluminum tube and the appropriate interfaces and lens distance are provided by spacers. More specifically, L5 is a biconvex lens and L6 is a positive meniscus; thus, all but the last contacting interfaces are tangential. However, unlike the L3-L4 assembly, in this case the axial preload is applied differently, i.e. with the use of a custom-made spring. The reason for this choice is that for the given lens diameters a suitable, commercially available spring could not be found.

On the rear side of L6 Kapton foil is placed and on top of it the stainless-steel shim and subsequently the flange with the cantilevered springs are stacked. Then, the backup ring is added and the components are fixed together. The Kapton foil is used in order to prevent high stress concentrations and to avoid the sharp edges of the metallic spring from scratching the optical surface of the lens. The spring consists of forty identical cantilever beams, which distribute the axial preload equally over the corresponding contacting arcs on the optical surface. As explained in subsection 4.2.4, the backup ring prevents excessive bending of the spring close to the fixed end (where the bending moment approaches its highest value) and also stiffens the rim of the spring. The inner diameter of the tube is 0.1 mm larger than the outer diameters of the lenses; thus, a maximum decenter of 0.1 mm can occur between the two optical components. The L5-L6 assembly, whose mass is approximately 0.9 kg, is mounted on the corresponding mounting plate of the support structure at three points.

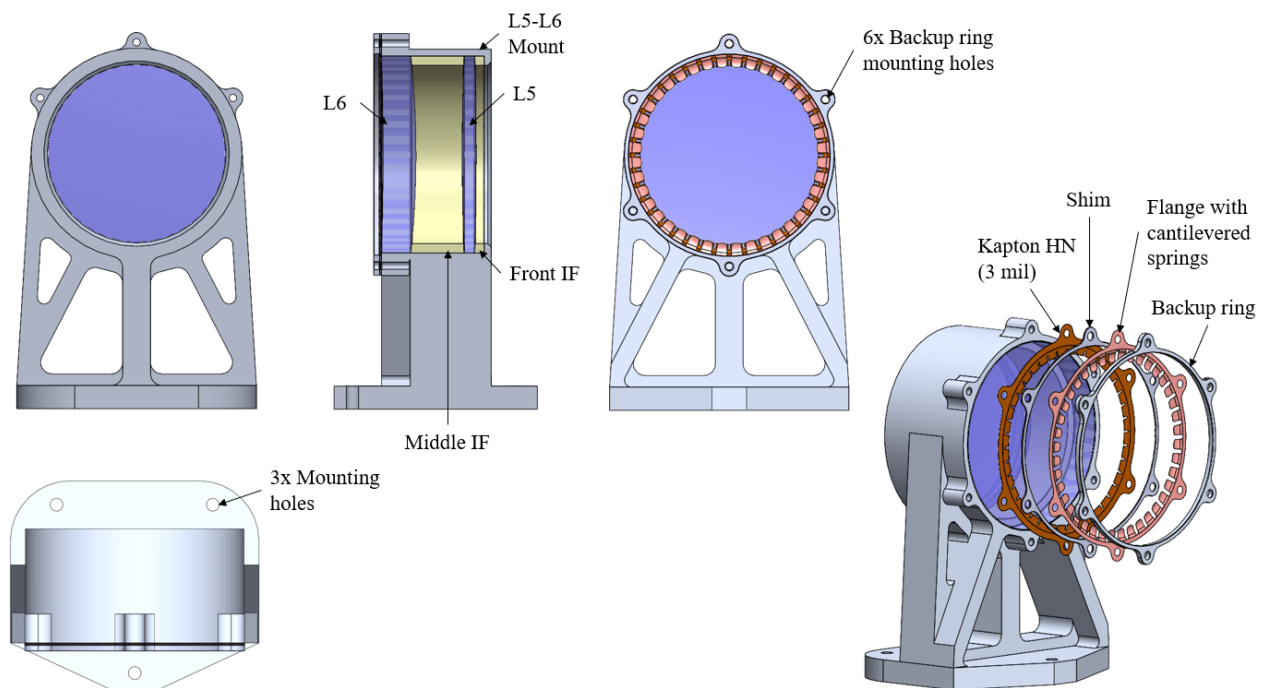


Figure 5.12. Preliminary design of the L5-L6 mount.

It should be noted that instead of a custom-made spring an O-ring could be used for the application of the preload, which, however, would not be well-defined, and neither would variations of its magnitude be easily predicted for changing ambient conditions. Although this uncertainty is not critical for mirrors, the optical performance of lenses might be degraded due to stress birefringence. This problem could be mitigated with the use of softer O-rings (i.e. shore A hardness from 50 to 70, depending on the required preload and the selected percent compression).

5.2.10 M6-M9 mount

The components M6 and M9 are located very close to each other and at an angular distance of 90° . This angle is important because it defines how accurately the laser beam is directed to the WFS through the moving M7-M8 group. Ideally, M6 and M9 would be mounted to a common mount without any intermediate cells, so that the total position error due to manufacturing tolerances remains as small as possible. However, given the geometry and the space limitations this is quite difficult. For that reason, the components are first mounted into their own cells and then to a common mount. The design of every mount is described below.

The following figure depicts the M6, mounted in its aluminum cell. The optical surface of the component is pressed against three hard stops, provided by the cell, by means of three cantilevered spring clips. Kapton tape is used between the front side of the mirror and the hard stops, while Kapton foil is placed between the rear side of the M6 and the spring clips. In addition, shims are used between the cell and the spring clips, in case the applied axial preload needs to be adjusted. Every spring clip is mounted at two points to avoid excessive rotation and thus deviation from the theoretical location where the preload should be applied. A backup plate is used on the top side of every spring clip, for reasons explained in previous sections. Lastly, the cell provides three mounting holes for its mounting to the common interface (*Figure 5.15*).

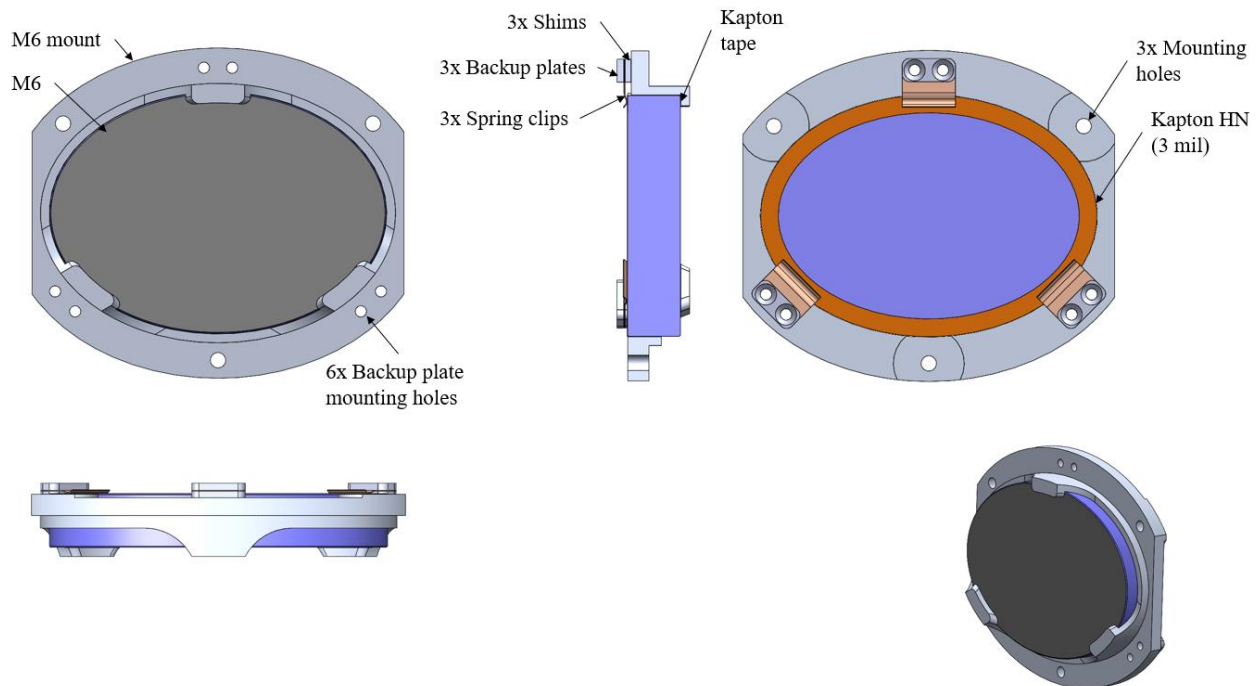


Figure 5.13. Preliminary design of the M6 mount.

As presented in the following figure, the M9 assembly consists of the aluminum cell, the mirror, the Kapton foil, the O-ring for the application of the preload and the shim for the adjustment of the preload magnitude; i.e. no other part is included for the compression of the O-ring. For the constraining of the M9 the common mount is used, instead. More specifically, the integration sequence for the mounting of M9 requires first the O-ring to be placed inside the recess provided by the common mount. Subsequently, the shim is added, the mirror is placed on top of the O-ring, then the Kapton foil and lastly the M9 cell. If tilting of M9 is necessary, the single shim can be replaced with individual washers.

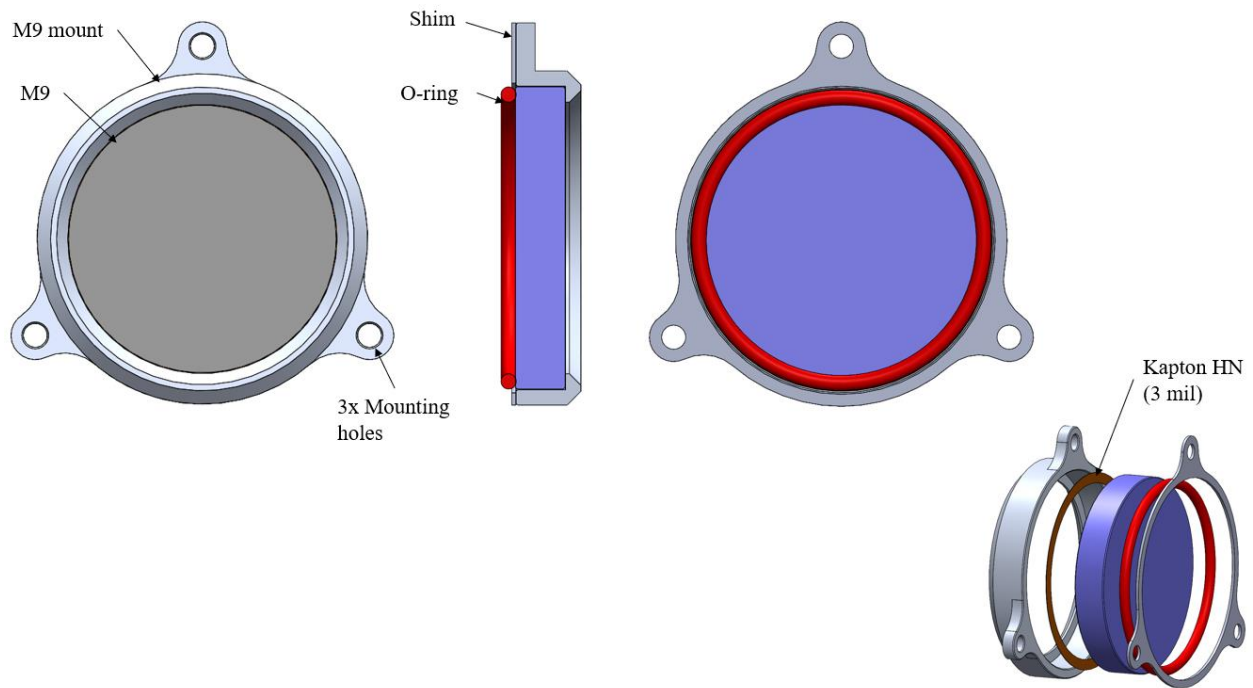


Figure 5.14. Preliminary design of the M9 mount.

The common mount of the M6-M9 group (Figure 5.15) provides the 90° angular separation between the two components, so that their position is relatively accurate and a priori verifiable. In that way, during the optical alignment in the SLAO system the two components can maintain their relative positions. This part, which is made of aluminum, also provides the interface (i.e. three holes) for the mounting of the assembly on the corresponding mounting plate of the support structure. The overall mass of the M6-M9 assembly is approximately 1 kg.

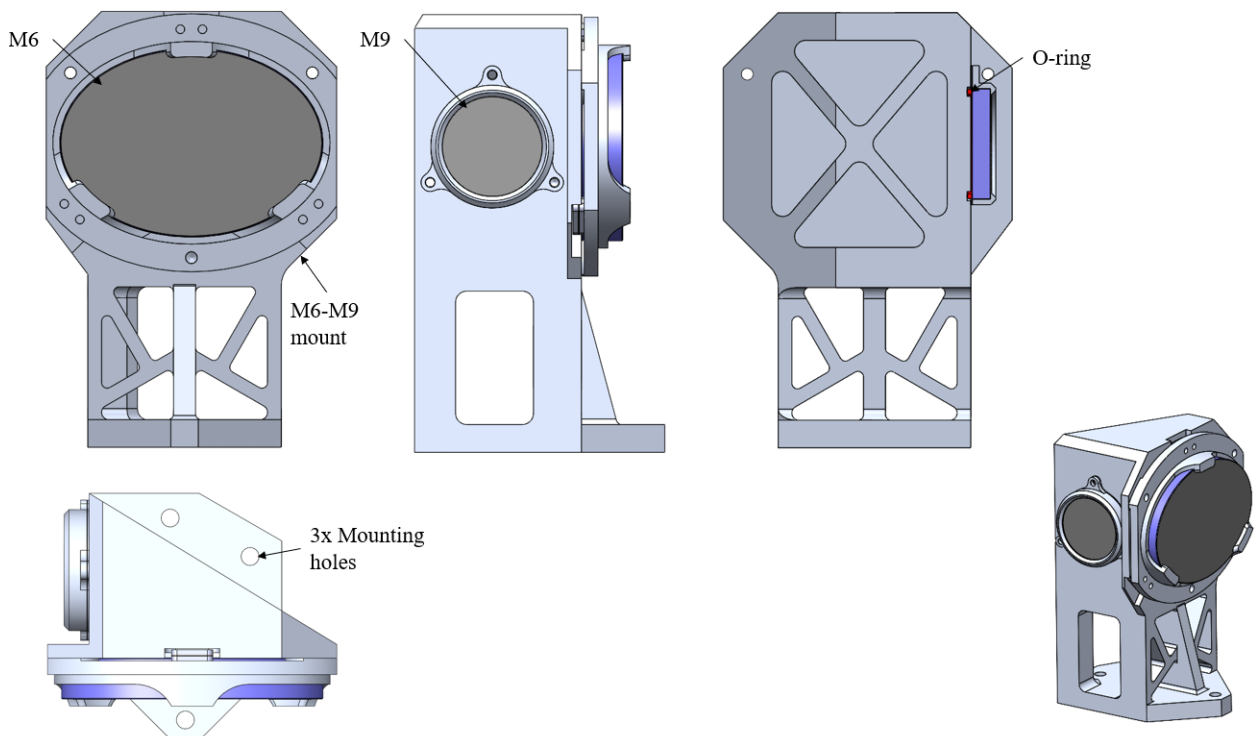


Figure 5.15. Preliminary design of the M6-M9 mount.

5.2.11 M7-M8 subsystem

Similar to the M6-M9 mirror group, the M7 and M8 have an angular separation of 90° . However, in this case the geometry allows for a direct mounting to a common mount, as illustrated in the following figure. The design of the M7-M8 mount is based on the concept presented in view (a) of *Figure 4.11*, with the only difference that the preload is not applied with the use of spring clips. More specifically, the mount provides a reference plane through a step, on which the reflecting surfaces are located. Kapton foil is used between the two surfaces (*Figure 5.17*) for reasons explained earlier. The two components are inserted into the corresponding recesses in the aluminum mount and are preloaded with the use of O-rings, which are compressed by the retainers. Again, shims are included in case the preloads need adjustment. Moreover, the M7-M8 mount provides a mounting interface, consisting of four holes.

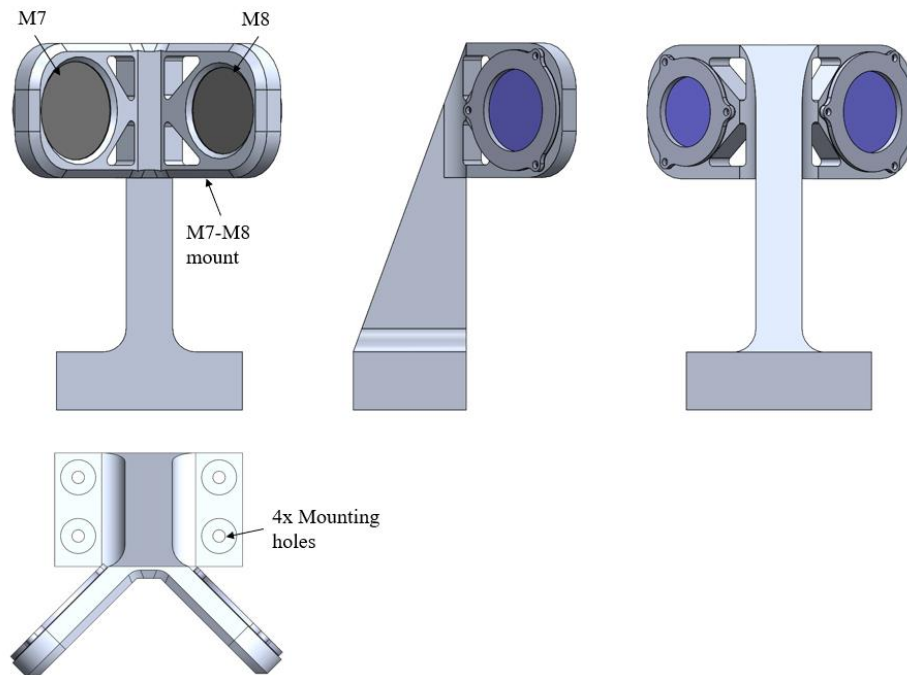


Figure 5.16. Preliminary design of the M7-M8 mount.

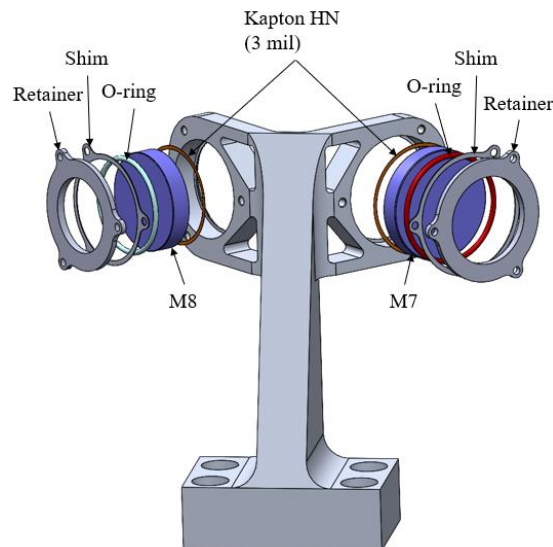


Figure 5.17. Exploded view of the M7-M8 mount.

As explained in the previous chapter, the horizontal translation of the M7-M8 group corrects for the defocus of the laser beam on the WFS, generated by variations in the altitude of the Sodium layer and/or changes in the zenith angle. Therefore, the M7-M8 mount is connected to an intermediate adapter plate (which includes both mounting interfaces) and then, to the translation stage. Due to space limitations, the M7-M8 mount cannot be mounted at the center of the carriage. Theoretically, this is an undesirable situation, because it would generate moments, which, in turn, would lead to a tilt. However, in practice this tilt is considered negligible, given the relatively low mass of the attached load.

The translation stage is attached to two mounting feet, which are used for the connection of the entire assembly to the base plate of the support structure. The total mass of the M7-M8 subsystem is approximately 33 kg. It should be noted that the mass of the customized translation stage is not known; thus, a value of 25 kg is assumed (the mass of the standard, commercially available version is 35 kg). Lastly, a study of the dynamic behavior of the subsystem would be useful, in order to determine if the current mechanical design provides the necessary stiffness for the given inertia loads. Besides that, it should be investigated whether the heat generated by the linear motor of the translation stage is transferred efficiently towards the base plate of the support structure.

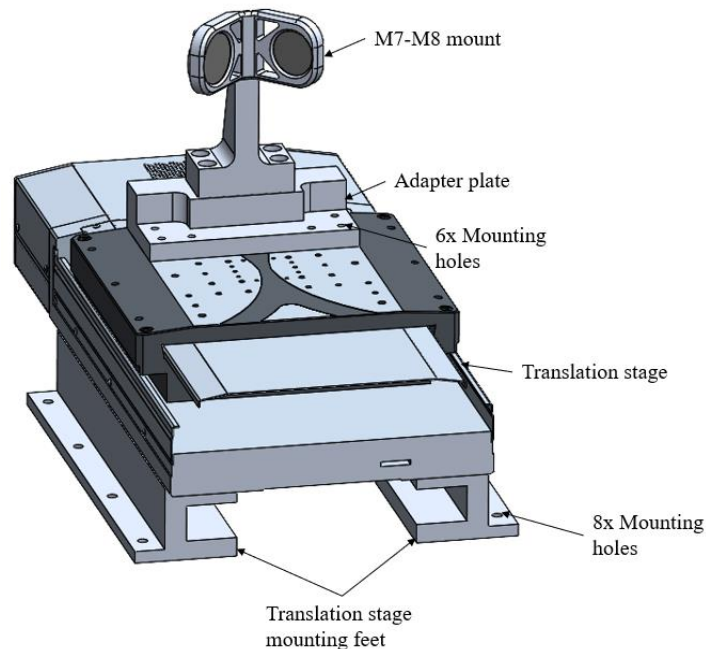


Figure 5.18. M7-M8 mount attached to the selected translation stage.

5.2.12 L7 mount

The design of the L7 mount is based on the concept presented in view (f) of *Figure 4.12*. However, given that this lens is located very close to the M9 and the M8 for a zenith angle equal to 60° , the containment of its entire circumference in a circular cell is impossible, due to potential collisions with its surroundings. Therefore, the mechanical diameter of the lens has been increased in the vertical direction so as to facilitate its mechanical clamping, while in the horizontal direction cutouts have been introduced, resulting in a lens width slightly larger than the clear aperture.

As illustrated in the figure below, the lens, which is a negative meniscus, is inserted into an aluminum cell and, contrary to the designs presented previously, the rear optical surface rests on a tangential surface provided by the cell itself (i.e. no intermediate spacers are used). It should be noted that between the optical surface and the mechanical interface Kapton foil is used. The reason for this design choice is that the magnitude of required axial preload is quite low because the mass of the component is low; thus, the mount-induced contact stresses are expected to be low as well (and with the use of Kapton even lower). In that way the mount can be more compact.

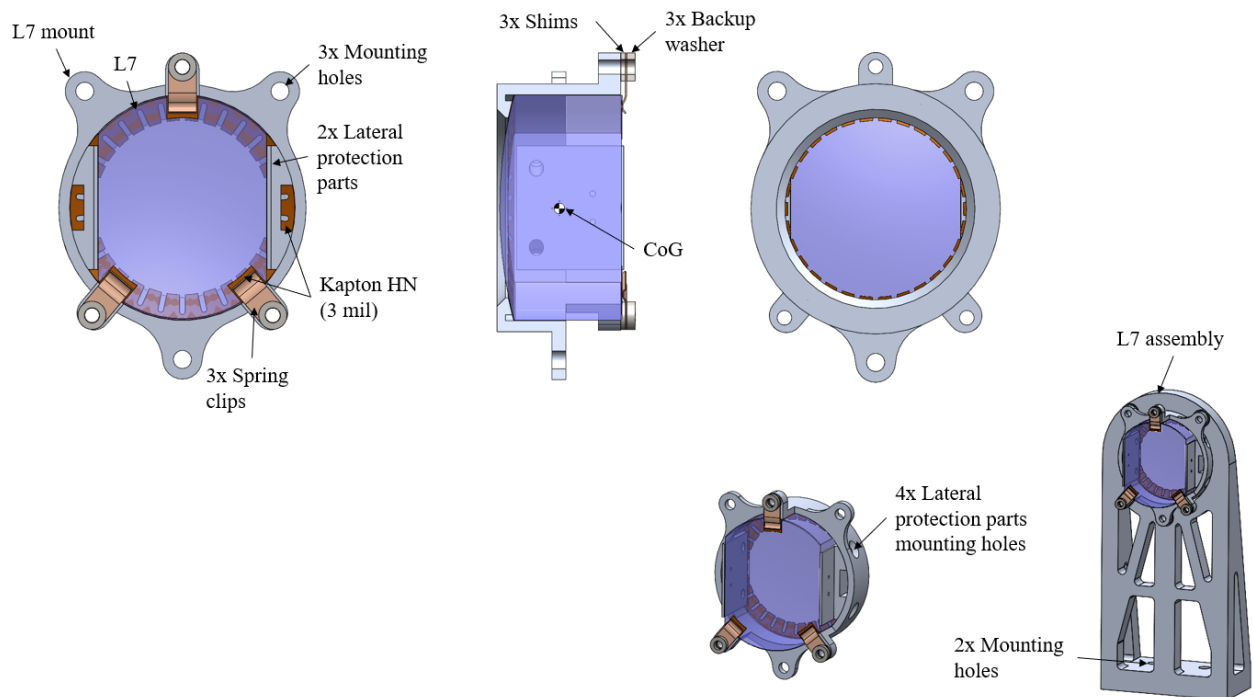


Figure 5.19. Preliminary design of the L7 mount.

The front optical surface, which in previously-presented designs rested on a hard stop, is used here for the application of the (adjustable) preload through three spring clips. The angular separation of the two lower springs is 80° ; a larger angle would result in collision. Furthermore, given the negative curvature of the lens, a toroidal interface is provided by the three springs, between which and the optical surface Kapton foil is used. Because of the close proximity of the L7 to the mounts of M9 and M8, two mechanical parts are added on both sides of the lens in the horizontal direction to offer protection from chipping, in case a collision does occur.

In addition, the radial clearance between the lens and its mount ensures that temperature variations within the given survival range will not generate compression stresses in the glass. Furthermore, the L7 mount provides the mounting interface (i.e. three mounting holes), which is located on a plane passing through the CoG of the lens, so that the generation of moments is avoided. The L7 assembly, including

the mechanical part to which the L7 mount is connected, has a mass of approximately 0.2 kg and is mounted on the corresponding mounting plate at two locations. Lastly, a more detailed analysis of the dynamic behavior of the above assembly is necessary to optimize its mass and stiffness and to ensure that it can withstand the expected inertia loads.

5.2.13 L8-L10 mount

The L8-L9-L10 group is the last assembly of the optics chain. The relatively short distances between these optical components allow for their mounting into a common tube, as depicted below. The lens L8 is a positive meniscus and is highly curved; thus, in order to avoid chipping of its outer edge, a flat bevel is added to its rear surface. For the same reason, flat bevels are introduced to the front and the aspheric rear surface of the L9. Moreover, the last lens, which is the lenslet array, is modelled as a flat plate.

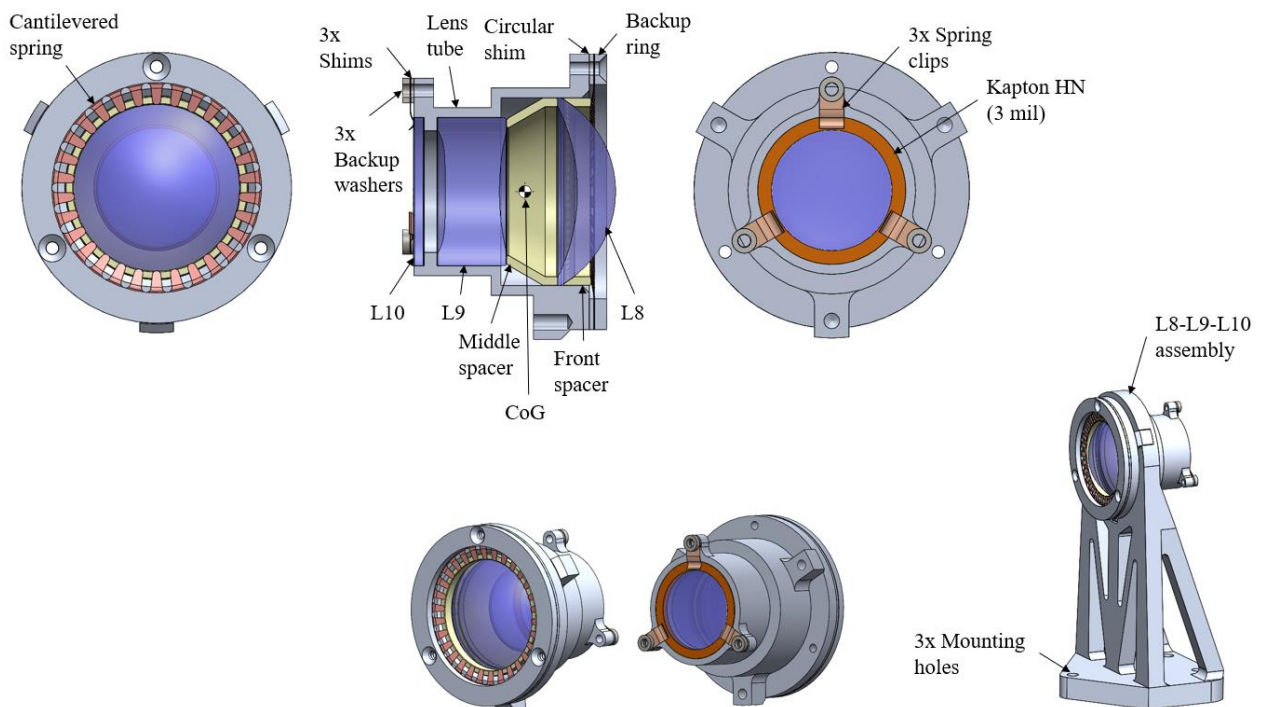


Figure 5.20. Preliminary design of the L8-L9-L10 mount.

Even though L9 and L10 have the same mechanical diameter, their masses differ significantly; by contrast, the masses of L8 and L9 are similar. For that reason, L8 and L9 are mounted together, so that they can share the same axial preload. The design of the aluminum tube is based on the concept presented in view (a) of Figure 4.14 and the difference in diameter between the two components is accommodated by a slope added to the middle spacer.

The preload, which can be adjusted with the aid of a circular shim, is applied with the use of a flange comprising 30 cantilevered springs. These springs press L8 through the front spacer, whose addition was deemed necessary because of the high curvature of L8. Moreover, the spring flange is supported by the backup ring. On both sides of the step between L9 and L10, provided by the tube, Kapton foil is placed (not shown in the figure), so that a degree of compliance is introduced between the flat bevel or face of the corresponding optical components and the metallic surface. On the other side of the tube, L10 is held in position with three spring clips. Although, theoretically, the axial preloads on both sides of the tube could be applied with the use of O-rings, their magnitude is so low that the selection of suitable O-rings

would be quite difficult. Alternatively, the preload magnitudes could be increased, which, however, would introduce unnecessarily high stresses in the optical components.

The tube is attached to its mechanical support at three locations and, similar to the L7 mount, the mounting plane passes through the CoG of the tube after all three optical components have been integrated. The mechanical support provides three mounting holes for the connection of the assembly to the corresponding mounting plate of the support structure. It should be noted that for the given position of the focal plane, part of the L8-L9-L10 assembly is currently inside the envelope of the LISA camera (*Figure 5.22*). Therefore, it should be investigated whether the tube can be attached directly to the camera instead of the mounting plate. Lastly, the stiffness and mass of the L8-L9-L10 assembly, with the latter being approximately 0.4 kg, need to be optimized for the given inertia loads.

As explained earlier, when multielement mounting is performed, it is essential to ensure that the distances between the optical axes of the individual components are as small as possible. In the case of the L8-L9-L10 mount, if no lateral adjustment is performed, then the maximum deviation is 0.1 mm. Finally, it is worth noting that for the design of the tube, the concept presented in view (*b*) of *Figure 4.14* could be applied. However, in that case every component would require an individual mechanical part for the application of the axial preload.

5.3 Integration of components and subsystems into the SLAO system

After having introduced the preliminary mechanical design of the SLAO system, the sequence in which the components and subsystems can be integrated is considered. This sequence depends on the accessibility of the components at different stages of the integration, their dimensions and role in the SLAO system. The numbering in *Figure 5.21* represents the proposed integration sequence.

As soon as the individual components of the support structure are connected together and the translation system of the M1 is integrated, the lenses L1 and L2 are mounted to the middle block, since they do not affect the accessibility of other components and can be connected more easily if there is still enough space around them. Subsequently, the mounting plate, appearing on the right-hand side of the figure, with the optical components already attached to it, is mounted on the two corners which are attached to the middle block. If possible, the components attached to this plate are pre-aligned, so that their relative positions (ideally) do not need to be changed after the mounting of the common plate.

As a next step, the M7-M8 translation stage is mounted on the base plate of the support structure. It should be noted that the M7-M8 mount is not attached to the stage yet. Then, the mounting plate on the left-hand side of the figure is mounted. Again, for the same reason explained above, it is preferable that all components are already attached to the mounting plate and pre-aligned. Then, the integration of the M7-M8 mount follows and after that the M3 and M2 can be mounted on the right block. Lastly, the M1 is inserted into the structure from the top and the LISA camera, which is considered a sensitive system in terms of handling and cleanliness, is mounted.

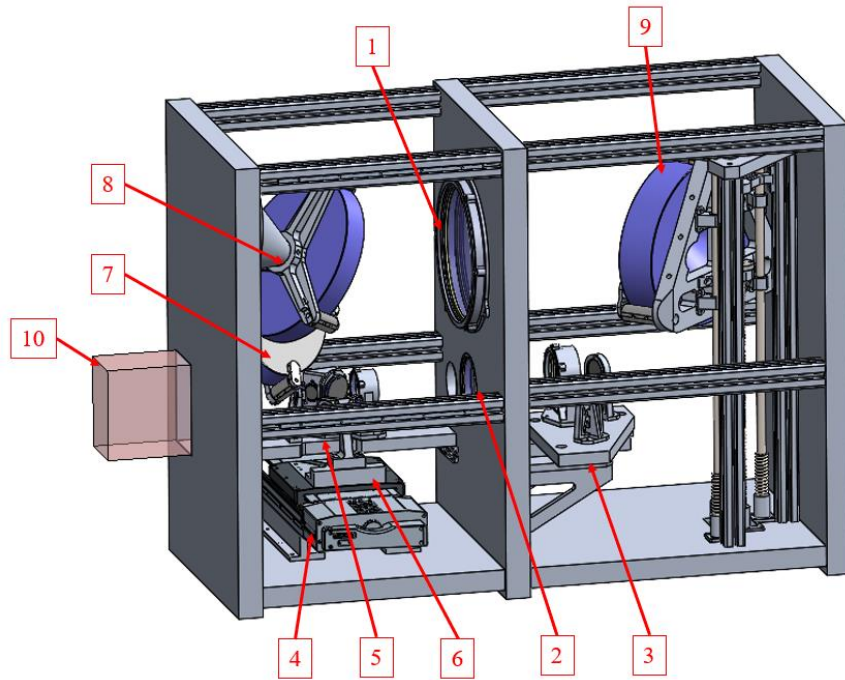


Figure 5.21. Proposed integration sequence of the components and subsystems in the SLAO system.

As mentioned in the discussion of the support structure design, additional stiffeners might be necessary to prevent the relative motion of the blocks. Thus, there may be limitations pertaining to the sides of the support structure from which the components can be inserted into the system. In other words, the detailed design of the support structure should guarantee that the required space is available for the integration of every component.

In the following figure the front, top and a three-dimensional view of the complete SLAO system is illustrated.

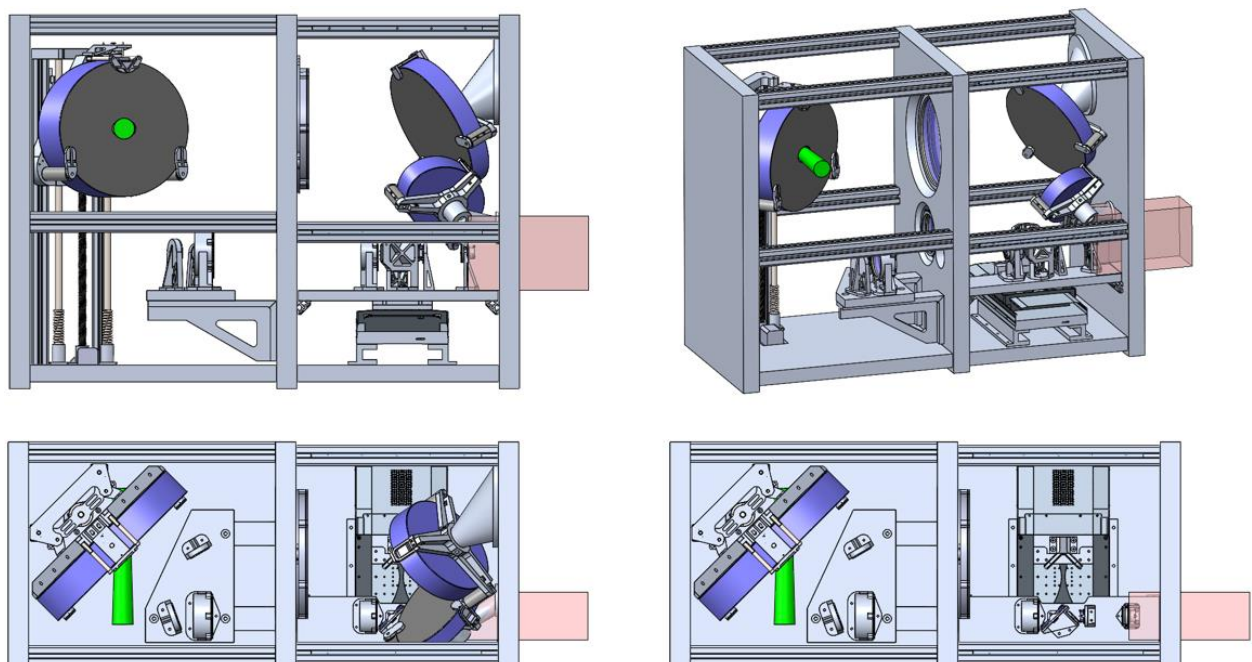


Figure 5.22. Optomechanical design of the SLAO system. In the bottom right figure, the top view of the system is repeated with the M2 and M3 hidden for clarity.

5.4 Cleanliness

Another aspect which needs to be addressed in the (opto)mechanical design of the SLAO system is cleanliness. More specifically, it would be desirable if the optical surfaces could remain clean over longer periods of time, since the presence of dust on the optical surfaces of the system would result in performance degradation. Generally, depending on the operating wavelength range, the way in which dust affects the performance of an optical system differs. In the IR band dust acts as an emitter of thermal radiation, while in the optical band (in which the SLAO system operates), it scatters the incident light, generating stray light. In any case, the presence of dust results in a lower SNR.

In addition, the pixels of the detector that are covered with dust can be considered dead, which also leads to performance loss. Unlike all other optical components (mirrors and lenses) cleaning a contaminated detector without causing permanent damage is not easy. For that reason, sheet metals have been added to cover most of the optical components. These covers compartmentalize the SLAO system in three different sections; the first section, which contains only the M1 and its translation stage, remains uncovered, the covered second section includes the M4, M5, L3 and L4, and the third section the rest of the system, i.e. the entire part between the middle and right block, as presented in the following figure. The total mass of the covers used is approximately 20.3 kg. It is worth noting that the covers can be removed without requiring the dismounting of any of the optical components in the system.

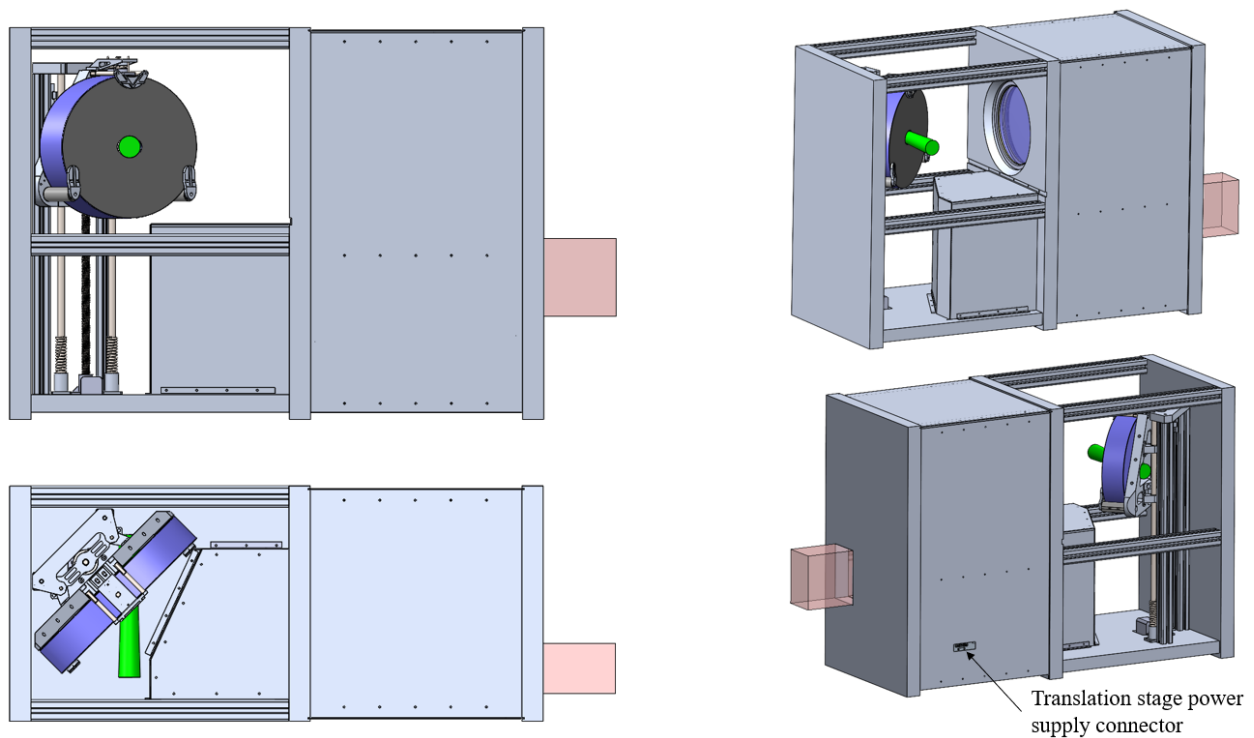


Figure 5.23. Cleanliness of the SLAO system.

The covering of the system may have an impact on its thermal behavior, since the abduction of the internally generated heat might be hampered. Thus, a thermal analysis should be conducted in order to guarantee that the performance of the SLAO system will not be degraded and, if possible, to propose measures (e.g. coatings, partial removal of sheets) which could improve the heat transfer away from the unit.

6 Results and Recommendations

This chapter focuses on the calculation of the required preloads for the holding of all optical components in the SLAO system. In addition, the change in the preload magnitudes due to temperature variations for every subassembly is studied and the optomechanical tolerance budget is analyzed. Subsequently, a brief discussion of the mass and cost estimates of the entire system is presented and the verification of the predefined requirements is investigated. Lastly, the future steps involved in the design of the SLAO system are identified at end of the chapter.

6.1 Calculation of minimum axial preloads

In the following table, the minimum axial preloads required for the mechanical clamping of all mirrors are presented. Since all mirrors are flat, a lateral shift would not affect their optical performance. Therefore, these preloads are calculated based on *eq. (4.1)*.

Component	Acceleration [m/s ²]	Mass [kg]	Safety factor [-]	Min. axial preload [N]
M1	34.335	33.459	2	2,297.621
M2	34.335	16.411	2	1,126.969
M3	34.335	8.011	2	550.091
M4	34.335	0.040	2	2.726
M5	34.335	0.084	2	5.761
M6	34.335	0.192	2	13.216
M7	34.335	0.032	2	2.208
M8	34.335	0.025	2	1.746
M9	34.335	0.021	2	1.418

Table 6.1. Minimum axial preloads for the clamping of the mirrors.

By contrast, the decenter of a lens can influence the resulting image quality; thus, lateral movement should be avoided. For that reason, *eq. (4.2)* is used for the calculation of the minimum axial preloads for all lenses in the system. For this calculation both the clamping angle and the coefficient of static friction are taken into account. Generally, it is quite difficult to find information pertaining to the value of the friction coefficient, especially for combinations of materials with specific surface properties. For the calculations of the minimum axial preloads in *Table 6.2* the coefficient of static friction for PEEK GF30 was assumed equal to 0.35, based on the measurements presented in the publication by Doumeng^[68]. Moreover, for some lenses Kapton is used. In the datasheet^[69] of this material the value of 0.6 is provided, but it only refers to a film-to-film contact, which is not representative of the present case. Therefore, for all calculations the value of 0.35 is used, which can be considered worst case when Kapton is used. Lastly, in the table below, the safety factor for the first two cases is 1.5, because a value higher than that would lead to very high preload magnitudes for the given clamping angles.

Component	Acceleration [m/s ²]	Mass [kg]	Safety factor [-]	Clamping angle [°]	Min. axial preload [N]
L1	34.335	5.992	1.5	5.150	874.675
L2	34.335	0.898	1.5	11.182	127.191
L3	34.335	0.254	2	58.725	13.412
L4	34.335	0.280	2	24.968	45.143
L5	34.335	0.077	2	3.640	15.095
L6	34.335	0.193	2	7.635	37.179
L7	34.335	0.056	2	56.350	10.345
L8	34.335	0.015	2	13.578	0.892
L9	34.335	0.023	2	0.000	4.475
L10	34.335	0.004	2	0.000	0.700

Table 6.2. Minimum axial preloads for the clamping of the lenses.

Since the calculated values of the axial preloads are the minimum required, the actual preloads applied to the optical components have to be equal to or higher than them, provided that the resulting contact stresses in the optical components are not excessively high. Practically, the actual values of the applied preloads will depend on the selected mechanical components that will exert the forces; namely, on the provided stiffnesses. Besides the axial preloads, the components M1, M2 and M3 require a radial force, i.e. a nesting force, so that the corresponding movement is also constrained. This force is selected to be equal to that applied in the axial direction.

In Table 6.3 the parameters are presented, based on which the COTS metallic springs have been selected for the application of the necessary preloads (Table 6.1, Table 6.2). Besides those parameters, the diameters and free lengths have been considered as well. More information about the latter can be found in the datasheets of the parts (the links are provided in Appendix C). Regarding the cost, no information is available without an RfQ. It should be noted that for the components M1, M2 and M3 more than one (identical) springs are used for the preload application in the axial and/or radial direction. In every case these springs are connected in parallel.

Part No.	Subassembly	Max. load [N]	Spring rate [N/mm]	Resistance to corrosion	On stock
LHP 192L 03S	M1 (axial direction)	1,743.21	233.487	✓	✓
LHP 218L 02 S	M1 (radial direction)	2,620.18	469.246	✓	✓
SSB-1339	L1	934.5	198	✓	✓
LC 135JK 01S	M2 (axial direction)	633.52	93.852	✓	✓
LC 112J 02 S316	M3 (axial direction)	482.07	45.64	✓	✓
YRW-0587	L2	2,046.18	1,239.37	✓	✓
YRW-0475	L3-L4	1,668.08	980.18	✓	✓

Table 6.3. Parameters for the selection of the COTS metallic springs for the application of the preloads.

In some cases, custom-made cantilevered springs are used for the application of the radial or axial preloads. As discussed in subsection 4.2.3.2, the stiffness of these springs depends on the elastic properties of the selected material as well as the spring geometry. Based on the classical beam theory, the total deflection of the spring(s) is given by (Yoder & Vukobratovich^[32]):

$$\delta = \frac{4Fl^3(1-\nu_M^2)}{Nbt^3E_M} \quad (6.1)$$

where:

- F : the applied preload [N]
- N : the number of springs [-]
- E_M : the Young's modulus of the material used [Pa]
- ν_M : the Poisson's ratio of the material used [-]
- l : the free length of the spring [m]
- b : the spring width [m]
- t : the spring thickness [m]

In order for N cantilevered springs to operate in the elastic region (i.e. not to be plastically deformed) for a given preload F , the resulting bending stress has to stay below the yield strength, σ_y , of the material used. The bending stress is defined as (Yoder & Vukobratovich^[32]):

$$\sigma_B = \frac{6Fl}{Nbt^2} \quad (6.2)$$

A safety factor between 1.5 and 2 is typically used to define the MoS of the spring design. For all cantilevered springs the Copper-Beryllium alloy UNS C17200^[70] is used and the selected temper is AT (TF00). It should be noted that other materials can also be used, such as Ti6Al4V, stainless steel 1.4310, CuSn6 and stainless steel 17-7. Depending on the material choice, the geometry of the springs has to be defined such that the yield strength of the material is not exceeded (i.e. the deformation of the spring remains in the elastic region). Lastly, the resistance to corrosion is also important, in order to avoid the occurrence of stress corrosion cracking, given that the springs are subjected to tensile stress.

In addition, O-rings are used for the application of the preloads for the mirrors M4, M5, M7, M8 and M9. In all cases a 10% compression is selected, so that preloads of moderate magnitudes (i.e. neither lower nor much higher than the minimum required) can be applied for a specific hardness of the O-ring material. Moreover, a desirable property is the compliance of the O-ring; namely, relatively soft O-rings can accommodate manufacturing errors, as discussed in subsection 4.2.3.2. Aside from that, the temperature range within which the O-ring material remains flexible and the maximum compression set should be considered in the selection of the most suitable O-rings. Lastly, the exact dimensions (inner diameter and cross section) as well as the availability of the selected component are important. Similar to the metallic springs discussed earlier, information about the cost of these components is not readily available.

In the following diagram, the percent compression as a function of the cross section, the applied preload per unit length of the midline circumference of the O-ring and the material hardness is presented as an example. It can be observed that for a specific hardness the preload per unit length of the midline circumference can be selected within a range of values, which means that the preload is not as well-defined as in the case of a metallic spring.

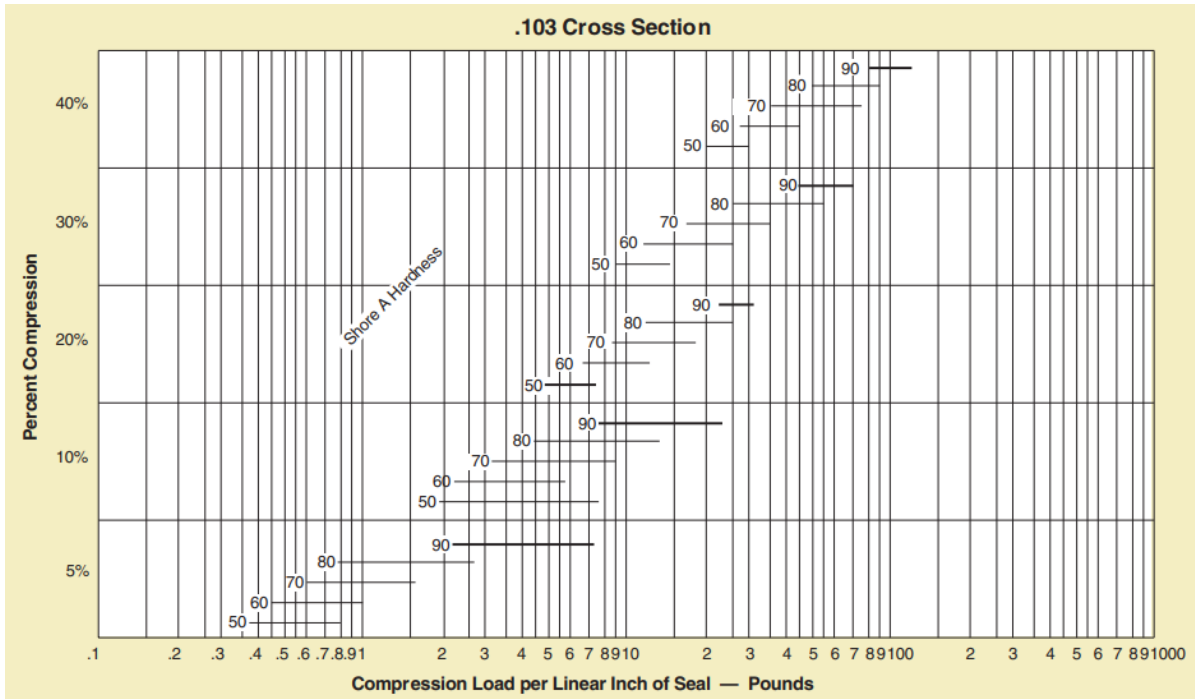


Table 6.4. O-ring compression for a cross section of approximately 2.6 mm (0.103 in) [71].

In Table 6.5 the properties of the selected O-rings are summarized. These values are based both on the Parker O-ring Handbook^[71] as well as the datasheets of the components (the links are provided in Appendix C).

Part Name	Subassembly	Shore A hardness	Compression set [%]	Temperature range [°C]	On stock
Si 970, FL	M4	70	4.5*	-60 to +200	✓
FKM LT 170	M5	70	14**	-50 to +200	✓
Si 820	M7	70	4.5*	-55 to +200	✓
Si 850	M8	50	4.5*	-55 to +200	✓
FKM LT 170	M9	70	18*	-50 to +200	✓

*: At 93.3 °C, after 22 hours and for a cross section of approximately 1.8 mm.

** : At 93.3 °C, after 22 hours and for a cross section of approximately 3.5 mm.

Table 6.5. Parameters for the selection of the O-rings for the application of the preloads.

Below, the applied preloads and the resulting contact stresses are summarized. In the case of M1, M2 and M3 the maximum radial contact stresses exist between the mirror and the posts. In most of the cases, the calculation of the contact stresses is based on the Hertzian contact theory, according to which *eq. (4.9)* to *(4.15)* are derived. Moreover, the mechanical properties of the materials used for the calculations are presented in Appendix B.

Component	Axial preload [N]	Axial σ_c [MPa]	Axial σ_t [MPa]	Radial preload [N]	Max. radial σ_c [MPa]	Max. radial σ_t [MPa]
M1	2,297.621	0.977*	0.190*	2,297.621	138.203*	26.904*
M2	1,126.969	0.628*	0.122*	1,126.969	108.801*	21.180*
M3	550.091	0.306*	0.060*	550.091	84.202*	16.391*
M4	75	1.002	0.195	N.A.	N.A.	N.A.
M5	85	1.013	0.197	N.A.	N.A.	N.A.
M6	16	63.612*	12.383*	N.A.	N.A.	N.A.
M7	70	0.802	0.156	N.A.	N.A.	N.A.
M8	42	0.901	0.175	N.A.	N.A.	N.A.
M9	60	1.302	0.253	N.A.	N.A.	N.A.

*: per contact.

Table 6.6. Applied preloads and calculated contact stresses for all mirrors.

Component	Axial preload [N]	σ_c on front surface [MPa]	σ_t on front surface [MPa]	σ_c on rear surface [MPa]	σ_t on rear surface [MPa]
L1	900	0.857	0.167	0.527	0.103
L2	165	1.218	0.237	0.973	0.189
L3	120	1.025	0.200	2.541	0.495
L4	120	1.399	0.272	1.905	0.371
L5	42	0.493	0.096	0.570	0.111
L6	42	1.148*	0.224*	29.502*	5.743*
L7	12	67.584*	13.156*	11.543*	2.247*
L8	8	2.629	0.512	0.052	0.010
L9	8	0.069	0.013	0.041	0.008
L10	3	13.955*	2.717*	47.802*	9.305*

*: per contact.

Table 6.7. Applied preloads and calculated contact stresses for all lenses.

As a rule of thumb, the upper limits for the compressive and tensile stresses in glass are 345 MPa and 6.9 MPa, respectively (Schwertz & Burge^[28]). In the above calculations the use of Kapton tape/foil has not been taken into account; thus, the magnitudes of the stresses represent the worst case. For instance, in the case of M6, the compressive contact stress between the spring and the Kapton foil is equal to 15.2 MPa, i.e. approximately four times lower than the value presented in *Table 6.6*. In addition, an increase in the radius of the toroidal part of the spring contacting the optical component would lead to a decrease in the contact stresses. Consequently, a more detailed analysis of the mount-induced contact stresses and the optimization of the contact geometry are necessary, especially for lenses, for which stress birefringence needs to be investigated as well.

The lenses L1 through L5 have an annular contacting IF on both sides; therefore, they can be used to demonstrate the influence of the interface geometry and the material selection on the magnitude of the mount-induced stresses. In the following graphs, the compressive and tensile contact stresses on the front and rear surfaces of the optical components are illustrated for four different cases. In the first two cases, the contacting IF is tangential or toroidal, depending on the shape of the lens, and the contacting material is either PEEK GF30 or aluminum. In the last two cases, a sharp-corner IF is used for the same material selections. In all cases the material of the optical components is BK7. From the graphs presented below it can be concluded that while the material selection of the mechanical IF influences the magnitude of the developed stresses to some degree, the impact of the IF geometry is predominant. It should be noted that the spherical IF has not been investigated because it is rarely used in practice.

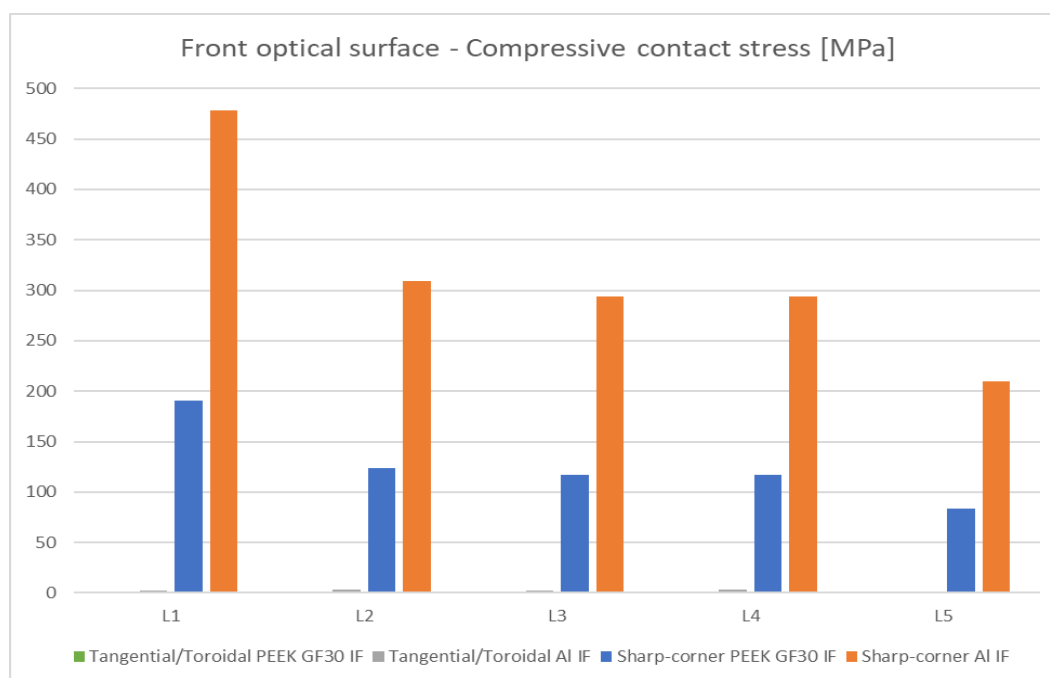


Figure 6.1. Mount-induced compressive contact stresses on the front optical surfaces of lenses L1 through L5 for different IF materials and geometries.

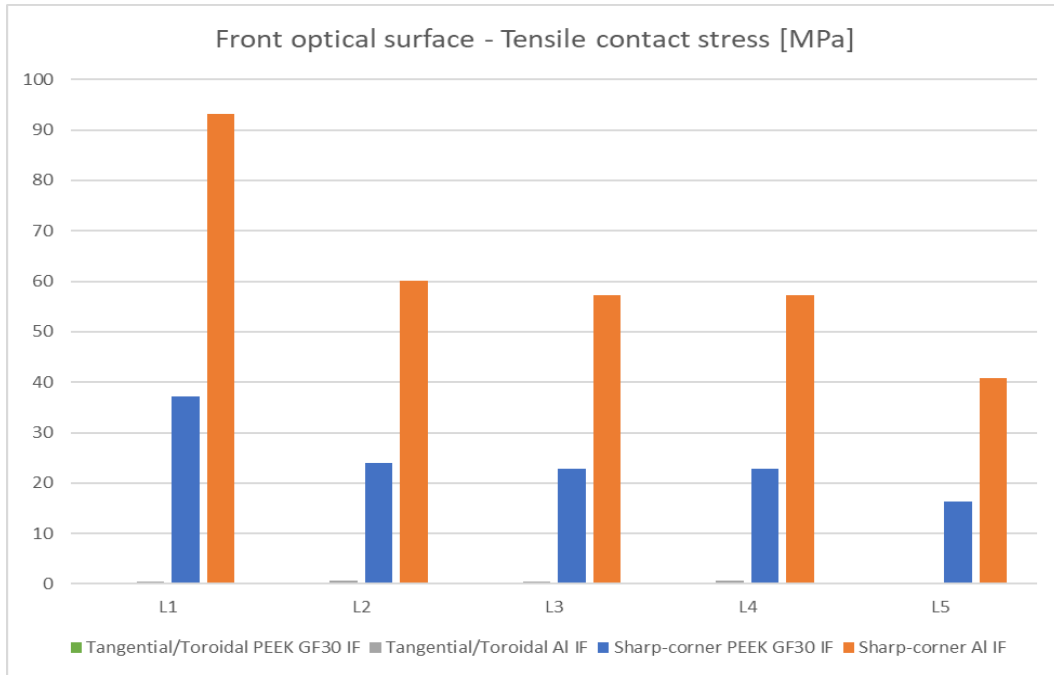


Figure 6.2. Mount-induced tensile contact stresses on the front optical surfaces of lenses L1 through L5 for different IF materials and geometries.

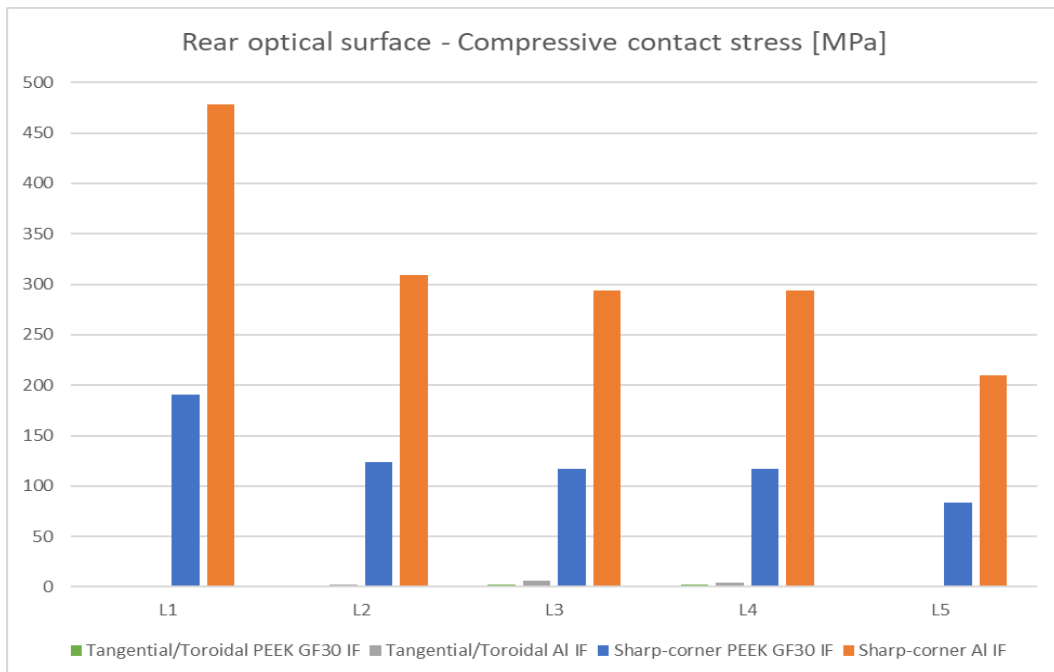


Figure 6.3. Mount-induced compressive contact stresses on the rear optical surfaces of lenses L1 through L5 for different IF materials and geometries.

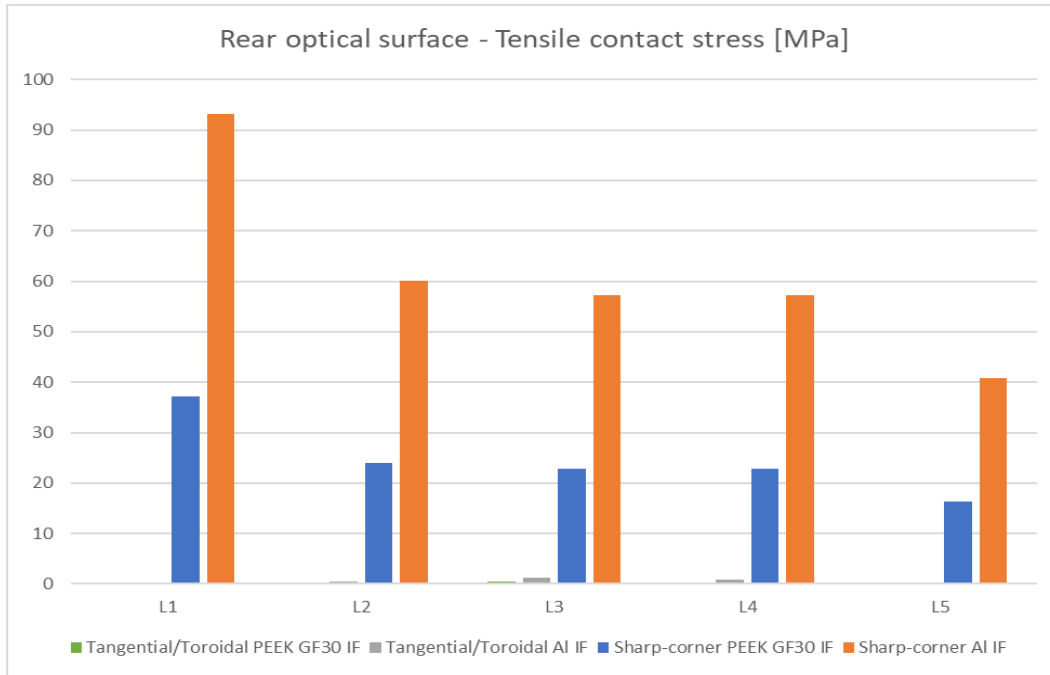


Figure 6.4. Mount-induced tensile contact stresses on the rear optical surfaces of lenses L1 through L5 for different IF materials and geometries.

In Table 6.8 the geometry of all custom-made springs is summarized and the deflections and bending stresses for the given axial preloads are calculated based on eq. (6.1) and (6.2). As discussed earlier, the material used is a Copper-Beryllium alloy and its mechanical properties can be found in Appendix B.

Component/ Subassembly	F [N]	Number of springs	l [mm]	b [mm]	t [mm]	δ [mm]	σ_B [MPa]
M2	1,126.969	1	52	26	5.5	1.018	447.062
M3	550.091	1	45	26	3.5	1.249	466.325
M6	16	3	5.5	15	0.3	0.076	130.370
L5-L6	42	40	2.5	4.28	0.15	0.032	163.437
L7	12	3	4.5	5	0.25	0.130	345.600
L8-L9	8	30	4.53	1.79	0.15	0.114	180.054
L10	3	3	4	5	0.15	0.105	213.333

Table 6.8. Deflection and bending stress in custom-made springs.

In the description of the design of the M2 and M3 mounts it has been mentioned that cantilevered springs are usually used when the magnitudes of the required preloads are relatively low. Thus, it has been suggested that the way in which the preloads are applied in the radial direction needs to be reconsidered. Furthermore, from the above calculations it can be observed that the deflections of the springs for M6 and the L5-L6 subassembly are very small, i.e. the springs are too stiff. The stiffness can be decreased if the free length is increased and/or the width and thickness are decreased, as long as the resulting bending stress is lower than the yield strength of the material of the spring.

6.2 Preload variations with temperature

In subsection 4.2.4 the calculation of the required axial preload has been discussed and its variation as a result of temperature changes has been briefly introduced. More precisely, for a given temperature difference, the coefficient K_3 in eq. (4.8) determines the magnitude of the preload change. For the calculation of the preload variations in the SLAO system over the given operational and survival temperature ranges (Table 3.1) K_3 is considered to be a function of the CTEs of the materials used (or the differences thereof) and the stiffnesses of the mechanical elements selected for the application of the required preloads. In this section, the preload changes in the axial and radial directions are presented for every subassembly in the survival and operational case. The reference temperature for all calculations is assumed equal to 20 °C. The axial and radial preloads for the upper and lower limits of the survival and operational ranges and the resulting contact stresses can be found in Appendix D.

Component	F [N]	$\Delta F_{@-33\text{ }^\circ\text{C}}$ [N]	$\Delta F_{@+85\text{ }^\circ\text{C}}$ [N]	$\Delta F_{@0\text{ }^\circ\text{C}}$ [N]	$\Delta F_{@+15\text{ }^\circ\text{C}}$ [N]
M1	2,297.621	+23.723	-29.094	+8.952	+2.238
M2	1,126.969	+7.205	-8.836	+2.719	+0.680
M3	550.091	+2.885	-3.539	+1.089	+0.272
M6	16	+3.517	-4.313	+1.327	+0.332

Table 6.9. Axial preload change with temperature for mirrors M1, M2, M3 and M6.

Component	C [%]	$\Delta C_{@-33\text{ }^\circ\text{C}}$ [%]	$\Delta C_{@+85\text{ }^\circ\text{C}}$ [%]	$\Delta C_{@0\text{ }^\circ\text{C}}$ [%]	$\Delta C_{@+15\text{ }^\circ\text{C}}$ [%]
M4	10	-0.668	+0.819	-0.252	-0.063
M5	10	-0.645	+0.791	-0.244	-0.061
M7	10	-0.600	+0.736	-0.227	-0.057
M8	10	-0.599	+0.734	-0.226	-0.056
M9	10	-0.741	+0.908	-0.280	-0.070

Table 6.10. O-ring compression change with temperature.

Component	F [N]	$\Delta F_{@-33\text{ }^\circ\text{C}}$ [N]	$\Delta F_{@+85\text{ }^\circ\text{C}}$ [N]	$\Delta F_{@0\text{ }^\circ\text{C}}$ [N]	$\Delta F_{@+15\text{ }^\circ\text{C}}$ [N]
M1	2,297.621	+269.029	-329.941	+101.520	+25.380
M2	1,126.969	+283.112	-347.213	+106.835	+26.709
M3	550.091	+73.229	-89.809	+27.633	+6.908

Table 6.11. Radial preload change with temperature for mirrors M1, M2 and M3.

Component	F [N]	$\Delta F_{@-33\text{ }^{\circ}\text{C}}$ [N]	$\Delta F_{@+85\text{ }^{\circ}\text{C}}$ [N]	$\Delta F_{@0\text{ }^{\circ}\text{C}}$ [N]	$\Delta F_{@+15\text{ }^{\circ}\text{C}}$ [N]
L1	900	+4.097	-5.025	+1.546	+0.387
L2	165	+30.320	-37.185	+11.441	+2.860
L3-L4	120	+4.204	-5.155	+1.586	+0.397
L5-L6	42	-4.344	+5.328	-1.639	-0.410
L7	12	+1.626	-1.994	+0.614	+0.153
L8-L9	8	+0.156	-0.191	+0.059	+0.015
L10	3	+0.063	-0.078	+0.024	+0.006

Table 6.12. Axial preload change with temperature for all lenses.

From the last table it can be observed that the calculated preload variations do not lead to a reduction of the preload magnitudes below the minimum values presented in Table 6.2. This means that in the case of lenses, even a combination of load cases, i.e. acceleration and temperature change, will theoretically not influence the position accuracy of the mounted optical component(s). Practically, however, settling effects right after integration might cause small shifts in the presence of vibrations and/or shock. Moreover, as mentioned earlier, all mirrors in the SLAO system are flat; thus, they are insensitive to lateral shifts. Therefore, in the case of mirrors the preload variations in the axial direction are more important. From the first three tables it can be seen that these variations are relatively small.

For the O-rings used for the application of the axial preloads, the effect of the compression set on the thicknesses of the components can be investigated. The recovered thickness is calculated based on the formula (Parker O-ring Handbook⁽⁷¹⁾):

$$t_i = t_o - \frac{CS}{100}(t_o - t_s) \quad (6.3)$$

where:

t_i : the recovered thickness [mm]

t_o : the original thickness [mm]

t_s : the height of the gap within which the O-ring is compressed, as defined by the selected percent compression (here 10%) [mm]

CS: the percent compression set (Table 6.5)

In the following table the recovered thickness, t_i , as well as the reduced percent compression, C' , as a result of the compression set are provided for the O-rings used in the SLAO system. It can be observed that there is a small loss in compression (and thus in the preload). However, the compression set is considered for a slightly higher temperature than the maximum survival temperature expected. Therefore, the losses in preload will be a little lower than the calculated ones.

Component	CS [%]	t_o [mm]	t_s [mm]	t_i [mm]	C' [%]
M4	4.5	2.5	2.25	2.49	9.6
M5	14	3	2.7	2.96	8.7
M7	4.5	2	1.8	1.99	9.6
M8	4.5	2	1.8	1.99	9.6
M9	18	2	1.8	1.96	8.4

Table 6.13. Recovered thickness and reduction of percent compression due to compression set.

6.3 Optomechanical tolerance analysis

A deviation from the theoretical position of an optical component might affect the optical performance of the entire system. Since in practice manufacturing errors are unavoidable, they have to remain within predefined limits, i.e. tolerances. Clearly, the tighter the tolerances are, the higher the manufacturing cost becomes; for that reason, a balance between performance and cost needs to be found. In this section the tolerances of every subassembly and subsystem in the SLAO system are analyzed and the overall errors are determined.

In the book by Yoder & Vukobratovich^[32] and the publication by Ginsberg^[72] the error analysis for an optomechanical system is discussed and every step involved in the allocation of the error budget is addressed with the aid of the block diagram illustrated in *Figure 6.5*. Generally, the requirements for the design of a system are determined in accordance with its performance specifications and mechanical constraints (e.g. size, mass), and, if applicable, its operational environment. The defined requirements are then used for the high-level (i.e. preliminary) optical and (opto)mechanical design, during which concepts are developed and evaluated, the design principle(s) used is/are examined and the architecture of the system is determined.

Subsequently, the error budgeting is performed through the tentative assignment of tolerances for every optical and (opto)mechanical component and assembly, based on experience and common manufacturing practices (item 7 in the figure), and with the use of a sensitivity table. The sensitivity of every parameter included in this table determines the impact of a potential (parameter) change on the performance of the system. Next, the developed layout is checked against the existing requirements and constraints (item 10). There are different ways in which the overall effect of the errors on the performance of the system can be estimated, e.g. the RSS or the Monte Carlo method. When the budgeted parameter changes are estimated to produce a system, whose performance meets the requirements, these changes can be used as tolerances in the drawings of the optical and mechanical components. For the design to reach maturity a number of iterations are necessary, in which the former is improved and the tolerance budget is updated.

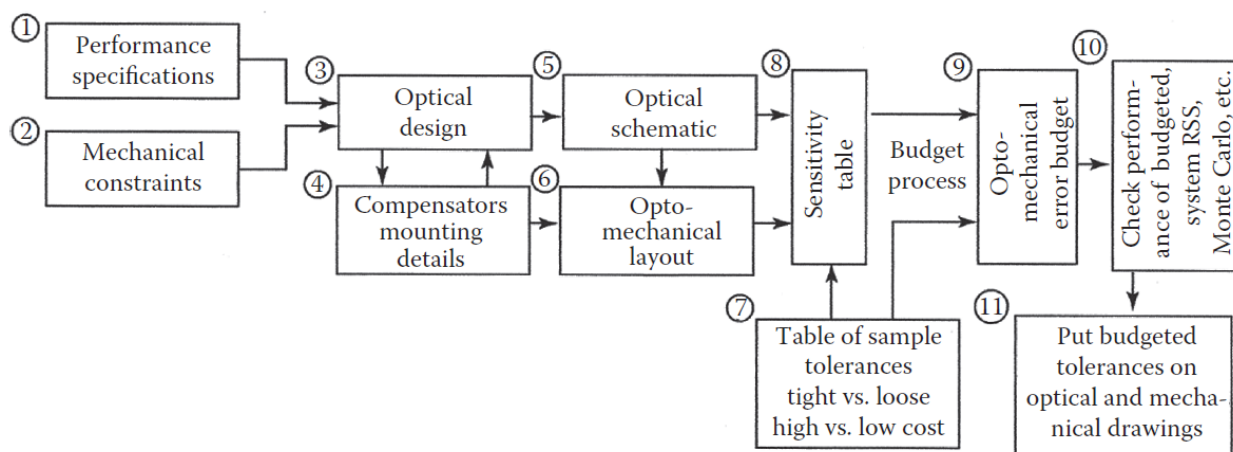


Figure 6.5. Block diagram representing a typical application of tolerances to an optomechanical system [32].

In this thesis the focus is placed on the definition of the tolerances related to the mounting of the optical components, based on the preliminary design presented in the previous chapter. Generally, these tolerances include spacing deviations, tilt, decenter, thermomechanical drift and the dynamic effects of external loads (e.g. accelerations, forces, shocks). The tolerances associated with the optical components, such as the geometry, material and optical surface are not included. Moreover, since the optomechanical design is still at a preliminary stage, neither the thermomechanical drift nor the dynamic effects are considered in the present tolerance analysis; namely, only the static position errors are taken into account. For the tolerance analysis coordinate systems for every subassembly and subsystem are defined, as illustrated in the following figure.

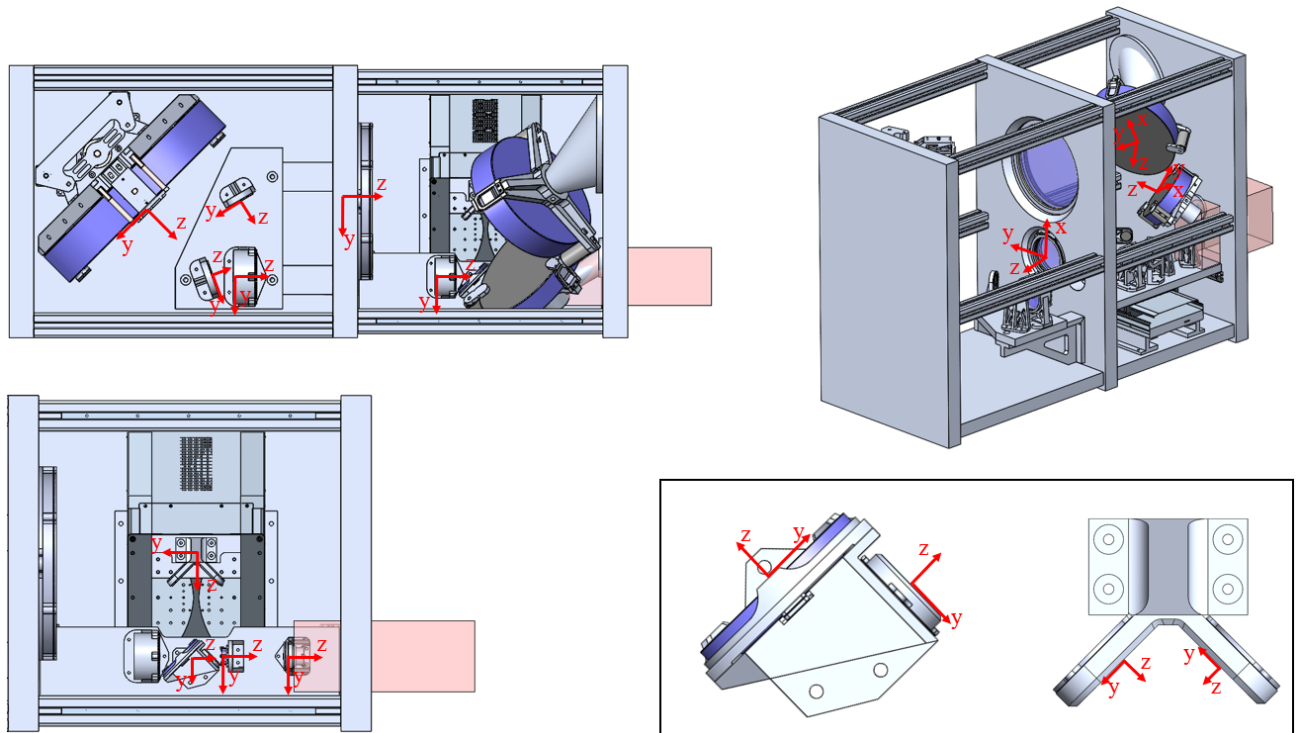


Figure 6.6. Mechanical coordinate systems.

For every subassembly and subsystem in the SLAO system the expected linear and angular deviations from the nominal position are defined and the overall error is estimated as the RSS, assuming that these deviations are independent of each other. The general manufacturing tolerances for linear and angular dimensions are based on the norm DIN ISO 2768-1 (1991-06), which can be found in the book by Fischer et al.^[73]. In the following tables, the error budgets for the SLAO system are summarized. The linear and/or angular shifts that have an influence on the performance of the optical components are indicated in bold font. Lastly, for the estimation of the total position errors a bottom-up analysis has been followed.

M1							
In	dx [mm]	dy [mm]	dz [mm]	rx [°]	ry [°]	rz [°]	Out
M1 → M1 mount	0.200	0.100	0.150	0.040	0.030	0.050	M1 assembly
M1 assembly → sliders	0.000	0.050	0.100	0.030	0.010	0.010	M1 subsystem
M1 subsystem → SLAO support structure	0.000	0.002	0.020	0.006	0.000	0.000	
Total error	0.200	0.114	0.181	0.050	0.032	0.051	

Table 6.14. M1 – Tolerance analysis.

M2							
In	dx [mm]	dy [mm]	dz [mm]	rx [°]	ry [°]	rz [°]	Out
M2 → M2 mount	0.150	0.200	0.150	0.060	0.060	0.060	M2 assembly
M2 assembly → M2 IF	0.040	0.040	0.020	0.000	0.000	0.000	M2 total assembly
M2 total assembly → SLAO support structure	0.020	0.020	0.030	0.006	0.009	0.005	
Total error	0.157	0.205	0.154	0.060	0.061	0.060	

Table 6.15. M2 – Tolerance analysis.

M3							
In	dx [mm]	dy [mm]	dz [mm]	rx [°]	ry [°]	rz [°]	Out
M3 → M3 mount	0.200	0.150	0.150	0.100	0.060	0.050	M3 assembly
M3 assembly → M3 IF	0.040	0.040	0.020	0.000	0.000	0.000	M3 total assembly
M3 total assembly → SLAO support structure	0.020	0.020	0.030	0.018	0.018	0.016	
Total error	0.205	0.157	0.154	0.102	0.063	0.052	

Table 6.16. M3 – Tolerance analysis.

M4							
In	dx [mm]	dy [mm]	dz [mm]	rx [°]	ry [°]	rz [°]	Out
M4 → M4 mount	0.100	0.100	0.020	0.030	0.030	0.000	M4 assembly
M4 assembly → Mount. plate	0.150	0.020	0.020	0.024	0.040	0.020	M4 assembly w/ mount. plate
Mount. plate → SLAO support structure	0.020	0.020	0.020	0.004	0.007	0.005	
Total error	0.181	0.104	0.035	0.039	0.050	0.021	

Table 6.17. M4 – Tolerance analysis.

M5							
In	dx [mm]	dy [mm]	dz [mm]	rx [°]	ry [°]	rz [°]	Out
M5 → M5 mount	0.100	0.100	0.020	0.020	0.020	0.000	M5 assembly
M5 assembly → Mount. plate	0.150	0.020	0.020	0.019	0.040	0.017	M5 assembly w/ mount. plate
Mount. plate → SLAO support structure	0.020	0.020	0.020	0.004	0.007	0.005	
Total error	0.181	0.104	0.035	0.028	0.045	0.018	

Table 6.18. M5 – Tolerance analysis.

M6							
In	dx [mm]	dy [mm]	dz [mm]	rx [°]	ry [°]	rz [°]	Out
M6 → M6 cell	0.100	0.100	0.020	0.012	0.017	0.000	M6 assembly
M6 cell → M6-M9 mount	0.020	0.020	0.020	0.011	0.014	0.030	
M6-M9 mount → Mount. plate	0.150	0.020	0.020	0.015	0.025	0.020	M6-M9 mount w/ mount. plate
Mount. plate → SLAO support structure	0.014	0.014	0.014	0.013	0.003	0.013	
Total error	0.182	0.105	0.037	0.026	0.033	0.038	

Table 6.19. M6 – Tolerance analysis.

M7							
In	dx [mm]	dy [mm]	dz [mm]	rx [°]	ry [°]	rz [°]	Out
M7 → M7-M8 mount	0.100	0.100	0.020	0.025	0.025	0.000	M7 assembly
M7-M8 mount → Adapter plate	0.100	0.020	0.020	0.019	0.056	0.021	M7-M8 mount w/ adapter plate
Adapter plate → Translation stage	0.100	0.020	0.020	0.008	0.020	0.010	
Translation stage → SLAO support structure	0.150	0.020	0.020	0.004	0.004	0.005	
Total error	0.229	0.106	0.040	0.033	0.065	0.024	

Table 6.20. M7 – Tolerance analysis.

M8							
In	dx [mm]	dy [mm]	dz [mm]	rx [°]	ry [°]	rz [°]	Out
M7 → M7-M8 mount	0.100	0.100	0.020	0.029	0.029	0.000	M8 assembly
M7-M8 mount → Adapter plate	0.100	0.020	0.020	0.019	0.056	0.021	M7-M8 mount w/ adapter plate
Adapter plate → Translation stage	0.100	0.020	0.020	0.008	0.020	0.010	
Translation stage → SLAO support structure	0.150	0.020	0.020	0.004	0.004	0.005	
Total error	0.229	0.106	0.040	0.036	0.066	0.024	

Table 6.21. M8 – Tolerance analysis.

M9							
In	dx [mm]	dy [mm]	dz [mm]	rx [°]	ry [°]	rz [°]	Out
M9 → M6-M9 mount	0.100	0.100	0.020	0.029	0.029	0.000	M9 assembly
M6-M9 mount → Mount. plate	0.150	0.020	0.020	0.015	0.025	0.020	M6-M9 mount w/ mount. plate
Mount. plate → SLAO support structure	0.014	0.014	0.014	0.013	0.003	0.013	
Total error	0.181	0.103	0.032	0.035	0.038	0.024	

Table 6.22. M9 – Tolerance analysis.

L1							
In	dx [mm]	dy [mm]	dz [mm]	rx [°]	ry [°]	rz [°]	Out
L1 → L1 cell	0.200	0.200	0.100	0.005	0.005	0.000	L1 assembly
L1 assembly → Middle block	0.020	0.020	0.100	0.004	0.004	0.003	
Total error	0.201	0.201	0.141	0.006	0.006	0.003	

Table 6.23. L1 – Tolerance analysis.

L2							
In	dx [mm]	dy [mm]	dz [mm]	rx [°]	ry [°]	rz [°]	Out
L2 → L2 cell	0.100	0.100	0.050	0.010	0.010	0.000	L2 assembly
L2 assembly → Middle block	0.020	0.020	0.100	0.010	0.010	0.006	
Total error	0.102	0.102	0.112	0.014	0.014	0.006	

Table 6.24. L2 – Tolerance analysis.

L3-L4							
In	dx [mm]	dy [mm]	dz [mm]	rx [°]	ry [°]	rz [°]	Out
L3 → L3-L4 mount	0.075	0.075	0.050	0.014	0.0140	0.000	
L4 → L3-L4 mount	0.075	0.075	0.050	0.014	0.0140	0.000	L3-L4 assembly
L3-L4 assembly → Mount. plate	0.100	0.020	0.020	0.015	0.017	0.012	L3-L4 assembly w/ mount. plate
Mount. plate → SLAO support structure	0.020	0.020	0.020	0.004	0.007	0.005	
Total error	0.147	0.110	0.076	0.025	0.027	0.013	

Table 6.25. L3-L4 – Tolerance analysis.

L5-L6							
In	dx [mm]	dy [mm]	dz [mm]	rx [°]	ry [°]	rz [°]	Out
L5 → L5-L6 mount	0.050	0.050	0.050	0.020	0.020	0.000	
L6 → L5-L6 mount	0.050	0.050	0.050	0.020	0.020	0.000	L5-L6 assembly
L5-L6 assembly → Mount. plate	0.100	0.020	0.020	0.018	0.020	0.017	L5-L6 assembly w/ mount. plate
Mount. plate → SLAO support structure	0.014	0.014	0.014	0.013	0.003	0.013	
Total error	0.123	0.075	0.075	0.036	0.035	0.021	

Table 6.26. L5-L6 – Tolerance analysis.

L7							
In	dx [mm]	dy [mm]	dz [mm]	rx [°]	ry [°]	rz [°]	Out
L7 → L7 cell	0.050	0.050	0.050	0.050	0.040	0.000	
L7 assembly → L7 mount	0.020	0.020	0.050	0.060	0.060	0.020	L7 assembly
L7 mount → Mount. plate	0.100	0.020	0.020	0.046	0.060	0.030	L7 assembly w/ mount. plate
Mount. plate → SLAO support structure	0.014	0.014	0.014	0.013	0.003	0.013	
Total error	0.114	0.059	0.075	0.092	0.094	0.038	

Table 6.27. L7 – Tolerance analysis.

L8-L9-L10							
In	dx [mm]	dy [mm]	dz [mm]	rx [°]	ry [°]	rz [°]	Out
L9 → L8-L9-L10 tube	0.050	0.050	0.100	0.060	0.060	0.000	
L8 → L8-L9-L10 tube	0.050	0.050	0.100	0.045	0.045	0.000	
L10 → L8-L9-L10 tube	0.050	0.050	0.050	0.060	0.060	0.000	
L8-L9-L10 tube → L8-L9-L10 mount	0.020	0.020	0.050	0.030	0.030	0.023	L8-L9-L10 assembly
L8-L9-L10 assembly → Mount. plate	0.100	0.020	0.020	0.038	0.020	0.025	L8-L9-L10 assembly w/ mount. plate
Mount. plate → SLAO support structure	0.014	0.014	0.014	0.013	0.003	0.013	
Total error	0.135	0.092	0.160	0.108	0.103	0.036	

Table 6.28. L8-L9-L10 – Tolerance analysis.

In the present tolerance analysis, the tolerances regarding the angular separation between the pairs M6-M9 and M7-M8 and those related to the fabrication and assembly of the support structure have not been considered. In addition, the compression of the Kapton foil is considered negligible. Moreover, in most cases a rotation of the (mounted) optical component about the optical axis has no effect on the performance of the system. This assumption should be investigated in the case of L10, which is the lenslet array. Lastly, the resulting overall position errors, need to be compared to the allowable errors provided by the optical design, so as to determine the necessary improvements in the (opto)mechanical design and at the same time gain an insight into the total cost.

As discussed in Section 6.1, for the calculation of the minimum required preloads in the case of all mirrors in the SLAO system the friction between the optical components and the mounts has not been taken into account, since they are flat (i.e a lateral displacement would not degrade their optical performance). By contrast, in the case of lenses the coefficient of static friction as well as the clamping angle have been taken into account in the corresponding preload calculations. Nonetheless, for the pickup mirror, the virtual play in the horizontal and vertical directions can be estimated in order to determine the tolerances in the dimensions of the central opening (besides the contribution of the total static position error).

Generally, preload variations (e.g. due to inertia and/or thermal loads) might lead to relative movement between the contacting surfaces. This movement results in the development of friction forces in the direction opposite to the movement and tangentially to the contacting surfaces, which, in turn, cause a tangential deflection, δ_t . This tangential deflection depends on the magnitude of the friction force F_f , the radius of the contact area r and the mechanical properties (G and ν) of the contact material. Based on the tangential deflection, the tangential stiffness of the contact can be calculated (Schouten et al.^[74]):

$$c_t = \frac{F_f}{\delta_t} \quad (6.4)$$

The corresponding local normal stiffness of the contact is given by (Schouten et al.^[74]):

$$c_n = \frac{2-\nu}{2(1-\nu)} c_t \quad (6.5)$$

In the following figure the contact between a sphere and a V-shaped groove is depicted, including the modeling of the tangential and normal stiffnesses which are represented by springs in the corresponding directions (assuming that the deformation of the material is elastic).

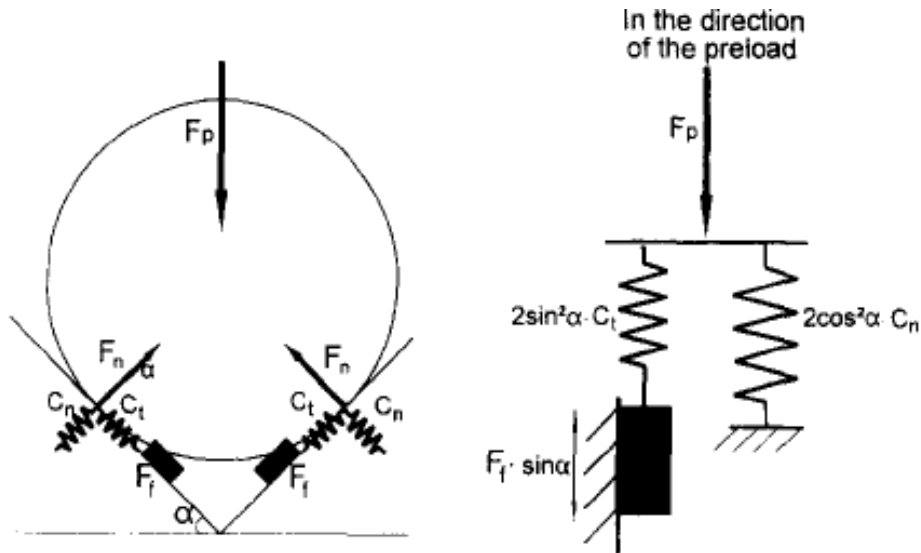


Figure 6.7. Schematic diagram of a sphere in a V-groove [74].

If the variation of the preload (F_p in the figure above) is large enough to allow for a relative movement between the sphere and the V-groove, then it is uncertain whether the relative positions of the contacting surfaces will coincide with the original ones, once the preload variation ceases to exist. This uncertainty, which is called hysteresis, results in low repeatability in the positioning of the component (here the sphere). The virtual play, which represents the positional uncertainty due to hysteresis, can be calculated based on the following expression (Schouten et al.^[74]):

$$s_v = \frac{2 \cdot |F_f|}{c} \quad (6.6)$$

where c is the stiffness in the direction of the friction.

The maximum friction force is proportional to the reaction force F_n with the proportionality constant being the coefficient of static friction. Thus, the virtual play can be decreased by reducing the friction coefficient (besides increasing the stiffness of the contact). Moreover, using geometry and for a given angle α of the groove (Figure 6.7) and a known coefficient of static friction between the two contacting surfaces, the virtual play in the horizontal and vertical directions can be calculated.

In the case of the M1 the magnitudes of the horizontal and vertical virtual play for different load cases are presented in the following table.

Temperature [°C]	Acceleration [g]	c_t [N/mm]	c_n [N/mm]	s_{vx} [mm]	s_{vy} [mm]
+20	1	3.124×10^5	3.794×10^5	0.009	0.004
-33	1	3.115×10^5	3.782×10^5	0.010	0.005
+85	1	3.135×10^5	3.807×10^5	0.008	0.004
0	1	3.120×10^5	3.789×10^5	0.010	0.004
+15	1	3.123×10^5	3.793×10^5	0.010	0.004
+20	3.5	2.579×10^5	3.131×10^5	0.016	0.007
-33	3.5	2.565×10^5	3.114×10^5	0.014	0.006
+85	3.5	2.595×10^5	3.152×10^5	0.012	0.005
0	3.5	2.574×10^5	3.126×10^5	0.013	0.006
+15	3.5	2.578×10^5	3.130×10^5	0.012	0.005

Table 6.29. Virtual play in the horizontal and vertical direction for different load cases.

In the above calculations the thickness of the mirror has not been taken into account for the sake of simplicity; namely, it has been assumed that all forces are coplanar and act on the plane passing through the CoG of the pickup mirror. In reality, however, the stiffnesses of the contact are distributed over the entire contact length.

In addition, virtual play exists, theoretically, in every connection in the SLAO system and should be studied extensively as the (opto)mechanical design of the system becomes more detailed. Besides that, it can be observed that the magnitude of the virtual play, even in the worst load case, is much smaller than the previously calculated static position errors in the system, which, however, can be minimized during the optical alignment of the components.

6.4 Mass estimate

The mass of every subassembly and subsystem in the SLAO system is summarized in *Table 6.30* and the total mass is calculated, including the total mass with a 30% contingency. The mass of the mechanical support of the SLAO system on METIS's platform has not been considered in this report and, thus, it is not included in the mass budget.

Assembly/Subsystem	Mass [kg]
SLAO support structure	496.5
M1 subsystem	86.2
L1 assembly	6.9
M2 assembly	20.0
M3 assembly	13.0
L2 assembly	1.0
M4 assembly	0.4
M5 assembly	0.5
L3-L4 assembly	1.5
L5-L6 assembly	0.9
M6-M9 assembly	1.0
M7-M8 subsystem	33.0
L7 assembly	0.2
L8-L9-L10 assembly	0.4
Camera	4.5
Sheets for cleanliness	20.3
Total mass	686.3
Total mass with 30% contingency	892.2

Table 6.30. Total mass of the SLAO system.

From the figures presented above it can be observed that the highest contribution is attributed to the support structure of the system. Nonetheless, given that the blocks used are, currently, merely three aluminum slabs, an optimization of their mass and stiffness will considerably reduce the mass of the support structure and, consequently, of the entire system.

6.5 Cost estimate

Besides a first estimate of the overall mass of the SLAO system, a preliminary cost estimate is provided. The SLAO system is broken down into the mechanical, optical and electronic components and subsystems used. The cost estimates for the optical and electronic components are based on Stuij^[75].

Mechanical components	
Support structure incl. cleanliness sheets	35,000 €
Optics mounts	15,000 €
M1 translation system	25,000 €
M7-M8 translation stage	15,000 €
Standard parts	1,500 €
<i>Subtotal cost</i>	<i>91,500 €</i>
Optical components	
Pickup mirror	10,000 €
Fold mirrors	10,000 €
Large zoom lenses	50,000 €
Small zoom lenses	20,000 €
Reimaging lenses	5,000 €
Telecentric lens	500 €
Lenslet array	1,500 €
<i>Subtotal cost</i>	<i>97,000 €</i>
Electronic components	
Cabling	5,000 €
LCU	5,000 €
LISA Camera	-
RTC Hardware	40,000 €
<i>Subtotal cost</i>	<i>50,000 €</i>
Total Cost	238,000 €
Total Cost with 30% contingency	310,050 €

Table 6.31. Cost estimate for the SLAO system.

It should be noted that the above estimate does not include the cost related to the work of the engineers involved in the development of the system.

6.6 Requirement verification

In Chapter 3 the requirements have been defined, based on which the (opto)mechanical design of the SLAO system has been developed. In this section it will be investigated to what extent these requirements have been fulfilled by the preliminary design presented earlier.

Req. No.	Description	Status	Comment
REQ-S-1	The SLAO system shall not violate the predetermined volume and mass limits, as defined in <i>Table 3.1</i> .	✓	The total mass can be further decreased through a careful study of the structural behavior of the support structure.
REQ-S-2	The design and implementation cost of the entire system shall not exceed 1 M€.	✓	The cost resulting from the work of engineers has not been considered.
REQ-S-3	The design of the optics mounts shall ensure that the stresses in the optical components, resulting from the given load cases (<i>Table 3.1</i>), do not compromise their optical performance.	●	Hand calculations of the contact stresses have been performed; however, a careful study of the optical performance of the system for different load cases is necessary.
REQ-S-4	The design of the support structure shall provide the required stiffness for the given survival and operational loads, such that neither the structural health of the SLAO system nor the position accuracy of its subsystems and components are compromised.	●	The structural behavior of the support structure needs to be investigated.
REQ-S-5	The design of the support structure shall guarantee accessibility to the individual components of the system. <i>Rationale: Accessibility to the components and subsystems in the SLAO system can facilitate the integration, optical alignment and maintenance of the system.</i>	✓	For the given design the accessibility of the optical components is ensured.
REQ-S-6	The design or selection of all subsystems and mechanical components in the SLAO system shall ensure that they can provide the necessary position accuracy at all times in the operational case and can withstand the corresponding loads in the survival case (<i>Table 3.1</i>).	✓/●	The application of the required preloads ensures that the optical components will maintain the nominal positions. However, a careful study of the mechanical behavior of the subsystems and subassemblies for different load cases is necessary.
REQ-S-7	The mechanical design of the SLAO system shall include measures that can increase the cleanliness levels of the unit.	✓	Covers have been added to this end.

Table 6.32. Review of general design requirements for the SLAO system.

Req. No.	Description	Status	Comment
REQ-M1-1	The dimensioning of the central opening of the M1 mirror shall guarantee that the vignetting in the scientific and SCAO FoV is lower than <TBD> arcsec.	●	This is to be defined by the updated optical design. The current dimensions of the opening are the average values between the two extremes.
REQ-M1-2	The translation/rotation system of the M1 mirror shall ensure that the component reaches its operational end position with an accuracy of <TBD> mm and/or <TBD> arcmin and with a repeatability of <TBD> mm.	●	The accuracy in the end position can be ensured with the use of a position sensor. The selection of the specific type and characteristics of the sensor has not been included in this report.
REQ-M1-3	The translation/rotation system of the M1 mirror shall provide a travel range of no less than <TBD> mm or <TBD> degrees, in order to ensure that the component does not interfere with the science and NGS beam when the SLAO system is not employed.	✓	The travel range of the M1 translation system ensures that the optical component in the contracted state does not interfere with the science and NGS beam.
REQ-M1-4	The translation/rotation system of the M1 mirror shall ensure that the component reaches its operational end position within <TBD> seconds.	●	The travel speed is yet to be defined. Its value depends on the characteristics of the motor used and the gear ratio of the transmission system.
REQ-M1-5	The position of the translation/rotation system of the M1 mirror shall ensure that it will not contribute to the instrument's background radiation. <i>Rationale: Any sources of thermal radiation (e.g. motor) located close to the science and NGS beam might introduce noise, which could have a negative impact on the instrument's performance.</i>	✓	The most favorable way to move the M1 away from the science and NGS beam has been selected.
REQ-M1-6	The envelope of the translation/rotation system of the M1 mirror shall not violate the allocated volume for the SLAO system (Table 3.1).	✓	-
REQ-M1-7	The design of the M1 subsystem, comprising the mirror mount and the corresponding translation/rotation system, shall ensure that the optical performance of the SLAO system is not degraded by any reflection artifacts.	●	This needs to be investigated when the M1 subsystem is at a more developed stage.

Table 6.33. Review of requirements for the M1 subsystem.

Req. No.	Description	Status	Comment
REQ-RFS-1	The M7-M8 refocusing stage shall provide a travel range of at least 125 mm.	✓	-
REQ-RFS-2	The M7-M8 refocusing stage shall provide a MIM of at least <TBD> μm , in order to be able to accurately follow and correct for the defocus on the WFS for different object distances.	●	The required MIM is yet to be defined. It should be examined whether the MIM provided by the selected translation stage is sufficient.
REQ-RFS-3	The M7-M8 refocusing stage shall guarantee that the two mirrors can reach their end position within <TBD> seconds.	●	The required travel speed is yet to be defined. Nonetheless, the travel speed provided by the selected translation stage is relatively high (s. <i>Table 4.11</i>).
REQ-RFS-4	The M7-M8 refocusing stage shall monitor and provide information about the current position of its carriage at any time.	✓	This is possible with the integrated position sensor provided by the selected translation stage.
REQ-RFS-5	The M7-M8 refocusing stage shall ensure that the pitch and yaw angles do not exceed <TBD> and <TBD> μrad , respectively.	●	It should be investigated whether the specifications of the selected translation stage meet the required lateral position accuracy of the M7-M8 assembly.
REQ-RFS-6	The loaded M7-M8 refocusing stage shall be able to withstand the ambient conditions given in <i>Table 3.1</i> .	✓	The load capacity of the selected translation stage is greater than the actual load.
REQ-RFS-7	The envelope of the M7-M8 refocusing stage shall not violate the allocated volume for the SLAO system (<i>Table 3.1</i>).	✓	-
REQ-RFS-8	The M7-M8 refocusing stage shall ensure that vignetting does not occur for zenith angles equal to or smaller than 45° .	✓	In <i>Figure 6.8</i> three different positions of the M7-M8 assembly are presented. It might be worth investigating at which zenith angle vignetting starts occurring.

Table 6.34. Review of requirements for the M7-M8 refocusing stage.

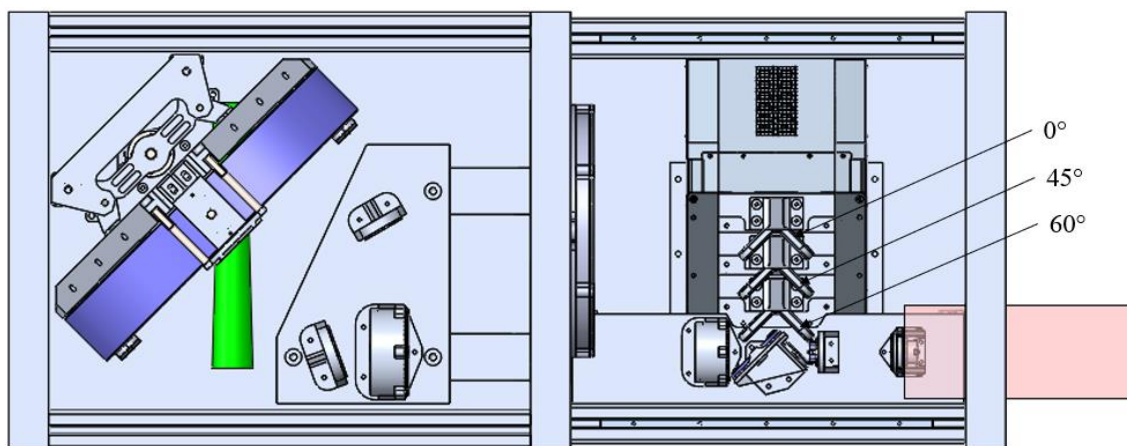


Figure 6.8. Position of M7-M8 assembly at the two extremes and at an intermediate value of the zenith angle. The mirrors M2 and M3 have been hidden for clarity.

6.7 Future work

The developed preliminary (opto)mechanical design of the SLAO system has been presented in Chapter 5 and recommendations, aimed at improving the current design, have been made for every subassembly and subsystem. In this section a number of additional suggestions are discussed, which could be used as input for the following design iterations.

As mentioned earlier, the mass budget of the SLAO system does not include the mounting interface of the SLAO system on METIS's platform. The definition of this interface is important not only in terms of mass, but also in order to study the structural behavior of the support structure, since the latter depends on the constraint type and location. In addition, regarding the optical design, besides the careful study of the optical performance, a stray light analysis should be performed and the inclusion of optical baffles in the design as well as the use of the appropriate optical coatings should be investigated.

Furthermore, using the preliminary design and the earlier-discussed tolerance analysis as a starting point, the integration and alignment processes of the optical components in the SLAO system should be defined and the verification plan of the overall performance of the system should be specified. Lastly, the optomechanical tolerance analysis provided in this thesis does not include the expected temperature variations. Therefore, as a next step the thermomechanical behavior of the SLAO system and its effect on the optical performance should be analyzed for different load cases. As stated earlier, this analysis can be performed at a later stage, when the optical and optomechanical design are sufficiently mature.

7 Conclusions

In this thesis, the preliminary (opto)mechanical design of the Single Laser Adaptive Optics system for METIS has been presented. This system could provide almost full-sky coverage for the instrument, so that additional science goals become attainable. While LTAO systems are, generally, the baseline for telescopes with apertures as large as that of the ELT (due to focal anisoplanatism), a low-cost and low-complexity SLAO system could still guarantee a good performance for long-wavelength observations. For that reason, it was considered worthwhile investigating how such a system can be designed and built without violating the given mass and volume limits and at an affordable price. The main objective of this thesis was to provide a possible solution for the (opto)mechanical design of this system.

Prior to the development of the (opto)mechanical design, the different functions in the SLAO system were identified. Based on these functions as well as the boundary and ambient conditions, the engineering specifications and requirements were defined (Chapter 3). These requirements served as a guide throughout the design process and as reference for the verification of the design, as soon as the latter was completed.

For the (opto)mechanical design a top-down approach was followed, in which the existing optical scheme was first examined and modifications were proposed, aiming at reducing the design and implementation cost and effort, and, potentially, result in better performance (Chapter 4). More specifically, the various ways in which the pickup mirror can be retracted were examined and the advantages and disadvantages of every option were discussed. From this discussion it was concluded that a vertical translation would be the best option, because of the volume limitation but also for reasons associated with the performance of the instrument as a whole.

In addition, different solutions for the design of the support structure of the SLAO system were investigated and the selection of the most favorable one, which is the three-block configuration, was made through a tradeoff. Besides that, for the mounting of all optical components in the SLAO system, mechanical clamping was deemed the best method, mainly because it is usually easier and at the same time it provides a relatively good performance. Nonetheless, given the size differences of the optical components in the system, various concepts were used for the design of the corresponding mechanical mounts.

Furthermore, the result of the search for commercially available translation stages for the implementation of the motions inside the system indicated that a number of COTS translation stages would be suitable for the correction of the defocus through the horizontal translation of the M7-M8 group. By contrast, no vertical translation stages were found for the translation of the pickup mirror, which could meet the requirements in load capacity and travel range. Therefore, it was concluded that for the M1 a translation system had to be designed from scratch.

In Chapter 5 the preliminary (opto)mechanical design of the SLAO system was presented, which proved that the SLAO system can be built within the allocated volume. Moreover, for the design of every mechanical component and/or assembly, the author suggested ways in which the performance could be improved and highlighted any outstanding issues. Lastly, the integration process of the various components and subassemblies into the overall system was provided.

In Chapter 6 the developed design was analyzed in terms of mechanical behavior as well as achievable position accuracy, and the rough mass and cost estimates were presented. Even though in some cases modifications of the mounts are necessary for the reduction of the mount-induced contact stresses, for the most part, the latter are relatively low. Nonetheless, a more detailed analysis of the thermomechanical behavior of the system is necessary. Additionally, given that the allowable position errors are not known yet, the provided tolerance analysis constitutes a first estimate of the errors involved in the mounting of the optical components and can be used as a starting point for the next design iteration. Furthermore, the comparison between the mass and cost estimates of the developed design and the predefined limits, leads to the conclusion that the latter have not been violated.

All in all, the general outcome of the present study, albeit preliminary, suggests that the design and implementation of a SLAO system for METIS, given the mass, volume and budget limitations, would be possible. Lastly, aside from the benefits stemming from an increase in METIS's sky coverage, a SLAO system might prove to be a viable option for other instruments on future terrestrial telescopes of sizes comparable to that of the ELT, on condition that the former perform observations at longer wavelengths.

Bibliography

- [1] Lissauer J. J. & de Pater I., 2019. *Fundamental Planetary Science (updated ed.)*. Cambridge University Press, UK.
- [2] McFadden et al., 2007. *Encyclopedia of the Solar System (2nd ed.)*. Academic Press, USA.
- [3] Impey C., 2007. *The Living Cosmos: Our Search for Life in the Universe*. Random House, New York.
- [4] Schneider P., 2015. *Extragalactic Astronomy and Cosmology: An Introduction (2nd ed.)*. Springer, Germany.
- [5] Labadie L. et al., 2010. *High spatial resolution and high contrast optical speckle imaging with FASTCAM at the ORM*. Proceedings of SPIE (Vol. 7735, 77350X).
- [6] McAlister H., 1977. *Speckle Interferometry as a Method for Detecting Nearby Extrasolar Planets*. Icarus (Vol. 30, Iss. 4), pp. 789-792.
- [7] Tyson R. K., 2000. *Introduction to Adaptive Optics*. Tutorial Texts in Optical Engineering (Vol. TT41), SPIE Press, Bellingham, USA.
- [8] Hardy J. W., 1998. *Adaptive Optics for Astronomical Telescopes*. Oxford University Press, New York.
- [9] Roddier F., 1999. *Adaptive Optics in Astronomy*. Cambridge University Press, UK.
- [10] Brandl B. R. et al., 2018. *Status of the Mid-IR E-ELT Imager and Spectrograph (METIS)*. Proceedings of SPIE (Vol. 10702 107021U).
- [11] Brandl B. R. et al., 2014. *METIS: the Mid-infrared E-ELT Imager and Spectrograph*. Proceedings of SPIE (Vol. 9147, 914721).
- [12] Stuik R. et al., 2016. *Designing the METIS SCAO and LTAO systems*. Proceedings of SPIE (Vol. 9909, 99090B).
- [13] Arcier B., 2018. *Single Laser Adaptive Optics system for the ELT/METIS – Feasibility and performance study*. MSc Thesis, TU Delft.
- [14] Tripsas A., 2019. *Opto-mechanical Design for a Single Laser Adaptive Optics System for METIS*. MSc Thesis, Leiden University.
- [15] Cirasuolo M., 2016. The European Extremely Large Telescope. Retrieved April 30, 2021, from <https://www.roe.ac.uk/workshop/jwst/presentations/cirasuolo-jwst-roe-july-2016.pdf>
- [16] The European Extremely Large Telescope, 2013. Retrieved April 30, 2021, from https://www.eso.org/sci/facilities/eelt/docs/E-ELT_2013-04-02.pdf
- [17] Kissler-Patig M. High angular resolution science with the E-ELT. Retrieved April 30, 2021, from <https://www.eso.org/sci/meetings/2011/VLTI2011/presentations/Kissler-Patig.pdf>

-
- [18] Ramsay S. et al, 2018. *Instrumentation for ESO's Extremely Large Telescope*. Proceedings of SPIE (Vol. 10702, 107021P).
- [19] Ramsay S. et al., 2016. *Progress along the E-ELT Instrument Roadmap*. Proceedings of SPIE (Vol. 9908, 99081T).
- [20] ESO - The ELT Instruments. Retrieved April 30, 2021, from <https://www.eso.org/public/usa/teles-instr/elt/>
- [21] Neichel B. et al, 2018. *Overview of the European Extremely Large Telescope and its instrument suite*. Société Française d' Astrophysique (SF2A).
- [22] Brandl B. et al., 2016. *Status of the mid-infrared E-ELT imager and spectrograph METIS*. Proceedings of SPIE (Vol. 9908, 990820).
- [23] Hippler S. et al., 2019. *Single conjugate adaptive optics for the ELT instrument METIS*. Experimental Astronomy 47.
- [24] Hippler S., 2019. *Adaptive Optics for Extremely Large Telescopes*. Journal of Astronomical Instrumentation (Vol. 8, No. 2).
- [25] ESO Adaptive Optics Modes, 2013. Retrieved April 30, 2021, from https://www.eso.org/sci/facilities/develop/ao/ao_modes/.html
- [26] Bertram T. et al., 2018. *Single Conjugate Adaptive Optics for METIS*. Proceedings of SPIE (Vol. 10703, 1070314).
- [27] Moussaoui N. et al., 2010. *Statistics of the sodium layer parameters at low geographic latitude and its impact on adaptive optics sodium laser guide star characteristics*. Astronomy & Astrophysics 511.
- [28] Schwertz K. & Burge J. H., 2012. *Field Guide to Optomechanical Design and Analysis*. SPIE Field Guides (Vol. FG26), Bellingham, Washington, USA.
- [29] Yoder P. R. & Vukobratovich D., 2015. *Opto-Mechanical Systems Design (Vol. 2): Design and Analysis of Large Mirrors and Structures (4th ed.)*. CRC Press, Boca Raton, Florida.
- [30] Vukobratovich D. & Yoder P., 2018. *Fundamentals of Optomechanics*, CRC Press, Boca Raton, Florida.
- [31] Chin D., 1964. *Optical Mirror-Mount Design and Philosophy*. Applied Optics (Vol. 3, No. 7).
- [32] Yoder P. R. & Vukobratovich D., 2015. *Opto-Mechanical Systems Design (Vol. 1): Design and Analysis of Opto-Mechanical Assemblies (4th ed.)*. CRC Press, Boca Raton, Florida.
- [33] Lamontagne F. & Desnoyers N., 2019. *New solutions in precision lens mounting*. The 11th International Conference on Optics-Photonics Design & Fabrication (ODF' 18), Hiroshima, Japan.
- [34] Lamontagne F. et al., 2021. *High accuracy lens centering using edge contact mounting*. SPIE Digital Library, Journal of Optical Engineering (Vol. 60, Issue 5).
- [35] Fischer R. E. et al., 2008. *Optical System Design (2nd ed.)*. SPIE Press. McGraw-Hill, USA.
- [36] Kasunic K. J., 2015. *Optomechanical Systems Engineering*. John Wiley & Sons, New Jersey, USA.

- [37] Ahmad A., 2017. *Handbook of Optomechanical Engineering (2nd ed.)*. CRC Press, Boca Raton, Florida.
- [38] M-IMS300V (Newport) vertical translation stage. Retrieved April 30, 2021, from <https://www.newport.com/p/M-IMS300V>
- [39] VTS300-200 (Aerotech) vertical translation stage. Retrieved April 30, 2021, from <https://www.aerotech.com/product/stages-actuators/vts300-mechanical-bearing-screw-driven-lift-stage/>
- [40] MOZ-300-200-H (Optics Focus) vertical translation stage. Retrieved April 30, 2021, from <https://www.optics-focus.com/motorized-high-load-vertical-lift-stage-p-1217.html#.YIvyPO3itPb>
- [41] 8MT195Z-340-10 (Standa) vertical translation stage. Retrieved April 30, 2021, from http://www.standa.it/products/catalog/motorised_positioners?item=259
- [42] 960-0115-340-2.5 (EKSMA) vertical translation stage. Retrieved April 30, 2021, from https://eksmaoptics.com/out/media/960-0115_Long-Travel_Motorized_Linear_Stages.pdf
- [43] OSMS26-300(Z)-M6 (SIGMAKOKI) vertical translation stage. Retrieved April 30, 2021, from https://www.laserlabsource.com/files/pdfs/labmotioncontrol_com/458/Motorized_Z_Stage_300mm_4um_10mms_Sigma_Koki-1509675487.pdf
- [44] SKF precision rail guides. Retrieved May 2, 2021, from http://www.mecapedia.uji.es/catalogos/guia_lineal/skf.2.pdf
- [45] SKF profile rail guides. Retrieved May 2, 2021, from <https://www.mpdims.cz/contents/editor/ke-stazeni/linearni-vedeni/kul-lin-skf.pdf>
- [46] HELIX linear sliders. Retrieved May 2, 2021, from <https://www.helixlinear.com/Products/Linear-Sliders/375>
- [47] Power screw types. Retrieved May 2, 2021, from <https://www.linearmotiontips.com/acme-or-trapezoidal-whats-the-difference-between-lead-screws-designs/>
- [48] Power lead screw. Retrieved May 2, 2021, from <https://www.abssac.co.uk/p/Power+Lead+Screws/Trapezoidal+Carbon+Steel+C45+POWER+screw+TRC45/113/>
- [49] Power ball screw. Retrieved May 2, 2021, from <https://www.heason.com/news-media/technical-blog-archive/how-do-ball-screws-work->
- [50] Motorized lead screw configurations. Retrieved May 2, 2021, from <https://feyc.eu/download/catalogos/lineal/thomson/Motorized%20Lead%20Screw.pdf>
- [51] Motorized lead screw configurations. Retrieved May 2, 2021, from https://www.haacon.com/media/kataloge/spindelhubgetriebe_en.pdf
- [52] Screw jack for rotating lead screw. Retrieved May 3, 2021, from https://www.thomsonlinear.com/downloads/actuators/Worm_Gear_Screw_Jacks_ctuk.pdf

- [53] V-508.6 PIMag (PI) horizontal translation stage. Retrieved April 30, 2021, from <https://www.physikinstrumente.nl/en/products/linear-stages/miniature-linear-stages/v-508-pimag-precision-linear-stage-1200210/#description>
- [54] V-551.4x (PI) horizontal translation stage. Retrieved April 30, 2021, from <https://www.physikinstrumente.nl/en/products/linear-stages/stages-with-magnetic-direct-drive-linear-motor/v-551-precision-linear-stage-1200204/#description>
- [55] XMS160-S (Newport) horizontal translation stage. Retrieved April 30, 2021, from <https://www.newport.com/p/XMS160-S>
- [56] DL125 (Newport) horizontal translation stage. Retrieved April 30, 2021, from <https://www.newport.com/p/DL125>
- [57] PCR32...0135 (Prismatics) horizontal translation stage. Retrieved April 30, 2021, from https://www.laserlabsource.com/files/pdfs/labmotioncontrol_com/271/Motorized_Linear_Stage_13_5mm_5nm_500mms_Prismatics-1509417732.pdf
- [58] ALS1000-150 (Aerotech) horizontal translation stage. Retrieved April 30, 2021, from https://www.laserlabsource.com/files/pdfs/labmotioncontrol_com/530/Motorized_Linear_Stage_15_0mm_5nm_750mms_Aerotech-1509808254.pdf
- [59] ANT130L-160 (Aerotech) horizontal translation stage. Retrieved April 30, 2021, from https://www.laserlabsource.com/files/pdfs/labmotioncontrol_com/539/Motorized_Linear_Stage_16_0mm_1nm_350mms_Aerotech-1509851071.pdf
- [60] LMS-270KSHO (PI) horizontal translation stage. Retrieved April 30, 2021, from <https://www.physikinstrumente.nl/en/products/linear-stages/stages-with-magnetic-direct-drive-linear-motor/lms-270-precision-linear-stage-1202001/>
- [61] Profile 12 60x60 light, natural. Article No.: 0.0.001.16. Retrieved April 30, 2021, from <https://product.item24.de/en/products/product-catalogue/productdetails/products/line-12-construction-profiles-1001042800/profile-12-60x60-light-natural-116/>
- [62] Profile 8 40x40-45°, natural. Article No.: 0.0.373.45. Retrieved April 30, 2021, from <https://product.item24.de/en/products/product-catalogue/productdetails/products/line-8-profiles-with-angled-outer-face-1001046472/profile-8-40x40-45-natural-37345/>
- [63] Kyungmok K., 2014. *A study of the frictional characteristics of metal and ceramic counterfaces against electro-deposited coatings for use on automotive seat rails*. Wear 320 (2014) 62-67.
- [64] ZrO₂: Material datasheet. Retrieved June 6, 2021, from <https://www.3d-activation.de/wp-content/uploads/2018/09/Zirkonoxid-D.pdf>
- [65] Alloy X8CrNiMoAl15-7-2: Material datasheet. Retrieved April 30, 2021, from <https://www.metalcor.de/en/datenblatt/30/>
- [66] Bushing ZFM-2023-21. Retrieved May 2, 2021, from <https://www.igus.gr/product/93?artNr=ZFM-2023-21>
- [67] PEEK GF30: Material datasheet. Retrieved May 2, 2021, from <https://www.ensingerplastics.com/en/shapes/products/peek-tecapeek-gf30-natural>

-
- [68] Doumeng M. et al., 2019. *Evolution of crystallinity of PEEK and glass-fibre reinforced PEEK under tribological conditions using Raman spectroscopy*. *Wear*, 426-427, 10.1016/j.wear.2018.12.078.
- [69] Kapton HN: Material datasheet. Retrieved May 11, 2021, from <https://www.dupont.com/content/dam/dupont/amer/us/en/products/ei-transformation/documents/DEC-Kapton-HN-datasheet.pdf>
- [70] Alloy C17200: Material datasheet. Retrieved May 11, 2021, from <https://materion.com/-/media/files/alloy/datasheets/copperberyllium/alloy-25-c17200-strip-data-sheet.pdf>
- [71] Parker O-ring Handbook ORD 5700. Retrieved May 11, 2021, from <https://www.parker.com/Literature/O-Ring%20Division%20Literature/ORD%205700.pdf>
- [72] Ginsberg R. H., 1981. *Outline of tolerancing (from performance specification to tolerance drawings)*. *Optical Engineering* (Vol. 20, No. 2). Society of Photo-Optical Instrumentation Engineers.
- [73] Fischer U. et al., 2008. *Mechanical and Metal Trades Handbook (2nd ed.)*. Europa Lehrmittel, Germany.
- [74] Schouten C. H. et al., 1997. *Design of a kinematic coupling for precision applications*. *Precision Engineering* (Vol. 20, Issue 1), pp. 46-52.
- [75] Stuik R., 2019. SLAO Trade-off and Analysis Report (E-REP-NOVA-MET-1216).

Appendix A: Geometry of the optical components

In the following tables the footprints, shapes and clear apertures of all mirrors and lenses, used in the SLAO system, are summarized.

Component	Material	Footprint [mm]
M1	BK7	481.3x361.8
M2	BK7	362.36x256
M3	BK7	150.22
M4	BK7	8.2
M5	BK7	53.48
M6	BK7	85.54
M7	BK7	37.3
M8	BK7	17.52
M9	BK7	30.8

Table A.1. List of all mirrors in the SLAO system. All mirrors are flat. The above footprints of the laser beam correspond to a zenith angle equal to 0° , i.e. when their size is maximum.

Component	Material	Front RoC [mm]	Center thickness [mm]	Back RoC [mm]	Clear aperture [mm]
L1	BK7	2,529.616	29.59733	-6,705.434	308.2
L2	BK7	523.9352	20.52985	1,280.141	133.8
L3	BK7	-131.6967	10.01463	-108.6533	104
L4	BK7	-452.0431	7.494904*	-193.2538	105.6
L5	BK7	1,471.177	6.104323	-1,100.793	69.2
L6	BK7	398.0573	14.21101	1,227.544	65.8
L7	BK7	-2,218.355	21.61098	-79.34138	26.8
L8	BK7	21.77337	7.76837	39.49803	29.3634
L9	BK7	-54.91468	11.38807	-673.4098	21.4
L10	BK7	Inf.	2	Inf.	19.2

*: The center thickness has been increased to 12 mm, so that the rim thickness remains positive.

Table A.2. List of all lenses in the SLAO system. The above clear apertures correspond to a zenith angle equal to 0°, i.e. when their size is maximum.

Appendix B: Thermomechanical properties of the materials used in the SLAO system

Material	E [GPa]	ν [-]	$\sigma_{y0.2\%}$ [MPa]	CTE [$1/^\circ\text{C}$]
BK7	82	0.208	N.A.	7.1×10^{-6}
AA7075-T6	71.7	0.33	400	23.6×10^{-6}
1.4301 (X5CrNi18-10)	200	0.3	190	16×10^{-6}
UNS C17200-AT (TF00)	131	0.3	960-1210	17.5×10^{-6}
ZrO₂	205	0.3	N.A.	10×10^{-6}
PEEK GF30	6.3	0.37	N.A.	40×10^{-6}
Kapton HN	2.76	0.34	N.A.	20×10^{-6}
Silicone*	6.2×10^{-3}	0.47-0.49	N.A.	200×10^{-6}
FKM*	$1.4-13.8 \times 10^{-3}$	0.5	N.A.	198×10^{-6}

*: O-ring materials.

Table B.1. List of thermomechanical properties of all materials used for the optomechanical design of the SLAO system.

Appendix C: COTS components used in the SLAO system

No	Item type	Part No.	Qty	Supplier	Function	Subassembly/Subsystem
1.	Beam 60 x 60	0.0.001.16	8	item	Block connection	Support structure
2.	Beam 40x40-45°	0.0.373.45	2	item	Mounting plate support	Support structure
3.	Beam 50 x 50	0.0.624.52	2	item	Translation system support	M1
4.	Motor	<TBD>	1	<TBD>	Vertical translation of M1	M1
5.	Screw jack	<TBD>	1	<TBD>	Vertical translation of M1	M1
6.	Lead screw	<TBD>	1	<TBD>	Vertical translation of M1	M1
7.	Lead nut	<TBD>	1	<TBD>	Vertical translation of M1	M1
8.	Ball bearing	<TBD>	1	<TBD>	Fixing of the lead screw	M1
9.	Coil spring	LHC 192N 06S	2	Lee Spring	Safety spring	M1
10.	Bushing	ZFM-2023-21	2	igus	Reduction of friction between sliders and slider guides	M1
11.	Coil spring	LHP 192L 03S	3	Lee Spring	Application of axial preload	M1

No	Item type	Part No.	Qty	Supplier	Function	Subassembly/Subsystem
12.	Coil spring	LHP 218L 02S	2	Lee Spring	Application of radial preload	M1
13.	Clevis pin	DIN 1445 (1977-02) M6	1	<TBD>	Fixing of radial preload subassembly	M1
14.	Dowel pin	DIN EN ISO 2338 Ø4	2	<TBD>	Fixing of radial preload subassembly	M1
15.	Wave spring	SSB-1339	1	Smalley	Application of axial preload	L1
16.	Coil spring	LC 135JK 01S	3	Lee Spring	Application of axial preload	M2
17.	Coil spring	LC 112J 02 S316	3	Lee Spring	Application of axial preload	M3
18.	Wave spring	YRW-0587	1	Smalley	Application of axial preload	L2
19.	O-ring	Si 970, FL Shore A 70 43x2.5	1	COG	Application of axial preload	M4
20.	O-ring	FKM LT 170 Shore A 70 59x3	1	COG	Application of axial preload	M5
21.	Wave spring	YRW-0475	1	Smalley	Application of axial preload	L3-L4
22.	O-ring	Si 820, Shore A 70 41x2	1	COG	Application of axial preload	M7
23.	O-ring	Si 850, TR Shore A 50 36x2	1	COG	Application of axial preload	M8

No	Item type	Part No.	Qty	Supplier	Function	Subassembly/Subsystem
24.	Translation stage	LMS-270KSHO	1	PI	Horizontal translation of M7 and M8	M7-M8
25.	O-ring	FKM LT170 Shore A 70 36x2	1	COG	Application of axial preload	M9
26.	T-slot nut	0.0.003.74	6	item	Fixing of sheet metals for cleanliness	SLAO covers

Table C.1. Parts list for all COTS components in the system.

Appendix D : Preload and contact stress variations with temperature

For all calculations the reference temperature is assumed 20 °C.

Component	Axial preload [N]	Axial σ_c [MPa]	Axial σ_t [MPa]	Radial preload [N]	Radial σ_c [MPa]	Radial σ_t [MPa]
M1	2,273.9	1.0*	0.2*	2,566.6	145.1*	28.2*
M2	1,119.8	0.6*	0.1*	1,410.1	120.2*	23.4*
M3	547.2	0.3*	0.1*	623.3	89.0*	17.3*
M4	**	**	**	N.A.	N.A.	N.A.
M5	**	**	**	N.A.	N.A.	N.A.
M6	19.5	70.3*	13.7*	N.A.	N.A.	N.A.
M7	**	**	**	N.A.	N.A.	N.A.
M8	**	**	**	N.A.	N.A.	N.A.
M9	**	**	**	N.A.	N.A.	N.A.

* : per contact.

** : the compression changes by less than $\pm 1\%$, consequently almost no variations are observed in the preload and contact stresses.

Table D.1. Axial and radial preloads and contact stresses for all mirrors at -33 °C (survival range).

Component	Axial preload [N]	Axial σ_c [MPa]	Axial σ_t [MPa]	Radial preload [N]	Radial σ_c [MPa]	Radial σ_t [MPa]
M1	2,326.7	1.0*	0.2*	1,967.7	129.2*	25.2*
M2	1,135.8	0.6*	0.1*	779.8	93.0*	18.1*
M3	553.6	0.3*	0.1*	460.3	78.0*	15.2*
M4	**	**	**	N.A.	N.A.	N.A.
M5	**	**	**	N.A.	N.A.	N.A.
M6	11.7	54.4*	10.6*	N.A.	N.A.	N.A.
M7	**	**	**	N.A.	N.A.	N.A.
M8	**	**	**	N.A.	N.A.	N.A.
M9	**	**	**	N.A.	N.A.	N.A.

* : per contact.

** : the compression changes by less than $\pm 1\%$, consequently almost no variations are observed in the preload and contact stresses.

Table D.2. Axial and radial preloads and contact stresses for all mirrors at +85 °C (survival range).

Component	Axial preload [N]	Axial σ_c [MPa]	Axial σ_t [MPa]	Radial preload [N]	Radial σ_c [MPa]	Radial σ_t [MPa]
M1	2,288.7	1.0*	0.2*	2,399.1	140.8*	27.4*
M2	1,124.3	0.6*	0.1*	1,233.8	113.2*	22.0*
M3	549.0	0.3*	0.1*	577.7	86.0*	16.7*
M4	**	**	**	N.A.	N.A.	N.A.
M5	**	**	**	N.A.	N.A.	N.A.
M6	17.3	66.2*	12.9*	N.A.	N.A.	N.A.
M7	**	**	**	N.A.	N.A.	N.A.
M8	**	**	**	N.A.	N.A.	N.A.
M9	**	**	**	N.A.	N.A.	N.A.

* : per contact.

** : the compression changes by less than $\pm 1\%$, consequently almost no variations are observed in the preload and contact stresses.

Table D.3. Axial and radial preloads and contact stresses for all mirrors at 0 °C (operational range).

Component	Axial preload [N]	Axial σ_c [MPa]	Axial σ_t [MPa]	Radial preload [N]	Radial σ_c [MPa]	Radial σ_t [MPa]
M1	2,295.4	1.0*	0.2*	2,323.1	138.8*	27.0*
M2	1,126.3	0.6*	0.1*	1,153.7	109.9*	21.4*
M3	549.8	0.3*	0.1*	557.0	84.7*	16.5*
M4	**	**	**	N.A.	N.A.	N.A.
M5	**	**	**	N.A.	N.A.	N.A.
M6	16.3	64.2*	12.5*	N.A.	N.A.	N.A.
M7	**	**	**	N.A.	N.A.	N.A.
M8	**	**	**	N.A.	N.A.	N.A.
M9	**	**	**	N.A.	N.A.	N.A.

* : per contact.

** : the compression changes by less than $\pm 1\%$, consequently almost no variations are observed in the preload and contact stresses.

Table D.4. Axial and radial preloads and contact stresses for all mirrors at +15 °C (operational range).

Component	Axial preload [N]	Front surface σ_c [MPa]	Front surface σ_t [MPa]	Rear surface σ_c [MPa]	Rear surface σ_t [MPa]
L1	904.1	0.9	0.2	0.5	0.1
L2	195.3	1.4	0.3	1.1	0.2
L3	124.2	1.0	0.2	2.6	0.5
L4	124.2	1.4	0.3	1.9	0.4
L5	37.7	0.5	0.1	0.5	0.1
L6	37.7	0.9*	0.2*	27.9*	5.4*
L7	13.6	72.0*	14.0*	12.3*	2.4*
L8	8.2	2.7	0.5	0.1	0.0
L9	8.2	0.1	0.0	0.0	0.0
L10	3.1	14.2*	2.8*	48.2*	9.4*

*: per contact.

Table D.5. Axial preloads and contact stresses for all lenses at -33 °C (survival range).

Component	Axial preload [N]	Front surface σ_c [MPa]	Front surface σ_t [MPa]	Rear surface σ_c [MPa]	Rear surface σ_t [MPa]
L1	895.0	0.9	0.2	0.5	0.1
L2	127.8	1.1	0.2	0.9	0.2
L3	114.8	1.0	0.2	2.5	0.5
L4	114.8	1.4	0.3	1.9	0.4
L5	47.3	0.5	0.1	0.6	0.1
L6	47.3	1.0*	0.2*	31.3*	6.1*
L7	10.0	61.7*	12.0*	10.5*	2.1*
L8	7.8	2.6	0.5	0.1	0.0
L9	7.8	0.1	0.0	0.0	0.0
L10	2.9	13.6*	2.6*	47.1*	9.2*

*: per contact.

Table D.6. Axial preloads and contact stresses for all lenses at +85 °C (survival range).

Component	Axial preload [N]	Front surface σ_c [MPa]	Front surface σ_t [MPa]	Rear surface σ_c [MPa]	Rear surface σ_t [MPa]
L1	901.5	0.9	0.2	0.5	0.1
L2	176.4	1.3	0.2	1.0	0.2
L3	121.6	1.0	0.2	2.6	0.5
L4	121.6	1.4	0.3	1.9	0.4
L5	40.4	0.5	0.1	0.6	0.1
L6	40.4	0.9*	0.2*	28.9*	5.6*
L7	12.6	69.3*	13.5*	11.8*	2.3*
L8	8.1	2.6	0.5	0.1	0.0
L9	8.1	0.1	0.0	0.0	0.0
L10	3.0	14.1*	2.7*	47.8*	9.3*

*: per contact.

Table D.7. Axial preloads and contact stresses for all lenses at 0 °C (operational range).

Component	Axial preload [N]	Front surface σ_c [MPa]	Front surface σ_t [MPa]	Rear surface σ_c [MPa]	Rear surface σ_t [MPa]
L1	900.4	0.9	0.2	0.5	0.1
L2	167.9	1.2	0.2	1.0	0.2
L3	120.4	1.0	0.2	2.5	0.5
L4	120.4	1.4	0.3	1.9	0.4
L5	41.6	0.5	0.1	0.6	0.1
L6	41.6	0.9*	0.2*	29.4*	5.7*
L7	12.2	68.0*	13.2*	11.6*	2.3*
L8	8.0	2.6	0.5	0.1	0.0
L9	8.0	0.1	0.0	0.0	0.0
L10	3.0	14.0*	2.7*	47.8*	9.3*

*: per contact.

Table D.8. Axial preloads and contact stresses for all lenses at +15 °C (operational range).